EPFL

Thèse n° 10 743

Microsecond Time-Resolved Cryo-Electron Microscopy

Présentée le 16 janvier 2024

Faculté des sciences de base
Laboratoire de nanodynamique moléculaire
Programme doctoral en chimie et génie chimique

pour l'obtention du grade de Docteur ès Sciences

par

Oliver Florian HARDER

Acceptée sur proposition du jury

Prof. C. Bostedt, président du jury
Prof. U. Lorenz, directeur de thèse
Prof. B. Zuber, rapporteur
Prof. S. Schäfer, rapporteur
Prof. C. Hébert, rapporteuse

École polytechnique fédérale de Lausanne

2024

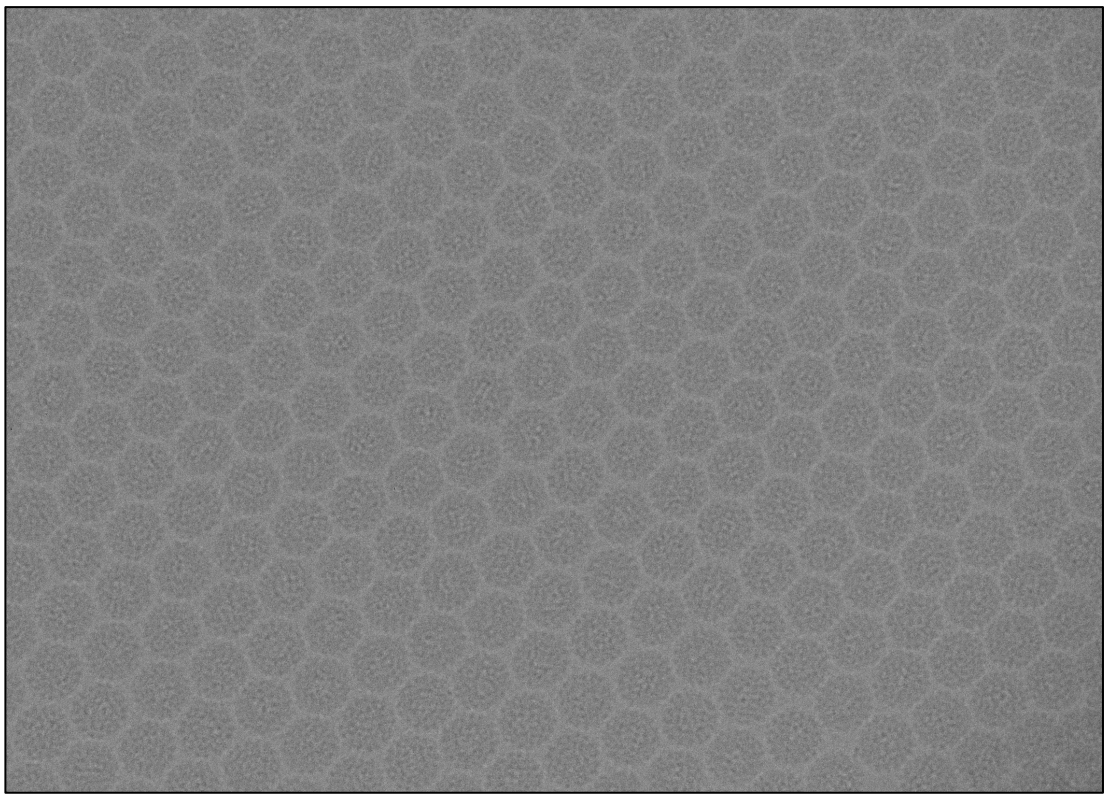

If you're a true contrarian, you're destined to stand alone.

Abstract

Recently, single-particle cryo-electron microscopy emerged as a technique capable of determining protein structures at near-atomic resolution and resolving protein dynamics with a temporal resolution ranging from second to milliseconds. This thesis describes the development of a novel method, microsecond time-resolved cryo-electron microscopy, that extends the time resolution to the microsecond regime. Following thorough characterization, the method is leveraged to produce biological insights by studying the microsecond dynamics of a viral system.

Chapter 3 describes the development and demonstrates the experimental feasibility of microsecond time-resolved cryo-electron microscopy. Its extraordinary temporal resolution is achieved by revitrification, the local melting of a cryo-sample with a heating laser and subsequent cooling and vitrification due to rapid heat transfer, within a few microseconds. Notably, this is achieved within the vacuum of an electron microscope. After characterizing the physical processes and their timescales, transient protein configurations induced by electron beam damage are trapped and imaged in a proof-of-principle experiment.

Chapter 4 provides a detailed description of the typical phenomena and practicalities encountered during microsecond revitrification experiments using microsecond time-resolved cryo-electron microscopy. Insights into microsecond nucleation and crystallization of water are described and interpreted to form a guiding principle to reproduce the experiments with different experimental equipment. The novel approach is easily scalable to the scope necessary for single-particle cryo-electron microscopy and integrates seamlessly into the conventional cryo-EM workflows.

Chapter 5 describes the application of methodology from structural biology to confirm that protein structures and virus structures are conserved during rapid melting and vitrification. Even though samples

crystallize before melting, the investigated biomolecules can be resolved to resolutions comparable to conventional cryo-electron microscopy. During these experiments, further qualitative observations regarding revitrified cryo-samples are made. Foremost, revitrified cryo-samples exhibit different beam induced motion, suggesting structural changes in the vitreous ice due to rapid revitrification. Moreover, particles can clump and reshuffle suggesting that the vitreous ice film is trapped in a disequilibrium which opens the possibility to study technical phenomena like preferred orientation.

Chapter 6 details the application of microsecond time-resolved cryo-electron microscopy to resolve the dynamics of a biological system with state-of-the-art instruments. Cowpea chlorotic mottle virus particles are exposed to a sudden change in pH triggering conformational changes on the microsecond scale. Transient conformations are trapped and imaged with microsecond time-resolved cryo-electron microscopy elucidating the mechanics of the virus capsid protein detrimental to its life cycle and biology.

Keywords: cryo-electron microscopy, time-resolved cryo-electron microscopy, laser heating, protein dynamics, protein structure determination.

Zusammenfassung

Über die letzten Jahre hat sich die Kryo-Elektronenmikroskopie (genauer: die Einzelpartikelmethode) als Technik etabliert, die sowohl Proteinstrukturen mit atomarer Auflösung als auch deren Dynamik auf einer Zeitskala von Sekunden bis zu Millisekunden bestimmen kann. Diese Dissertation beschreibt Ausdehnung auf Mikrosekundenbereich durch die Entwicklung einer neuen Methode, die Kryo-Elektronenmikroskopie mit Mikrosekundenzeitauflösung. Diese Technik wird nach einer umfassenden Charakterisierung auf die Biologie angewandt, um die Dynamik eines Virussystems auf der Mikrosekundenskala zu erforschen.

Kapitel 3 beschreibt die Entwicklung und demonstriert die experimentelle Realisierbarkeit der Kryo-Elektronenmikroskopie mit Mikrosekundenzeitauflösung. Ihre bahnbrechende Zeitauflösung wird durch Wiederverglasung, das Schmelzen einer Kryo-Probe mit einem Laser gefolgt von dem schnellen Abkühlen und Verglasen durch Wärmetransport, ermöglicht. Erstaunlicherweise ist dieses Experiment im Hochvakuum eines Elektronenmikroskops realisierbar. Nachdem die physikalischen Prozesse und ihrer Zeitskalen charakterisiert sind, werden in einer Machbarkeitsstudie transiente Proteinstrukturen, erzeugt durch Elektronenstrahlschaden, eingefroren und abgebildet.

Kapitel 4 bietet eine detaillierte Beschreibung der typischen Phänomene und Herangehensweisen, die während der Experimente gefunden wurden. Um die Reproduktion der Experimente mit variierender Ausrüstung zu ermöglichen, wird eine Reihe von Leitprinzipien entwickelt. Dies geschieht durch die Beschreibung und Interpretation von Einblicken in die Nukleation und Kristallisation des glasigen Wassers innerhalb von Mikrosekunden. Glücklicherweise ist der Ansatz leicht skalierbar und lässt sich nahtlos in die typischen Arbeitsabläufe der Einzelpartikel-Kryo-Elektronenmikroskopie integrieren.

Kapitel 5 beschreibt die Anwendung von Methoden aus der Strukturbiologie, um zu bestätigen, dass Proteine und Viren während der schnellen Wiederverglasung strukturell intakt bleiben. Obwohl Proben vor dem Schmelzen kristallisieren, können die untersuchten Biomoleküle zu einem Grad aufgelöst werden, der mit der herkömmlichen der Kryo-Elektronenmikroskopie vergleichbar ist. Während dieser Experimente werden weitere qualitative Funde gemacht. Zunächst stellt sich heraus, dass die Wiederverglasung strukturelle Veränderungen im gefrorenen Eis hervorbringt, die sich in einer unterschiedlichen elektronenstrahl-induzierten Bewegung spiegelt. Darüber hinaus werden Biomoleküle in neuartigen Anordnungen gefunden, was darauf hindeutet, dass sich der dünne Wasserfilm in einem Ungleichgewicht befindet. Dies bietet die Möglichkeit technische Phänomene wie beispielsweise Orientierungs-Bias zu studieren.

Kapitel 6 beschreibt die Anwendung der Kryo-Elektronenmikroskopie mit Mikrosekundenzeit-auflösung um die Dynamik eines biologischen Systems mit hochmodernen Instrumenten zu untersuchen. Viruspartikel des Cowpea Chlorotic Mottle Viruses werden einer plötzlichen pH-Veränderung ausgesetzt, was zu Konformationsänderungen innerhalb von Mikrosekunden führt. Transiente Konformationen können mit Hilfe der neuen Methode eingefroren und abgebildet werden, was ermöglicht einige der Mechanismen, die für den Lebenszyklus und die Biologie des Virus relevant sind, strukturell aufzuklären.

Schlüsselwörter: Kryo-Elektronenmikroskopie, zeitaufgelöste Kryo-Elektronenmikroskopie, Laser-erwärmung, Proteindynamik, Proteinstrukturbestimmung.

Table of Contents

Chapter 1: Introduction

1.1 The Study of Proteins

Proteins play a critical role in sustaining life, serving a diverse range of functions. They can provide structural support for tissues such as bone, horn, hair, and shells or might fulfil various active and dynamic roles as enzymes, transporters, regulators, messengers, antibodies, or the root cause of disease.[1,2] Active proteins can be considered as nano-scale machines that might enable us one day to precisely control or even repurpose their biological functions for medicine or bioengineering.[3] While promising, our comprehension of their operational principles is driven by the disciplines of structural biology or protein dynamics and has remained largely incomplete, especially when accounting for more complex, native biological environments.[2,3] Before discussing the state and limitations of these fields, it is essential to offer a concise historical overview, enabling us to fully appreciate their remarkable trajectory, potential, and current limitations.

In 1819, Joseph Proust isolated the first amino acid, leucine, from wheat flour.[4] Its constitution was finally understood in 1891 while the role of amino acids as the building block of proteins remained unclear throughout the remainder of the century.[5] Remarkably, the last amino acid to be discovered, threonine, was identified in 1935 by William Rose.[6]

By 1833, Anseleme Payen and Jean Persoz had successfully extracted the first protein, diastase, and studied its function.[7] They named what turned out to be an enzyme after its critical function in sugar production which, according to their understanding, was the separation of sugar from starch.[7] However, in 1835, Jöns Berzelius instead proposed catalytic properties of diastase converting starch in to sugar.[8] Elemental analysis by his colleague Gerardus Mulder on a range of common biomolecules led both to the erroneous conclusion that all studied molecules consisted of identical primary moieties.[9] Hence, the term protein in the meaning of primary (constituent of life) was coined.[8] In 1902, Franz Hofmeister and later that same day Hermann/Emil Fischer proposed that proteins are polypeptides, amino acids linked by peptide bonds.[10] This proclamation established the concept of a protein's primary structure, sparking further interest in protein structures and ultimately laying the foundation for structural studies on proteins.[10]

Linus Pauling used chemical intuition in bond chemistry to correctly predict secondary structures of proteins.[11] Curiously, polypeptide chains tend to arrange into a small set of motives known as alpha helices, beta sheets, beta turns and omega loops.[11] [12] Secondary structures usually form spontaneously as intermediates before a protein can fold into its functional shape called tertiary structure.[12]

From 1949 onwards, Frederick Sanger embarked on a decade-long study that culminated in the first complete sequencing of a protein, bovine insulin. This achievement finally confirmed the concept proposed by Franz Hofmeister in 1902.[13] Sanger's discovery, revealing the clearly defined sequences of insulin A and B, led him to propose that any protein could be uniquely defined by its sequence of amino acids and postulate the foundations for the central dogma of molecular biology.[12] [13]

In 1958, a significant milestone was achieved when Max Perutz and John Kendrew solved the structure of hemoglobin and myoglobin, respectively, through X-ray crystallography.[14] [15] [16] John Kendrew commented on the structure of myoglobin: "Perhaps the most remarkable features of the molecule are its complexity and its lack of symmetry. The arrangement seems to be almost totally lacking in the kind of regularities which one instinctively anticipates, and it is more complicated than has been predicted by any theory of protein structure. Though the detailed principles of construction do not yet emerge, we may hope that they will do so at a later stage of the analysis."[15] As detailed later in this work, understanding the principles of construction would take a lot more effort and time than expected.

Nevertheless, this monumental advance led to a stunning increase in protein structures solved with hallmark structural research continuing well into the 21st century. In 1985 the first integral membrane protein, the photosynthetic reaction center, was solved.[17] In 2000, the structure of the ribosome was solved to 2.4 Å[18] and, in 2001, the structure of RNA Polymerase and its role in DNA transcription was unveiled.[19] Complementary techniques such as nuclear magnetic resonance spectroscopy for the structure determination of smaller molecules and Neutron diffraction allowing the location of hydrogen atoms were established as routine methods for structure determination.[20] [21] Still, X-ray crystallography has remained the leading technique in terms of pure number of structures solved and deposited onto the Protein Data Bank.[22] Recently, single-particle cryo-electron microscopy (cryo-EM) with its origins in electron

crystallography has emerged as a powerful complementary technique for structure determination.[23] While generally more costly than X-ray crystallography, it allows to circumvent the need for a protein crystal which in many cases presents a major obstacle in advancing structural research.[24]

All the forementioned advances have collectively contributed a stunning number of over 200,000 protein structures deposited in the Protein Data Bank as of 2023.[25] An even more remarkable breakthrough was engineered in 2020 when scientists from DeepMind shocked the word of science by solving the question pondered by John Kendrew in 1958. Using deep neural networks, they achieved the reliable prediction of protein structures solely from their amino acid sequences.[26] This achievement holds the promise of solving the structure of the remaining estimated two billion proteins by computational means.[27]

Hopefully, this brief historical review illustrates the exponential advances in structural biology which promise incredible developments in biology and medicine. However, the second key to leveraging our understanding of proteins and exerting control over biology lies within the discipline of protein dynamics.[28] Before sketching the state, challenges and current limitations of protein dynamics, I would like to take the opportunity to introduce single-particle cryo-electron microscopy which is a promising technique for the study of protein dynamics and forms one of the two pillars this work is built upon.

1.2 Single-Particle Cryo-Electron Microscopy

The general idea behind single-particle cryo-electron microscopy is to embed proteins of interest in a thin film of vitreous ice and image them at high resolution in a transmission electron microscope. After collecting a large number of recorded micrographs and treating them statistically, the protein structure can be solved. In sequence, the three key steps of cryo-EM are sample preparation, data collection and data treatment which each had to overcome their historical challenges.[23]

During its operation, an electron microscope necessitates a high vacuum within its column, thereby presenting a challenge for hydrated samples, such as proteins immersed in an aqueous buffer solution.[29 30] Starting in 1981, Jacques Dubochet successfully achieved the preparation of thin vitreous ice films, wherein proteins of interest were able to maintain their structural integrity while being protected from the vacuum environment, owing to the very low vapor pressure of glassy water.[31 32] His methodology would become the blueprint for sample preparation, wherein the thin film is created by either spraying the protein solution onto a grid or blotting it with a blotting paper. The grid is then promptly immersed into a cryogen, ensuring the film's vitrification.[31 32 33]

Biological molecules and films of vitreous ice are generally stabilized by weaker interactions and are therefore easily damaged by the electron beam and induced secondary effects.[34] Richard Henderson established that electrons are the best feasible probe for imaging biomolecules considering the ratio of information extracted versus induced sample damage.[35] Electron doses that prevent significant structural damage are so small that images inherently have a very low signal-to-noise ratio.[35] Moreover, the general limitations of electron microscopy such as shot noise, radiation damage from inelastic scattering, detector noise, "background structure" noise due to the vitreous ice film and sample drift can add considerable noise (as in Fig. 1 a). While the advent of direct detectors and the continuous improvement of reconstruction algorithms have pushed the typical resolution of a cryo-EM map to a few Å, the necessity to image a large number of particles and to treat them as statistical ensemble persists.[23 35 36]

Achieving atomic resolution for weak-phase objects such as biomolecules requires three conditions. First, Friedrich Zemlin found that images taken at different defocus values can be synthesized allowing all spatial frequencies to be sampled.[37] Second, Joachim Frank demonstrated that high spatial frequency information can be recovered if particles contain enough information to be grouped and averaged according to their orientation (as in Fig. 1 b).[38] Naturally, this puts a lower technical limit on the molecule size that can be resolved with cryo-EM.[35] Finally, from a stochastic point, this averaging is possible as the noise is zero-mean in Fourier space implying that the average of many noisy images will converge to the original signal.[39] With these three conditions fulfilled a molecule of interest can be reconstructed by averaging different orientations using the projection slice theorem.[40] Unlike in X-ray crystallography, a starting structure is not necessary to obtain a high-resolution density map (as in Fig. 1c) allowing to avoid human biases.

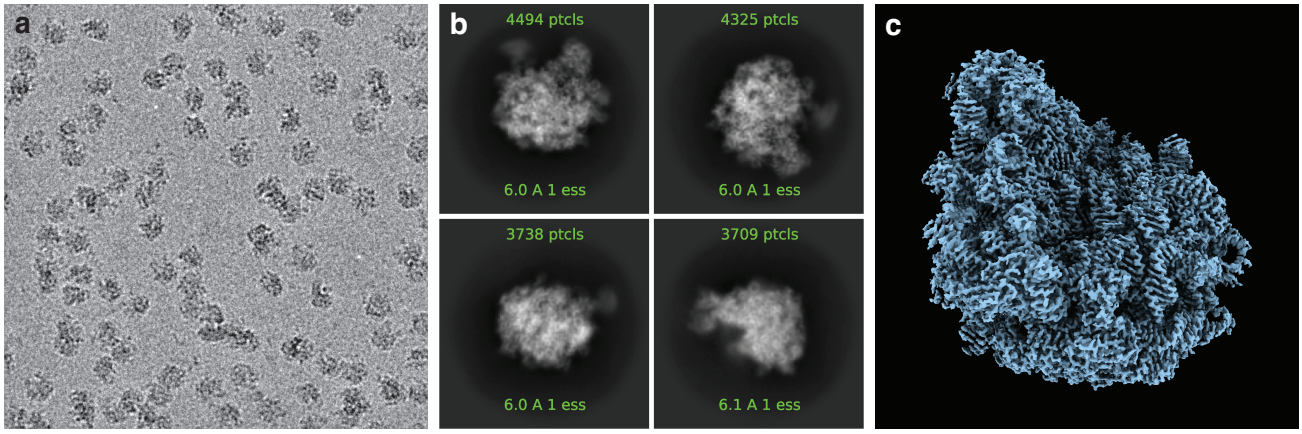

Figure 1. Examples of Cryo-Electron Microscopy. (a) Noisy cryo-EM micrograph containing proteins. (b) Averaged particles for different orientations at 6 Å. (c) Cryo-EM map of 50S Ribosome at 2 Å.

The growing importance of cryo-EM to structural biology as a complementary alternative to x-ray crystallography can be illustrated with the example of the SARS-CoV-2 spike protein. Without the need for a crystal, the structure in its pre-fusion conformation was solved in February 2020, just a few months after the virus' identification, contributing to the rapid development of vaccines.[41] One might only speculate how much more progress could have been made if it was possible to observe the spike protein's dynamic role directly.

1.3 Resolving Protein Dynamics

Understanding a proteins dynamic nature is important since proteins are not critical to life not just due to their structure, their function is often determined by their dynamic motive.[42] Currently, most of our limited understanding of any protein's function in a biological process is inferred indirectly based on snapshots of static structures or the interpretation of results from chemical reactions.[28 42 43]

Myoglobin is again a perfect case study to illustrate the history and typical techniques for studying protein dynamics: The very moment the structure was solved in 1958, questions about its dynamic nature arose.[15] Myoglobin's structure, as an oxygen-storing protein, did not allow an open pathway to the binding site without rearrangement as this pathway is typically blocked in crystal structures.[44] This seemingly innocent question kicked off a series of studies spanning a wide range of different techniques with investigations carried out to this day:

Spectroscopic techniques were quickly employed, with pump-probe spectroscopy studying how myoglobin rebinds carbon monoxide and oxygen after laser photolysis.[45 46] Rebinding was identified to be a multi-step process with different rates suggesting larger than expected heterogeneity in myoglobin's functional conformations.[45 46]

Mutagenesis, a technique where parts of the protein structure are altered genetically, was used in several studies to investigate functional aspects of myoglobin's structural dynamics.[47 48] Here, the importance of the solvent in its impact on protein dynamics was investigated as well.[49 50]

Crystallography can provide indirect information about a protein's structural flexibility by the refinement of asymmetric Debye-Waller factors of individual or correlated atoms as studied with X-ray diffraction in myoglobin.[51] Analogously, neutron diffraction data was used to extend the dynamic model of myoglobin by obtaining information about the displacement of individual hydrogen atoms.[52 53] However, the side effects of crystal packing generally have to be taken into account in crystallographic studies, highlighting the need for complementary techniques to study protein dynamics in a more natural environment.[54]

Time-resolved X-ray crystallography has been at the forefront of gathering additional insights into the dynamics of myoglobin: With picosecond time resolution at 1.8 A per frame, transient conformational changes were resolved elucidating the short-lived 140 ps intermediate and the dramatic motions involved in the undocking of CO.[55] Ultrafast experiments with an X-ray free electron laser investigated light-induced the restructuring of myoglobin described as a "proteinquake" with a time resolution of a few hundred femtoseconds.[56]

This short example of myoglobin hopefully illustrates that understanding a protein's dynamic structure is usually orders of magnitude more challenging compared to solving its static structure. While myoglobin's structure is considered to be solved since 1958, its dynamic nature is investigated to this day. In fact, the case has been made that there is no single protein whose function is fully understood at an atomistic and deterministic level.[55] Fundamentally, this can be attributed to this chain of three reasons.

First, protein dynamics are difficult to describe by a general, reductionist framework due to a large number of system dependent complexities and peculiarities. For example, proteins can undergo spontaneous conformational changes that drastically change their dynamic behavior and function.[57] Some proteins exhibit different degrees of intrinsic disorder such as non-foldable regions, semi-foldable regions or missing residues which vary with experimental conditions and again can strongly impact any observable dynamics.[58] In vivo, proteins are exposed to a wide range of possibly different post-translational modifications.[59] Unlike a simple single static protein view, inferring protein dynamics seems to require a more probabilistic and wholistic description facilitated by combining many experimental and computational techniques.[60]

Computational probing of protein dynamics has been insightful and impressive but has remained largely complementary to experiments. One major limitation is the restriction to short timescales with the microsecond regime being the typical practical limit.[61] Another limitation is our incomplete understanding of the force fields involved in the dynamics such as the solvent or protein-specific effects.[62,63] The stunning computational advances in protein folding were possible due to a vast experimentally produced training

datasets.[25 26] Applying this approach to study protein dynamics would likely require large training datasets of dynamics generated by experimental methods.

Experimental insights require techniques with high spatial resolution that can also access timescales ranging from femtoseconds to seconds.[64 65] As the case of myoglobin illustrates, many complementary methods such as time-resolved X-ray crystallography and spectroscopy are necessary to build a coherent yet limited and largely indirect picture of a proteins dynamic nature.[28 42] Following this chain of reasoning, a more extensive arsenal of direct techniques with recent additions like High-Speed AFM seems to be necessary to propel the field of protein dynamics forwards.[66]

Recently, cryo-electron microscopy has been added to the study of biological dynamics. As early as 1989, intermediates in membrane fusion were imaged on the second timescale by manually mixing sample solutions before freezing.[67] Advances in technology that propelled cryo-EM in its importance for protein structure solution also led to its reemergence as a promising technique for resolving protein dynamcis.[68] Unlike in crystallography, proteins are embedded in glassy ice displaying a wide range of configurations that correspond much more closely to their natural state.[69] Nowadays, the possibility of heterogenous populations occurring within one sample is a blessing as they can be separated and solved computationally thereby providing insight into populations and rate constants that allow researchers to model snapshots of the free-energy landscape.[69]

Since then, a wide range of time-resolved techniques has been developed that allow going beyond the time resolution of a few seconds afforded by chemically mixing two reagents on the grid before plunge freezing: Nigel Unwin pioneered "fast on-grid mixing", the first cryo-EM technique reaching millisecond temporal resolution for proteins. By spray-mixing acetylcholine onto a free-falling grid with torpedo ray postsynaptic membranes just before plunging into liquid ethane, he managed to resolve the open channel form of the acetylcholine receptor with a temporal resolution better than 5 milliseconds.[70]

More recently, a general-purpose approach to on-grid mixing has been developed. Using piezoelectric dispensers, two solutions can be deposited and mixed on the surface of a specialized self-blotting grid.[71]

The reaction induced by mixing is arrested due to vitrification when the grid reaches liquid ethane trapping short-lived intermediates. By mixing 50S and 30S ribosomal subunits intermediates such as 50S-50S dimers and the 70S complex could be resolved.[72] Further, conformational changes could be induced and resolved by mixing calcium ions with the calcium-gated potassium channel MthK.[72] On top of allowing time-resolved cryo-EM studies, it promises further quality-of-life improvements such as possibly addressing orientation bias or reducing the sample volumes consumed in preparation.[71 72]

A different approach is "microfluidic mixing": Here, conformational changes are triggered by rapidly mixing two reagents in a microfluidic device wherein its geometry allows controlling the mixing times in a range of 10 – 1000 ms.[73] After leaving the channel, the mixture is sprayed onto a plunging grid which arrests the reaction within a few milliseconds. Studies into the three-component system of the ribosome, elongation factor G and ribosome recycling factor revealed intermediate complexes that formed, their relative populations and the timescale for ribosome recycling.[74]

Ultimately, the current time resolution of cryo-EM is determined by the vitrification speed during plunging with the current practical limitations being a few miliseconds.[68 71] However, the second pillar of this work, the field of time-resolved transmission electron microscopy, has developed methods that can achieve up to femtosecond temporal-resolution at atomic resolution.[75 76]

1.4 Time-Resolved Electron Microscopy

Time-resolved transmission electron microscopy is based on the idea of combining the sub-nanometer resolution afforded by a TEM with modifications improving its temporal resolution.[75] Fundamentally, there are four ways to improve the time resolution of a TEM.

First, the electron source can be modified to change the timescale of electron emission. Historically, Takaoka and Ura were first to modify the electron source to allow for a pulsed extraction voltage.[77] During operation, the extraction voltage was lowered to prevent any significant emission while a rapid and short increase in extraction voltage of the extractor anode allowed to generate electron pulses of 30 microseconds.[76] In 1987, Oleg Bostanjoglo followed a different approach where the filament was irradiated by a laser generating electron pulses of a few nanoseconds.[78] Here, the temperature of the thermionic emitter is lowered to prevent significant emission until a short laser pulse can generate an electron pulse by increasing the filaments temperature or by using the photoelectric effect.[78] More recently, the group of Ahmed Zewail managed to achieve femtosecond temporal resolution by conducting stroboscopic experiments with femtosecond lasers.[79] If a reversible phenomenon can be excited and probed millions of times, the statistical treatment of all the signals from all the probing events can result in atomic resolution.[79]

Another approach is to modify the beam path to control the timescale of the electron flow through the microscope. Historically, this was first accomplished by modifying a beam blanker to deflect the beam.[80] Generally, this approach promises better ease of use and wider accessibility as a conversion from conventional to pulsed operation is more straight forward.[81] To improve spatial and temporal resolution a wide range of designs such as microwave cavities or micro-electro-mechanical plates have been proposed or employed.[81] Compared to modifying the electron source, it seems more challenging to reach similar results due to a lower beam quality from the sweeping of the beam, a somewhat limited beam current and possible pump-probe synchronization jitter.[80 81]

Third, modifications to the sample can slow down the process or reaction of interest. Preparing a sample to change on the timescale of the instrument seems to be extremely difficult as, in general, there isn't a "one fits all" approach. Possibly, one of the most promising examples are the rapid freezing approaches

presented in the previous section which are, as mentioned previously, limited to millisecond temporal resolution.[71 73]

Finally, faster detectors could allow to time-resolve rapid processes. Typically, electron detectors are developed by companies due to their expensive and complex research and development requirements. Currently, a state-of-the-art 4096 by 4096 pixel direct electron detector such as the Falcon 4i operates with a few 100 frames per second potentially allowing for millisecond time resolution.[82] Smaller STEM detectors such the Celeritas XS recently reached readout rates of 87,000 frames per second with 256 by 64 pixels demonstrating that a microsecond time resolution is indeed possible. To be competitive with the previously described approaches, fundamental improvements to electronics and TEMs are necessary which relegate faster detectors to a long-term solution.[83]

Time-resolved TEM has largely been applied to a variety of questions in materials physics. Defect-modulated phonons were imaged on the femtosecond timescale.[84] A prominent area of research are phase transitions like mapping charge density wave domains during the excitation of a tantalum disulfide transition or the observation of transient structures during the phase transition of vanadium dioxide.[85 86] Crystal growth or reaction morphologies have been studied in the rapid solidification of a Al-Si alloy and the nanothermite reaction process of Al/CuO nanoparticles when heated by a laser pulse respectively.[87 88]

Engineering applications such as the micro-second time resolution of dislocation formation, twin nucleation, crack formation and crack propagation in pure copper with a high-rate straining stage are being developed as well.[89] Especially, the additional possibility to combine these findings with the crystallographic orientation obtained by electron diffraction of individual grains seems promising.[89]

Compared to materials science, the applications of ultra-fast transmission electron microscopy in biology have been relatively restricted. By using photoinduced near field effect electron microscopy (PINEM), the photon absorption by electrons in the presence of evanescent fields around nano-scale objects, ultrafast imaging of biological samples was demonstrated.[90] Initially, objects of study would be protein vesicles and E.coli cells, where the laser polarization dependence of the PINEM effect for biological samples was

demonstrated as well.[91] In a follow up, eukaryotic cancer cells or membrane vesicles in the presence of the Epidermal Growth Factor (EGF) and its receptor protein (EGFR) were studied with PINEM as well.[92] It was found that the binding of EGF to its receptor (EGFR) seems to strongly impair the photon absorption.[92] More recently, PINEM was used to resolve the T cell surface structure reorganization after stimulation.[93]

In time-resolved cryo-EM experiments, nanosecond pulsed electron diffraction was used to observe the structural dynamics of amyloid fibrils in their hydrated environment.[94] This proof-of-concept experiment demonstrated the detection of picometer-scale movements on a nanosecond timescale that amyloid fibrils undergo when subjected to the laser-induced temperature jump.[94]

Fundamentally, the reasons that ultrafast transmission electron microscopy had trouble delivering on the dream of direct movies of protein dynamics are the very same core issues cryo-EM faced in its infancy: Biological samples are very sensitive to electron beam damage and images tend to have low signal to noise. Where cryo-EM has seconds to extract a noisy image, time-resolved TEM has only the time of a short pulse for image formation. Typically, time-resolved transmission electron microscopy has solved this with stroboscopic experiments, an approach ill-suited to proteins and their fragile and chaotic nature to be excited and probed millions of times in a reversible manner. In contrast, using the statistical multi-particle approach from single-particle cryo-electron microscopy as a basis and applying laser methodology from time-resolved transmission electron microscopy has no such fundamental limitations.

1.5 Outline

This thesis describes the synthesis of methods, further detailed in Chapter 2, from structural biology and time-resolved transmission electron microscopy which leads to a structural study in biology and culminates in a pioneering investigation of viral protein dynamics on the microsecond-scale.

In Chapter 3, we characterize the discovery of microsecond melting and revitrification of cryo-samples by laser irradiation within a transmission electron microscope. Surprisingly, samples do not evaporate in the vacuum of the microscope allowing us to demonstrate the microsecond disassembly of GroEL in liquid induced by electron beam damage.

In Chapter 4, the phase transitions involved in the microsecond melting and revitrification of cryo-samples are investigated. Crucially, we learn that the approach is scalable such that the methods employed in conventional cryo-EM can be applied seamlessly. Interestingly, we discover that samples crystallize while heating within a few microseconds before melting and revitrifiying.

In Chapter 5, we combine the scalability with statistical methods from single-particle cryo-EM to verify that melting and revitrification conserves protein and virus structures within the spatial resolution of a few Angstroms. Notably, laser heating seems to structurally change the vitreous ice film resulting in a different beam induced motion.

All this foundational work culminates in a state-of-the-art cryo-EM study with microsecond time resolution on a biological system described in Chapter 6. A meticulously prepared ensemble of cowpea chlorotic mottle virus particles is exposed to a pH jump during melting and revitrification. It undergoes conformational changes that are directly resolved on the microsecond timescale elucidating the mechanics of the virus capsid protein which are detrimental to its life cycle and biology.

Finally, the conclusions, ongoing research and future prospects of the thesis are laid out in Chapter 7.

1.6 References

1. K. Numata, How to define and study structural proteins as biopolymer materials, Polym J 52, 1043–1056 (2020).

2. H. Flechsig, A.S. Mikhailov, Simple mechanics of protein machines. J R Soc Interface, 2019;16(155):20190244.

3. L.J. Domigan, J.A. Gerrard, Introduction to Protein Nanotechnology, Methods Mol Biol. 2020;2073:1-13.

4. J.L. Proust, Sur le Principe qui assaisonne les Fromages, Ann Chim Phys. 1819;10:29-49.

5. E. Schulze, A. Likernik: Über die Constitution des Leucins. Ber Deutschen Chem Ges, Band 24, S. 669ff (1891).

6. R. H. McCoy, C. E. Meyer, W. C. Rose, Feeding experiments with mixtures of highly purified amino acids. VIII. Isolation and identification of a new essential amino acid, J. Biol.Chem.1935,112, 283–302.

7. A. Payen, J. F. Persoz, Mémoire su la Diastase, les Principaux Produits de ses Réactions et leurs Applications Aux Arts Industrielles, Ann. Chim., 53, 73-92, 1833.

8. H. Harold, Origin of the Word 'Protein, Nature. 168(4267): 244, 1951.

9. G.J. Mulder, Sur la composition de quelques substances animales, Bulletin des Sciences Physiques et Naturelles en Néerlande: 104. 1838.

10. C. Tanford, J. Reynolds, Nature's Robots: A History of Proteins, Oxford University Press, New York, 2001.

11. L. Pauling, R.B. Corey, Atomic coordinates and structure factors for two helical configurations of polypeptide chains, Proceedings of the National Academy of Sciences of the United States of America. 37 (5): 235–40, 1951.

12. A. Liljas, L. Liljas, J. Piskur, G. Linblom, P. Nissen, M. Kjeldgaard, Textbook of Structural Biology. World Scientific Publishing, Singapore, 2009.

13. F. Sanger, Sequences, sequences, and sequences. Annu Rev Biochem. 1988.

14. H. Muirhead, M.F. Perutz, Structure of hemoglobin. A three-dimensional fourier synthesis of reduced human hemoglobin at 5.5 Å resolution., Nature. 199 (4894): 633–38, 1963.

15. J.C. Kendrew, G. Bodo, H.M. Dintzis, R.G. Parrish, H. Wyckoff, D.C. Phillips, A three-dimensional model of the myoglobin molecule obtained by x-ray analysis, Nature, 181(4610): 662–6. 1958.

16. J.C. Kendrew, R.E. Dickerson, B.E. Strandberg, R.G. Hart, D.R. Davies, D.C. Phillips, V.C. Shore, Structure of myoglobin: A three-dimensional Fourier synthesis at 2 A. resolution, Nature,185: 422-42, 1960.

17. J. Deisenhofer, O. Epp, K. Miki, R. Huber, H. Michel, Structure of the protein subunits in the photosynthetic reaction centre of Rhodopseudomonas viridis at 3Å resolution, Nature, 318(6047):618-24, 1985.

18. N. Ban, P. Nissen, J. Hansen, P.B. Moore, T.A. Steitz, The complete atomic structure of the large ribosomal subunit at 2.4 A resolution, Science. 2000; 289(5481): 905–920.

19. P. Cramer, D.A. Bushnell, J. Fu, A.L. Gnatt, B. Maier-Davis, N.E. Thompson, R.R. Burgess, A.M. Edwards, P.R. David, R.D. Kornberg, Architecture of RNA polymerase II and implications for the transcription mechanism, Science. 2000; 288(5466):640-9.

20. K. Wüthrich, Protein structure determination in solution by NMR spectroscopy, Journal of Biological Chemistry, 265, 36, 1990.

21. X. Cheng, B.P. Schoenborn, Hydration in protein crystals. A neutron diffraction analysis of carbonmonoxymyoglobin, Acta Crystallographica Section B, 46(2), 195-208 1990.

22. The Protein Data Bank H.M. Berman, J. Westbrook, Z. Feng, G. Gilliland, T.N. Bhat, H. Weissig, I.N. Shindyalov, P.E. Bourne (2000) Nucleic Acids Research, 28: 235-242. https://www.rcsb.org/stats/all-released-structures

23. E.Y.D. Chua, J.H. Mendez, M. Rapp, S.L. Ilca, Y.Z. Tan, K. Maruthi, H. Kuang, C.M. Zimanyi, A. Cheng, E.T. Eng, A.J. Noble, C.S. Potter, B. Carragher, Better, Faster, Cheaper: Recent Advances in Cryo–Electron Microscopy, Annual Review of Biochemistry 2022 91:1, 1-32.

24. C. Vénien-Bryan, Z. Li, L. Vuillard, J.A. Boutin, Cryo-electron microscopy and X-ray crystallography: complementary approaches to structural biology and drug discovery, Acta Crystallogr F Struct Biol Commun. 2017; 73 (Pt 4) :174-183.

25. The Protein Data Bank H.M. Berman, J. Westbrook, Z. Feng, G. Gilliland, T.N. Bhat, H. Weissig, I.N. Shindyalov, P.E. Bourne (2000) Nucleic Acids Research, 28: 235-242. https://www.rcsb.org/stats/growth/growth-released-structures

26 J. Jumper, R. Evans, A. Pritzel, et al., Highly accurate protein structure prediction with AlphaFold, Nature. 2021; 596(7873): 583-589.

27 M. Steinegger, M. Mirdita, J. Söding, Protein-level assembly increases protein sequence recovery from metagenomic samples manyfold, Nat Methods. 2019;16(7):603-606.

28 K. Nam, M. Wolf-Watz M, Protein dynamics: The future is bright and complicated!, Struct Dyn. 2023; 10 (1):014301, 2023.

29 K.A. Taylor, R.M. Glaeser, Electron microscopy of frozen hydrated biological specimens, Journal of Ultrastructure Research, Volume 55, Issue 3, 1976.

30 K. Fernandez-Moran, Low-temperature preparation techniques for electron microscopy of biological specimens based on rapid freezing with liquid helium II, Ann N Y Acad Sci. 1960.

31 J. Dubochet, J. Lepault, R. Freeman, J.A Berriman and J.C. Homo, Electron microscopy of frozen water and aqueous solutions, Journal of Microscopy, 128: 219-237, 1982.

32 J. Lepault, F.P. Booy, J. Dubochet, Electron microscopy of frozen biological suspensions, Journal of Microscopy, 1983.

33 J. Dubochet, M. Adrian, J. Lepault, A.W. McDowall, Emerging techniques: Cryo-electron microscopy of vitrified biological specimens, Trends in Biochemical Sciences, Volume 10, Issue 4, 1985.

34 R.M. Glaeser, Limitations to significant information in biological electron microscopy as a result of radiation damage, J Ultrastruct Res. 1971

35 R. Henderson, The potential and limitations of neutrons, electrons and X-rays for atomic resolution microscopy of unstained biological molecules, Q Rev Biophy. 1995.

36 M. Van Heel, Angular reconstitution: a posteriori assignment of projection directions for 3D reconstruction, Ultramicroscopy. 1987;21(2):111-123.

37 F. Zemlin, Image synthesis from electron micrographs taken at different defocus. Ultramicroscopy 1978.

38 J. Frank, A. Verschoor, M. Boublik, Computer averaging of electron micrographs of 40S ribosomal subunits, Science. 1981.

39 W.T. Baxter, R.A. Grassucci, H. Gao, J. Frank, Determination of signal-to-noise ratios and spectral SNRs in cryo-EM low-dose imaging of molecules, J Struct Biol. 2009.

40 G.J. Jensen, Cryo-EM Part B: 3-D Reconstruction. In: Methods in Enzymology. Volume 482, Academic Press, 2010.

41 D. Wrapp, M. Wang, K.S. Corbett, J.A. Goldsmith, C.L. Hsieh, O. Abiona, B.S. Graham, J.S. McLellan, Cryo-EM structure of the 2019-nCoV spike in the prefusion conformation, Science 2020.

42 K. Henzler-Wildman, D. Kern, Dynamic personalities of proteins, Nature, 2007, 450, 964-972.

43 M.D. Miller, G.N. Phillips Jr., Moving beyond static snapshots: Protein dynamics and the Protein Data Bank, JBC Reviews Volume 296, 100749, 2021.

44 E.E. Scott, Q.H. Gibson, J.S. Olson, Mapping the pathways for O2 entry into and exit from myoglobin, J. Biol. Chem. 2001; 276: 5177-5188.

45 R.H. Austin, K.W. Beeson, L. Eisenstein, H. Frauenfelder, I.C. Gunsalus, Dynamics of ligand binding to myoglobin, Biochemistry. 1975; 14: 5355-5373.

46 G.U. Nienhaus, J.R. Mourant, K. Chu, H. Frauenfelder, Ligand binding to heme proteins: The effect of light on ligand binding in myoglobin, Biochemistry. 1994; 33: 13413-13430.

47 M.L. Quillin, R.M. Arduini, J.S. Olson, G.N. Phillips Jr., High-resolution crystal structures of distal histidine mutants of sperm whale myoglobin, J. Mol. Biol. 1993; 234: 140-155.

48 M.L. Carlson, R. Regan, R. Elber, H. Li, G.N. Phillips Jr., J.S. Olson, Q.H. Gibson, Nitric oxide recombination to double mutants of myoglobin: Role of ligand diffusion in a fluctuating heme pocket, Biochemistry. 1994; 33: 10597-10606.

49 G.N. Phillips Jr., B.M. Pettitt, Structure and dynamics of the water around myoglobin, Protein Sci. 1995; 4: 149-158.

50 V. Lubchenko, P.G. Wolynes, H. Frauenfelder, Mosaic energy landscapes of liquids and the control of protein conformational dynamics by glass-forming solvents, J. Phys. Chem. B. 2005; 109: 7488-7499.

51 G.N. Phillips Jr., Comparison of the dynamics of myoglobin in different crystal forms, Biophys. J. 1990; 57: 381-383.

52 B.P. Schoenborn, Neutron Diffraction Analysis of Myoglobin, Nature volume 224, pages 143–146 (1969).

53 J. Smith, K. Kuczera, M. Karplus, Dynamics of myoglobin: comparison of simulation results with neutron scattering spectra, Proc Natl Acad Sci U S A . 1990 Feb; 87(4):1601-5.

54 D.A. Kondrashov, W. Zhang, R. Aranda, B. Stec, G.N. Phillips Jr., Sampling of the native conformational ensemble of myoglobin via structures in different crystalline environments, Proteins, 2008; 70: 353-362.

55 F. Schotte, M. Lim, T. A. Jackson, A. Smirnov, J. Soman, J. S. Olson, G. N. Phillips Jr., M. Wulff, P. A. Anfinrud, Watching a protein as it functions with 150-ps time-resolved x-ray crystallography, 2003 Jun 20;300(5627):1944-7.

56 M. Levantino, G. Schirò, H.T. Lemke, et al., Ultrafast myoglobin structural dynamics observed with an X-ray free-electron laser. Nat Commun. 2015;6:6772. 2015.

57 V.N. Uversky, Unusual biophysics of intrinsically disordered proteins, Biochim Biophys Acta. 2013;1834(5):932-951.

58 T. Le Gall, P.R. Romero, M.S. Cortese, V.N. Uversky, A.K. Dunker, Intrinsic disorder in the Protein Data Bank, J Biomol Struct Dyn. 2007;24(4):325-342.

59 L.D. Vu, K. Gevaert, I. De Smet, Protein Language: Post-Translational Modifications Talking to Each Other, Trends Plant Sci. 2018;23(12):1068-1080.

60 M.D. Miller, G.N. Phillips Jr., Moving beyond static snapshots: Protein dynamics and the Protein Data Bank, J Biol Chem. 2021;296:100749.

61 A. Srivastava, T. Nagai, A. Srivastava, O. Miyashita, F. Tama, Role of Computational Methods in Going beyond X-ray Crystallography to Explore Protein Structure and Dynamics, Int J Mol Sci. 2018;19(11):3401. 2018.

62 P. Gallo, K. Amann-Winkel, C.A. Angell, et al. Water: A Tale of Two Liquids, Chem Rev. 2016;116(13):7463-7500.

63 L.A. Abriata, M. Dal Peraro, Assessment of transferable forcefields for protein simulations attests improved description of disordered states and secondary structure propensities, and hints at multi-protein systems as the next challenge for optimization, Comput Struct Biotechnol J. 2021;19:2626-2636. 2021.

64 G. Haran, H. Mazal, How fast are the motions of tertiary-structure elements in proteins?, J Chem Phys. 2020;153(13):130902.

65 M.G. Guenza, Dynamics of protein droplets revealed by bridging multiple scales, Nature. 2023;619(7971):700-701.

66 K. Lim, N. Kodera, H. Wang et al., High-Speed AFM Reveals Molecular Dynamics of Human Influenza A Hemagglutinin and Its Interaction with Exosomes, Nano Lett. 2020;20(9):6320-6328.

67 D.P. Siegel, J.L. Burns, M.H. Chestnut, Y. Talmon, Intermediates in membrane fusion and bilayer/nonbilayer phase transitions imaged by time-resolved cryo-transmission electron microscopy, Biophysical Journal, Volume 56, Issue 1, 1989.

68 J. Frank, Time-resolved cryo-electron microscopy: Recent progress, Journal of Structural Biology 200, 303–306 (2017).

69 J. Giraldo-Barreto, S. Ortiz, E.H. Thiede, et al., A Bayesian approach to extracting free-energy profiles from cryo-electron microscopy experiments, Sci Rep. 2021;11(1):13657. 2021.

70 N. Unwin, Acetylcholine receptor channel imaged in the open state, Nature. 1995;373(6509):37-43

71 I. Razinkov, V. Dandey, H. Wei, Z. Zhang, D. Melnekoff, W.J. Rice, C. Wigge, C.S. Potter, B. B. Carragher, A new method for vitrifying samples for cryoEM, J Struct Biol. 2016 Aug;195(2):190-198.

72 V.P. Dandey, W.C. Budell, H. Wei, D. Bobe, K. Maruthi, M. Kopylov, E.T. Eng, P.A. Kahn, J.E. Hinshaw, N. Kundu, C.M. Nimigean, C. Fan, N. Sukomon, S.A. Darst, R.M. Saecker, J. Chen, B. Malone, C.S. Potter, B. Carragher, Time-resolved cryo-EM using Spotiton, Nat Methods 2020, 17(9):897-900.

73 B. Chen, S. Kaledhonkar, M. Sun, B. Shen, Z. Lu, D. Barnard, T.M. Lu, R.L. Gonzalez, J. Frank, Structural Dynamics of Ribosome Subunit Association Studied by Mixing-Spraying Time-Resolved Cryogenic Electron Microscopy, Structure, Volume 23, Issue 6, 2015,

74 Z. Fu, S. Kaledhonkar, A. Borg, M. Sun, B. Chen, R.A. Grassucci, M. Ehrenberg, J. Frank, Key intermediates in ribosome recycling visualized by time-resolved cryo-electron microscopy, Structure. 2016 Dec 6; 24(12): 2092–2101.

75 F.M. Alcorn, P.K. Jain, R.M. van der Veen, Time-resolved transmission electron microscopy for nanoscale chemical dynamics, Nat Rev Chem 7, 256–272 (2023).

76 A.H. Zewail: Four-Dimensional Electron Microscopy. Science328,187-193 (2010).

77 A. Takaoka, K. Ura, Stroboscopic TEM with Time Resolution of 30 μs, Journal of Electron Microscopy 32, 299–304 (1983).

78 O. Bostanjoglo, F. Heinricht, Producing high-current nanosecond electron pulses with a standard tungsten hairpin gun, 1987 J. Phys. E: Sci. Instrum. 20 1491.

79 A. Gahlmann, S.T. Park and A.H. Zewail, Ultrashort electron pulses for diffraction, crystallography and microscopy: theoretical and experimental resolutions, Phys. Chem. Chem. Phys., 2008,10, 2894-2909.

80 L.C. Oldfield, A rotationally symmetric electron beam chopper for picosecond pulses, Phys. E: Sci. Instrum. 9, 455, 1976.

81 L. Zhang, J.P. Hoogenboom, B. Cook, P. Kruit, Photoemission sources and beam blankers for ultrafast electron microscopy, Struct. Dyn. 6, 051501 2019.

82 T. Nakane, A. Kotecha, A. Sente, et al., Single-particle cryo-EM at atomic resolution, Nature, 2020, 587, 152-156.

83 P. Ercius, I. Johnson, H. Brown, P. Pelz, S. Hsu, B. Draney, P. Denes, The 4D Camera – An 87 kHz Frame-rate Detector for Counted 4D-STEM Experiments. Microscopy and Microanalysis, 26(S2), 1896-1897 2020.

84 D.R. Cremons, D.A. Plemmons, D.J. Flannigan: Femtosecond electron imaging of defect-modulated phonon dynamics. Nature Communications volume 7, Article number: 11230 (2016).

85 T. Danz, T. Domröse, C. Ropers, Ultrafast nanoimaging of the order parameter in a structural phase transition, Science 2021 22;371(6527):371-374.

86 P. Baum, D.S. Yang, A.H. Zewail, 4D visualization of transitional structures in phase transformations by electron diffraction, Science 2007 2;318(5851):788-92.

87 J.D. Roehling, D.R. Coughlin, J.W. Gibbs, J.K Baldwin, J.C.E. Mertens, G.H. Campbell, A.J. Clarke, J.T. McKeown, Rapid solidification growth mode transitions in Al-Si alloys by dynamic transmission electron microscopy, Acta Materialia, Volume 131, 2017, Pages 22-30.

88 G.C. Egan, T. LaGrange, and M.R. Zachariah, Time-Resolved Nanosecond Imaging of Nanoscale Condensed Phase Reaction, The Journal of Physical Chemistry C 2015 119 (5), 2792-2797.

89 M.D. Grapes, T.T. Li, M.K. Santala, Y. Zhang, J.P. Ligda, N.J Lorenzo, B.E. Schuster, G.H. Campbell, T.P. Weihs, In situ TEM observations of high-strain-rate deformation and fracture in pure copper, Materials Today. 33 2019.

90 B. Barwick, D.J. Flannigan, A.H. Zewail, Photon-induced near-field electron microscopy, Nature 462, 902–906 (2009).

91 D.J. Flannigan, B. Barwick, and A.H. Zewail, Biological imaging with 4D ultrafast electron microscopy, 2010 107 (22) 9933-9937.

92 M. Kaplan, B.K. Yoo, J. Tang, T.E. Karam, B. Liao, D. Majumdar, D. Baltimore, G.J. Jensen, A.H. Zewail, Photon-Induced Near-Field Electron Microscopy of Eukaryotic Cells, Angew. Chem. Int. Ed. 2017, 56, 11498.

93 Y. Lu, B.K. Yoo, A.H.C. Ng, J. Kim, S. Yeom, J. Tang, M.M. Lin, A.H. Zewail, J.R. Heath. 4D electron microscopy of T cell activation. Proc Natl Acad Sci U S A. 2019 Oct 29;116(44):22014-22019.

94 W.P. Fitzpatrick, U.J. Lorenz, G.M. Vanacore, and A.H. Zewail, 4D Cryo-Electron Microscopy of Proteins Anthony, Journal of the American Chemical Society 2013 135 (51), 19123-1912

Chapter 2: Methods

2.1 Cryo-Electron Microscopy Experiments

As mentioned previously, cryo-electron microscopy consists of a costly workflow involving many steps. Unlike melting and revitrification, the cryo-workflow is not described in such detail that an unfamiliar reader can follow. For that purpose, a short introduction to the methodology is presented which relied on a wide range of instruments which were made accessible to us from different laboratories and facilities at EPFL. Quantitative details regarding protein solutions and plunging conditions can be found in the corresponding appendices. Qualitatively, the cryo-EM workflow developed to complete the work presented consists of producing a protein solution, cryo-sample preparation, sample screening, data collection and computational data treatment.

Generally, a large fraction of any cryo-EM workflow is protein production and purification which was not carried out in-house in the context of this work. Protein solutions were made accessible from three sources. The proteins used in Chapter 3 and Chapter 4, recombinant GroEL and extracted apoferritin, were bought in lyophilized shape from suppliers and reconstituted in the wet lab. The samples used in Chapter 5 and Chapter 6, recombinant apoferritin and cowpea chlorotic mottle virus were sample donations in aqueous buffer solutions from EPFL labs and external sources respectively.

Protein buffers were produced with reagents provided by the Protein Production and Structure Core Facility (PTPSP), an EPFL institution. Protein concentrations were measured with a UV Visible NanoDrop Spectrophotometer, PTPSP equipment. For the experiments presented in Chapter 6, specific buffers were exchanged with centrifugal concentrators in a refrigerated centrifuge, equipment provided by PTPSP.

Cryo-EM grids were vitrified using a Vitrobot Mark IV, an instrument accessible through the Interdisciplinary Center for Electron Microscopy (CIME) and the Dubochet Center for Imaging (DCI), EPFL microscopy facilities. This instrument offers the flexibility to adjust various parameters during the

plunge freezing process. A glow discharged grid is held by tweezers and kept in a chamber where humidity and temperature are controlled. Under these conditions, the sample solution is manually pipetted onto the grid which is then plunged mechanically by the machine into liquid ethane. Many parameters such as sample volume, the blotting time, the blotting force or waiting time before blotting are usually varied in search for an ideal sample. Another parameter during sample preparation is the choice of grid where a wide range of geometries and materials can be employed. As described in Chapters 3 and 4, this work is constrained by the necessity of a gold film to allow for rapid laser heating. Hence, all presented work is carried out with 1.2/1.3 or 2/2 UltrAuFoil grids.

Sample Screening is the step before data collection where the relationship between sample production parameters and sample quality is evaluated using a transmission electron microscope to optimize sample quality iteratively. For all experiments, samples were evaluated using a modified JEOL JEM-2200FS with standard alignment procedures.[1]

The Cryo-EM data collection for Chapter 3, 4 and 5 was conducted on a modified JEOL JEM-2200FS.[1] It operates a Schottky-emitter at 200 kV and is equipped with an in-column omega energy filter and a K3 direct detector. One sample can be loaded via a cryogenic side entry holder into the microscope and all aspects of operation are controlled manually. As data quality depends strongly on alignment, a full alignment was performed before each data collection cycle. For optimal alignment, magnification shift, gun shift, gun tilt, beam shift, beam tilt, condenser lens placement and condenser lens astigmatism, objective lens astigmatism, intermediate lens astigmatism, beam shift and beam tilt pivot points, Zemlin-tableau alignment and energy filter configuration were optimized iteratively in manual operation.[2] Before collection, areas with suitable ice thickness and particle distributions were identified manually. During a typical manual data collection session, an average of 100 micrographs can be obtained before the deposition of gas molecules from the column causes an increase in sample thickness that renders the data unusable. Using this equipment and the aforementioned procedures, protein structures can be resolved to around 3-4 Å under ideal conditions.[3]

The Cryo-EM data collection for Chapter 6 was conducted on a state-of-the-art microscope, a Titan Krios G4, at the Dubochet Center for Imaging (DCI) in Lausanne. It operates a cold field emission gun at 300 kV and is equipped with an SelectrisX Energy Filter and a Falcon IV direct detector. Here, support from staff scientists is provided and the collection efficiency is greatly improved due to recent advances in cryo-EM, such as coma-free shift, more stable stages, improved collection algorithms and autoloader cassettes allowing up to 12 samples inside the microscope.[4] As the microscope has an automated alignment and collection software, the main challenge is an efficient, robust configuration and diligent supervision. A typical session would result in about 10.000 micrographs with collection time allocated by the facility being the limiting factor. Cryo-EM under these state-of-the-art experimental conditions can nowadays deliver protein structures at near-atomic resolution.[5]

Data treatment and reconstructions in Chapter 5 and 6 are computationally expensive steps.[6] They were carried out on workstations running CryoSPARC.[7] This software platform facilitates the multistep workflow taking a large number of multi-frame micrographs and ideally returning a high quality cryo-EM density map.[6] Intermediate steps generally follow this sequence: Muti-frame micrographs are motion corrected and their CTF is fitted.[7 8] After excluding low quality micrographs such as heavily contaminated areas, misfitted or misaligned micrographs, particles are picked. [7 8] To this date picking is a major hurdle in cryo-EM data treatment with many approaches such as manual picking, blob picking (picking Gaussians), template picking (requiring an initial model) or deep learning-based picking.[9 10] Picked particles are then typically grouped via a wide range of approaches such as 2D or 3D classification wherein the promising groups are used for the reconstruction of a 3D Volume.[11] Additional analysis such as investigating structural flexibility, structural variability or estimating local resolution is also possible within CryoSPARC.[12]

2.2 Stroboscopic Experiments

In Chapter 3, time-resolved transmission electron microscopy is used to measure the timescale of laser-melting and revitrification. Qualitatively, nanosecond diffraction patterns of a holey gold foil were collected at different points in time to trace the temperature evolution of the sample heated by µs laser pulses using a stroboscopic approach.[13] This investigation can be structured into experimental setup, measurement process and analysis of diffraction patterns.

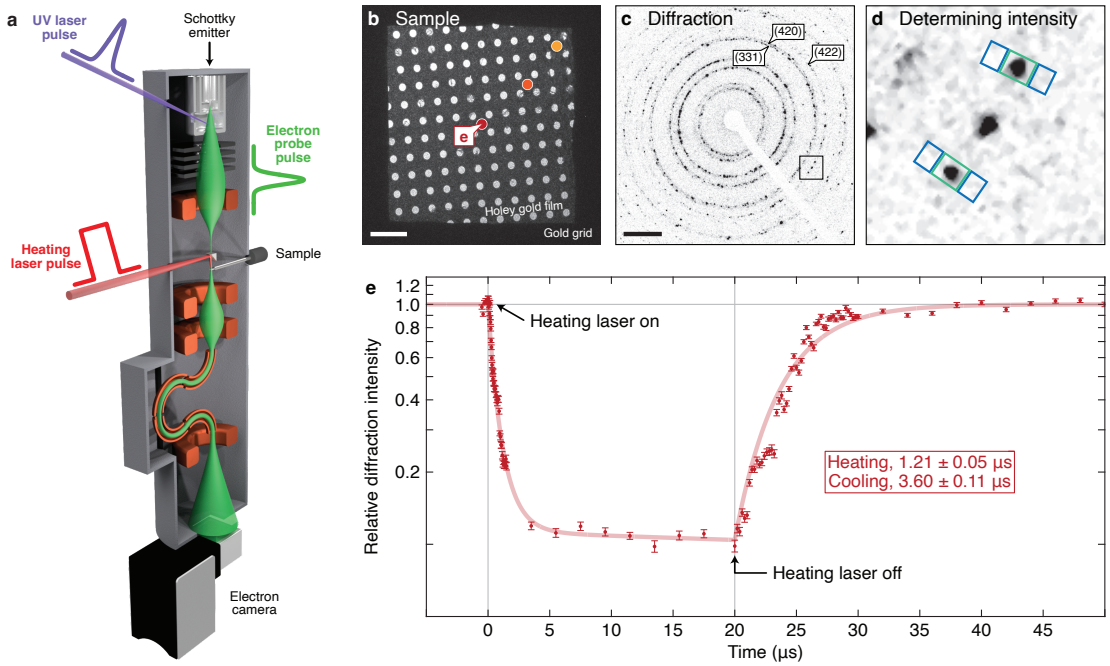

Adapted from Jonathan M. Voss, Oliver F. Harder, Pavel K. Olshin, Marcel Drabbels, Ulrich J. Lorenz, Chem. Phys. Lett., 2021, 778, 138812.

Figure 2. (a) Schematic of the time-resolved electron microscope. (b) Micrograph of grid square. Scale bar 5 µm. (c) Diffraction pattern from area marked with red dot. Scale bar, 5nm^{-1}. (d) Areas used to determine the diffraction signal (green) and background (blue). (e) Temporal evolution of diffraction spot intensity.

The experimental setup (as in Fig. 2a) requires the addition of two lasers to the transmission electron microscope. A nanosecond UV laser beam is guided onto the Schottky emitter. The output of a continuous laser is chopped by an acousto-optic modulator before being directed onto the sample. The sample, a gold foil grid (as in Fig. 2b) is kept in a cryogenic sample holder at 100 K.

Generating of electron pulses via direct photoemission requires suppressing of the continuous emission. For this, the temperature of the emitter is lowered such that electron emission can only occur by irradiation with a UV laser pulse (266 nm, 1 ns, 200 nJ). An electron pulse generated by photoemission (~1 ns, 10^4

electrons) is elastically scattered from a selected sample area that is simultaneously irradiated with a synchronized heating laser pulse (532 nm, 20 μs, 13 mW). The stroboscopic diffraction pattern of the gold foil (as in Fig. 2c) emerges from 8000 pulses at a 1kHz repetition rate when acquiring with the electron camera. To complete one scan, the delay time between electron pulse and laser heating is increased step wise from before time zero to 50 μs. For better statistics, 5 complete scans were recorded.

Performing one or even several scans on samples with a vitreous ice film is not possible as crystallization and evaporation under repeated irradiation by a heating laser is not reversible. For that reason, a plain holey gold foil is chosen as a proxy-measurement. To avoid irreversible deformations in the gold foil, the power of the heating laser is lowered to 13 mW, less than typically required for the revitrification of cryo-samples. While not suitable to determine absolute temperatures, the reliability of this approximation to determine heating and cooling rates has recently been confirmed independently by single shot electron diffraction.[14]

The analysis of diffraction patterns relies on the Debye-Waller factor, which attenuates the intensity of a diffraction spot attenuates exponentially with increasing temperature.[15] For analysis, the intensities of the gold reflections (331), (420) and (422) are monitored (green rectangles in Fig. 2d) and integrated. To subtract the background, the intensity of the neighboring areas (blue rectangles in Fig. 2d) is averaged. On the small scale of this experiment, not all diffraction spots are suitable as specific grains in a thin film can move in or out of diffraction condition under thermal strain. Further, reflections with poor signal to noise ratio or irreversible changes in intensity were discarded.

The diffraction intensities were normalized by estimating the electron beam intensity, which can vary within the few hours necessary to complete this stroboscopic experiment. To estimate the intensity of the electron beam for each scan, a spline was fitted through the time-resolved diffraction patterns unaffected by the laser heating (diffraction patterns collected before time zero or after 40 μs). For one delay time, the intensities were averaged and weighted by the electron beam intensity of the scan. Finally, the relative diffraction intensity, $\log(I/I_0)$, is obtained by accounting for the temperature dependence of the Debye-

Waller factor resulting in the transients shown in Fig. 2e. Similarly, the standard error for one delay was weighted by the electron beam intensity of the scan.

To obtain heating and cooling rates, the transients are fit piecewise with Newtonian heating (f_1) and cooling curves (f_2),

$$\log\left(\frac{I}{I_0}\right) = f_1(t) = \begin{cases} 0 & \text{for } t \leq 0 \\ -a(1 - e^{-t/\tau_{heating}}) - bt & \text{for } t > 0 \text{ and } t \leq 20\ \mu s \end{cases}$$

$$\log\left(\frac{I}{I_0}\right) = f_2(t) = f_1(t = 20\ \mu s) \cdot e^{-(t-20\ \mu s)/\tau_{cooling}} \qquad \text{for } t \geq 20\ \mu s$$

where $\tau_{heating}$, is the heating time, and a and b are fit parameters.

This approach allows to determine the laser heating time and the subsequent cooling time of 1.2 µs and 3.6 µs, respectively. However, for complementary understanding, especially regarding absolute temperatures, heat transfer simulations are a necessary tool.

2.3 Finite-Element Heat Transfer Simulations

In Chapters 3 and 4, we use heat transfer simulations to gain deeper and more intuitive understanding of laser heating and revitrification. They were performed using COMSOL Multiphysics[16]. A detailed, quantitative description can be found in the Appendix of Chapters 3 and 4, respectively.

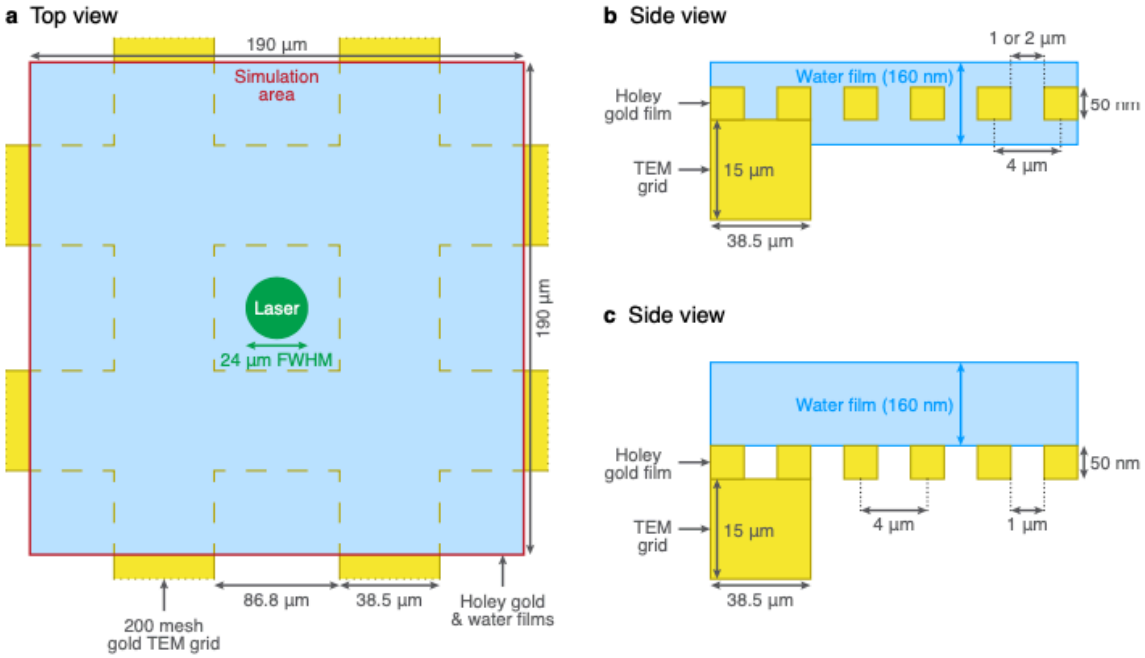

Adapted from Jonathan M. Voss, Oliver F. Harder, Pavel K. Olshin, Marcel Drabbels, Ulrich J. Lorenz, Structural Dynamics 8, 054302 (2021).

Figure 3. Sample geometries for heat transfer simulations. (a) Top view of the simulation geometry. (b) Side view of the simulation geometry with the holey gold film covered on both sides with water. (c) Side view of the simulation geometry for samples in which multilayer graphene is added on top of the holey gold film.

Fig. 3a illustrates the modeled geometry. A 200 mesh TEM gold grid (38.5 µm wide and 15 µm thick bars, 86.8 µm × 86.8 µm viewing area) supports a holy gold film with a thickness of 50 nm. To reduce computational cost, the simulated area is restricted to a central grid square surrounded by parts of neighboring grid squares. As illustrated in Fig. 3b, a vitreous ice film of 160 nm thickness is not just placed within the holes in the foil but uniformly on top and below. To reduce computational cost further, graphene was not included in Chapter 3 as its impact on heat transfer was determined to be negligible.

Note however, that graphene impacts evaporative cooling as water resting on graphene has only half the surface area exposed to vacuum.

Once defined, the geometry is meshed into volume elements where classical heat transfer equations are solved locally at each time step.[17] The distribution in volume per element is varied locally as it represents the local spatial resolution and computational cost. Hence, in areas of interest, elements reach lengths of a few nm while other areas can be up to 10 μm. Typically, simulations run for 50 μs with time-steps of around 0.1 μs having been found to conserve numerical stability.

As inputs, material properties, laser heating, evaporative cooling, starting conditions and boundary conditions have to be given. Materials and their relevant properties such as heat capacity and heat conductivity, are taken from literature for graphene[18 19 20] and gold[21 22]. As values for supercooled water have not been measured for the entire temperature range due to rapid crystallization in "no man's land", the heat capacity is approximated by measurements of supercooled water in silica nanopores.[23] The corresponding thermal conductivity is approximated by the room temperature value, which is close to the amorphous ice at cryogenic temperatures.[24]

Laser heating is simulated by defining a 2D heat source on the surface of the gold film, with the heat following a 2D Gaussian distribution originating at the central hole of the grid square. Its FWHM and magnitude are given by the spot size and the laser power used experimentally with thin film calculations correcting for fractional absorption of the laser light. Analogous, evaporative cooling is simulated as a 2D heat sink depending on the local temperature in the local trapezoid.[25 26 27]

As initial condition, the temperature was set to 100K. In the simulation, the cross-section of each grid bar at the outer limit of the simulated area has its temperature enforced to 100K to approximate the remainder of the grid acting as a quasi-infinite heat sink during the experiment. Notably, the heating does not affect the temperature outside the irradiated cell, as the grid bars are massive heat sinks.

Finally, results are saved and readout in a space saving manner: Aside from volumes of interest, no data is saved. Within volumes of interest, the volume averaged, the minimum and the maximum temperature are stored and can be readout after the simulation finishes.

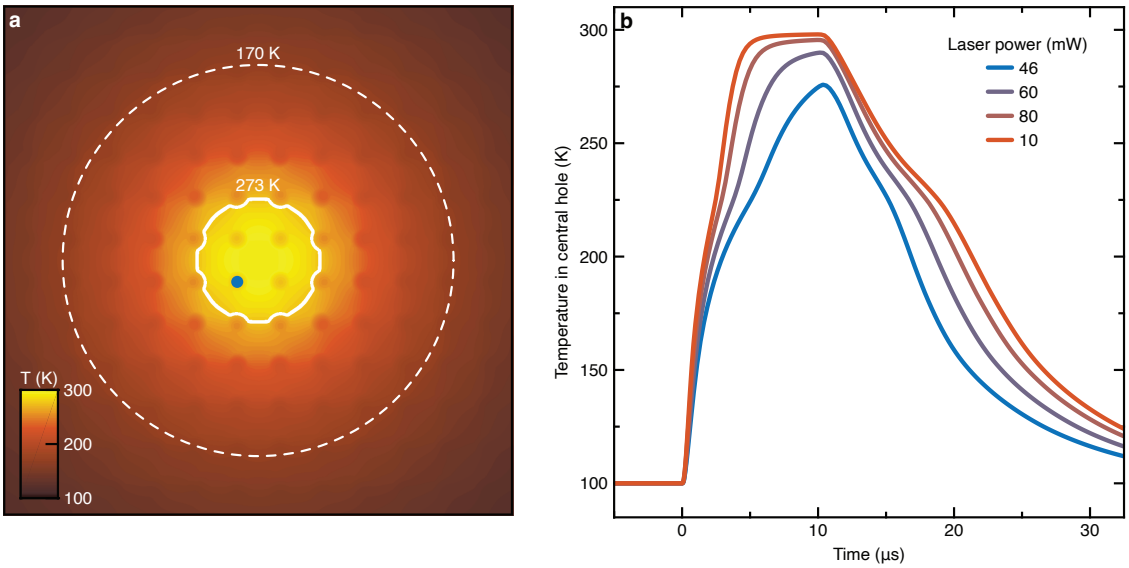

Adapted from Jonathan M. Voss, Oliver F. Harder, Pavel K. Olshin, Marcel Drabbels, Ulrich J. Lorenz, Structural Dynamics 8, 054302 (2021).

Figure 4. Visualized Results. (a) Heat map of grid square with point of interest marked by blue dot. (b) Temperature evolution sampled at blue point of interest for different laser powers.

In the context of this work, the heat transfer simulations serve three purposes. First, they allow to confirm experimental results independently, such as the timescales of heating and cooling determined by time-resolved cryo-EM. Second, they give better intuitive and qualitative understanding of what changes in experimental conditions such as a different grid geometry, substitution of materials or ice thickness would entail. Third, they allow us to predict the outcome of potential experiments by reading out temperatures, timescales and evaporation rates.

To extend the range or accuracy of the simulation, one improvement could be made. Evaporative cooling is implemented without accounting for the loss of mass. Once the water is boiled off completely, evaporative cooling should subside inducing further rapid heating. This change seems to be costly to implement with no prospective payoff aside from satisfying curiosity.

2.4 Ex-Situ UV-Irradiation

In Chapter 6, cryo-samples contain a photoactive compound (NPE-caged-proton) that needs to be activated by UV irradiation to drive pH-dependent protein dynamics.[29] For this purpose, an ex-situ UV Irradiation Setup was built using a UV laser and a LINKAM cryo-stage for correlative microscopy. Ex-situ irradiation provides greater flexibility in choice of laser or laser spot size as exchanging a laser, aligning it into the microscope and measuring parameters such as spot size is considerably more time consuming within the microscope.

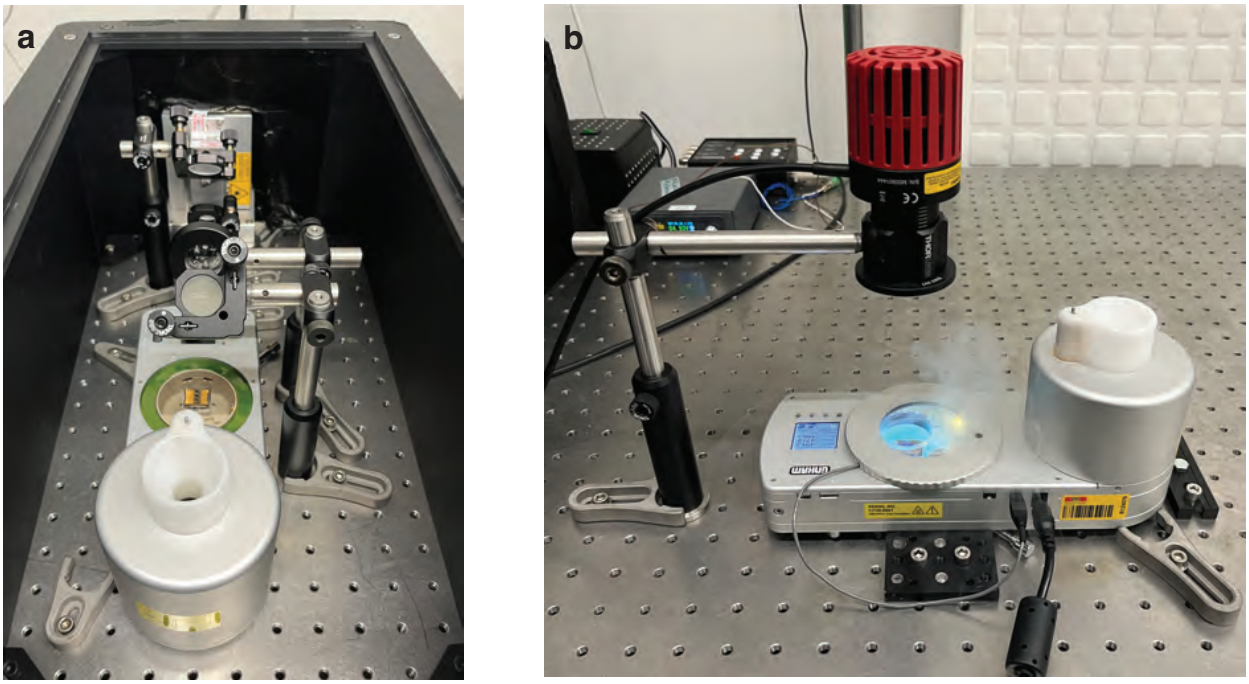

Figure 5. Experimental Setup for Ex-Situ UV-Irradiation. (a) View of the irradiation setup with a UV laser (266 nm), optics and the LINKAM cryo-stage in a protective enclosure. (b) Side view of LINKAM cryo-stage during a test irradiation with a photodiode (355 nm).

As depicted in Figure 5, the laser setup is enclosed by a protective laser box. TEM grids that have been plunge frozen beforehand are meticulously positioned within a cassette, which is then loaded onto a LINKAM cryo-stage, ensuring they remain within a protective atmosphere of nitrogen vapor cryogenic temperatures. These circumstances require the Dewar to be refilled every 15 minutes to maintain the atmosphere and temperatures.

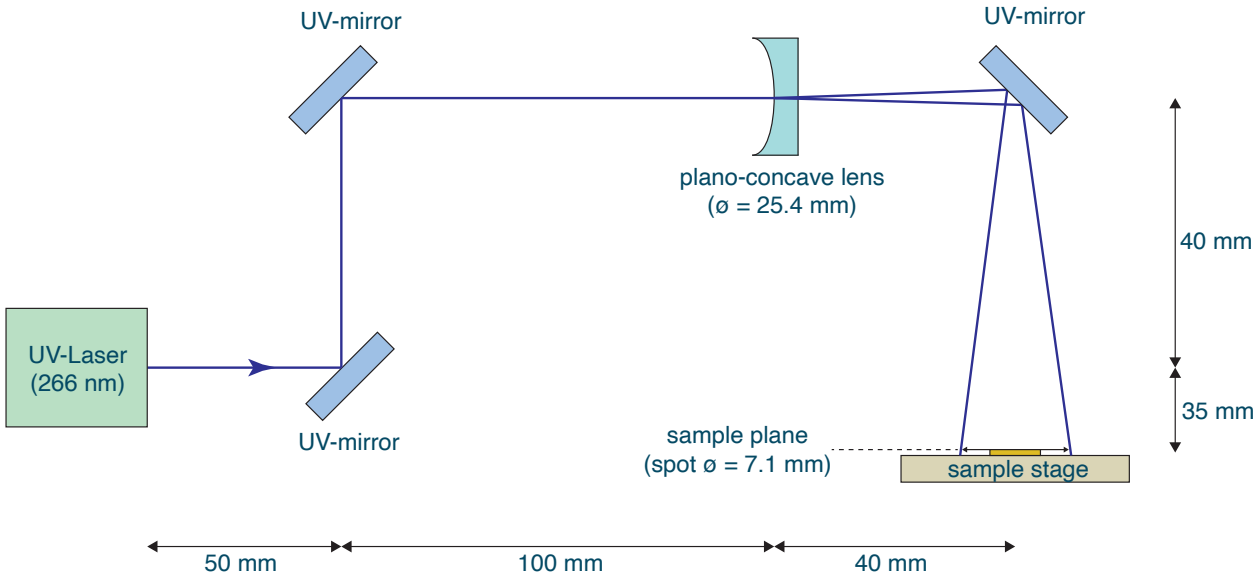

Figure 6. Schematic for Ex-Situ UV-Irradiation. Schematic view of the irradiation setup and the beam path taken by the UV laser light. The beam is guided up by two mirrors, defocused by a plano-concave lens (F=-30 mm) and then guided vertically onto the center of the sample/grid.

As depicted in Figure 6, a UV-laser (Bright Solutions Wedge 266 nm, laser power 35 mW, pulse width 1.5 ns, repetition rate 10 kHz) is directed normally onto the sample area of the cryo-stage using a plano-concave lens (Thorlabs LC4252, ø= 25.4 mm, F=-30 mm, AR Coated) and three dichroic UV-mirrors. The spot size in the sample plane (7.1 mm ±0.1 mm, knife-edge scan) can be adjusted via the placement of the plano-concave lens to comfortably exceed the size of a cryo-grid (around 3 mm) and allow quasi-uniform irradiation of the sample.

Photoactivation depends on the number of incident photons which was controlled by irradiation time while leaving other parameters such as spot size in sample plane, repetition rate or laser power invariant. Further chemical constraints depending on the photoactive compound have to be considered. NPE-caged-proton, for instance, can form intermediates that cannot be activated by UV. To drive significant pH changes with NPE-caged-proton, this setup required irradiation times ranging from 5 to 30 minutes.

In this setup, the pH was calibrated by irradiating 3 ul pearls of frozen sample solution emerged in liquid nitrogen and placing them on pH strips afterwards to melt. During the few seconds it takes the vitreous droplet to melt, moisture will be collected on the sample introducing a systematic measurement error which can be neglected due to the logarithmic nature of the pH scale. Experimentally, much higher irradiation times were determined than reported in literature for aqueous solution.[28 29] In the context of cryogenic samples this difference can be explained by a lower quantum efficiency in vitreous ice compared to liquid water.

Ex-Situ irradiation has major advantages compared to irradiation inside the microscope but further improvements should be made to enhance reliability: The sample transfer required additional steps where the samples have to be physically handled leaving room for error, contamination and sample damage. This could be addressed by mechanizing/automating part of the process or by switching to clipped grids designed to prevent damage to the foil. Progressively, this could be supported by optical elements (e.g. glasses or a small optical microscope) to increase visibility of the grid.

Lastly, identifying of ways to clean a grid would allow us to counteract contamination and reduce the fraction of grids that have to be discarded in the following steps. One way would be to introduce a washing stage where the liquid nitrogen is poured onto the grid. While effective, this step carries the downside of potential physical damage, already a major issue. An alternative is cleaning by dipping in liquid nitrogen such as during the autoloading process in a Titan Krios which would require additional mechanization/automation.

2.5 References

1. P. K. Olshin, M. Drabbels, U.J. Lorenz, Characterization of a time-resolved electron microscope with a Schottky field emission gun Struct Dyn 7, 054304 (2020).

2. F. Zemlin, K. Weiss, P. Schiske, W. Kunath, K.-H. Herrmann, Coma-free alignment of high resolution electron microscopes with the aid of optical diffractograms. Ultramicroscopy, Volume 3, 1978.

3. Y. Kayama, R.N. Burton-Smith, C. Song., et al., Below 3 Å structure of apoferritin using a multipurpose TEM with a side entry cryoholder, Sci. Rep. 2021, 11, 8395.

4. E.Y.D. Chua, J.H. Mendez, M. Rapp, S.L. Ilca, Y. Zi Tan, K. Maruthi, H. Kuang, C.M. Zimanyi, A. Cheng, E.T. Eng, A.J. Noble, C.S. Potter, B. Carragher, Better, Faster, Cheaper: Recent Advances in Cryo–Electron Microscopy. Annual Review of Biochemistry 2022 91:1, 1-32.

5. T. Nakane, A. Kotecha, A. Sente, G. McMullan, S. Masiulis, P.M.G.E Brown, I.T. Grigoras, L. Malinauskaite, T. Malinauskas, J. Miehling, T. Uchański, L. Yu, D. Karia, E.V. Pechnikova, E. de Jong, J. Keizer, M. Bischoff, J. McCormack, P. Tiemeijer, S.W. Hardwick, D.Y. Chirgadze, G. Murshudov, A.R. Aricescu, S.H.W. Scheres, Single-particle cryo-EM at atomic resolution. Nature. 2020 587 (7832):152-156.

6. S.H.W. Scheres, RELION: Implementation of a Bayesian approach to cryo-EM structure determination. Journal of Structural Biology, Volume 180, Issue 3, 2012.

7. A. Punjani, J.L. Rubinstein, D.J. Fleet, M.A. Brubaker, cryoSPARC: algorithms for rapid unsupervised cryo-EM structure determination. Nature methods 14 (3), 290-296, 2017.

8 A. Punjani, Algorithmic Advances in Single Particle Cryo-EM Data Processing Using CryoSPARC. Microscopy and Microanalysis, 26(S2), 2322-2323. (2020).

9 T.V. Hoang, X. Cavin, P. Schultz, et al., gEMpicker, a highly parallel GPU-accelerated particle picking tool for cryo-electron microscopy, BMC Struct Biol 13, 25 (2013).

10 F. Wang, H. Gong, G. Liu, M. Li, C. Yan, T. Xia, X. Li, J. Zeng, DeepPicker: A deep learning approach for fully automated particle picking in cryo-EM, Journal of Structural Biology Volume 195, Issue 3, 2016.

11 A. Punjani, H. Zhang, D.J. Fleet, Non-uniform refinement: adaptive regularization improves single-particle cryo-EM reconstruction, Nat Methods 17, 1214–1221 (2020).

12 A. Punjani, D.J. Fleet, 3D variability analysis: Resolving continuous flexibility and discrete heterogeneity from single particle cryo-EM, Journal of Structural Biology, Volume 213, Issue 2, 2021.

13 A.H. Zewail, Four-Dimensional Electron Microscopy. Science328,187-193 (2010).

14 C.R. Krüger, N.J. Mowry, G. Bongiovanni et al., Electron diffraction of deeply supercooled water in no man's land. Nat Communications 14, 2812 (2023).

15 B.E. Warren, X-Ray Diffraction, Dover Publications, New York, 1990.

16 COMSOL Multiphysics® v. 6.1. www.comsol.com. COMSOL AB, Stockholm, Sweden.

17 COMSOL Multiphysics Reference Manual, version 5.5", COMSOL, Inc, www.comsol.com

18 W. DeSorbo and W. W. Tyler, The specific heat of graphite from 13° to 300°K, The Journal of Chemical Physics, 1953, 21, 1660–1663.

19 E. Pop, V. Varshney and A.K. Roy, Thermal properties of graphene: Fundamentals and applications, MRS Bulletin, 2012, 37, 1273–1281.

20 A.A. Balandin, Thermal properties of graphene and nanostructured carbon materials, Nat. Mater. 10 (2011) 569–581.

21 J.W. Arblaster, Thermodynamic properties of gold, J. Phase Equilib. Diffus., 2016, 37, 229–245.

22 J. Huang, Y. Zhang and J.K. Chen, Ultrafast solid–liquid–vapor phase change of a gold film induced by pico- to femtosecond lasers, Applied Physics A, 2009, 95, 643–653.

23 S. Maruyama, K. Wakabayashi and M. Oguni, Thermal properties of supercooled water confined within silica gel pores, AIP Conference Proceedings, 2004, 708, 675–676.

24 O. Andersson and H. Suga, Thermal conductivity of low-density amorphous ice, Solid State Commun., 1994, 91, 985–988.

25 M. Fuchs, E. Dayan, E. Presnov, Evaporative cooling of a ventilated greenhouse rose crop. Agric. For. Meteorol. 138, 203–215 (2006).

26 J.D. Smith, C.D. Cappa, W.S. Drisdell, R.C. Cohen and R.J. Saykally, Raman thermometry measurements of free evaporation from liquid water droplets, J. Am. Chem. Soc., 2006, 128, 12892– 12898.

27 R.J. List, Ed., Smithsonian Meteorological Tables, Smithsonian Institution Press, Washington, 1968.

28 O. Andersson and H. Suga, Thermal conductivity of low-density amorphous ice, Solid State Commun., 1994, 91, 985–988.

29 A. Barth, J.E.T. Corrie: Characterization of a New Caged Proton Capable of Inducing Large pH Jumps. Biophysical Journal, Volume 83, Issue 5, 2002, Pages 2864-2871.

30 S. Abbruzzetti, S. Sottini, C. Viappiani, and J.E. T. Corrie, Kinetics of Proton Release after Flash Photolysis of 1-(2-Nitrophenyl)ethyl Sulfate (Caged Sulfate) in Aqueous Solution, Journal of the American Chemical Society, 2005, 127 (27), 9865-9874.

Chapter 3: *Rapid Melting and Revitrification as an Approach to Microsecond Time-Resolved Cryo-Electron Microscopy*[1]

3.1 Introduction

Proteins perform a range of tasks that are quintessential for life. They are involved in harvesting energy, maintaining homeostasis, catalyzing metabolic reactions, reproduction, and sensing stimuli. As nanoscale machines, proteins are dynamic systems whose free energy surface determines their motions and characteristic timescales.[1] Backbone motions and side-chain rotations involve transitions between minima separated by small barriers and typically occur on picosecond to nanosecond timescales, leading to fast, small-amplitude fluctuations of the protein structure.[2] In contrast, the dynamics associated with the activity of a protein frequently involve large-amplitude motions of entire domains that occur on a timescale of microseconds to milliseconds.[1 2]

Much of our knowledge about protein function derives from static structures at atomic resolution, which frequently allow one to infer function, particularly if structures of different functional states can be obtained.[3 - 6] However, in the absence of real-time observations, our understanding of proteins is necessarily incomplete. Directly observing proteins as they perform their tasks, in real time and at atomic resolution, holds the promise of fundamentally advancing our grasp of these nanoscale machines.[1]

X-ray crystallography has long been the most important tool in structural biology.[7] Recently, the advent of bright x-ray pulses has also made it possible to carry out time-resolved experiments, even with ultrafast time resolution.[8 9] However, the requirement of a crystalline sample poses a specific challenge for studying the dynamics of proteins, as the crystal packing hinders large-amplitude motions.[10 11 12] In contrast, single-

[1] Reproduced with small adaptations from Jonathan M. Voss, Oliver F. Harder, Pavel K. Olshin, Marcel Drabbels, Ulrich J. Lorenz, Chem. Phys. Lett., 2021, 778, 138812.

Personal contribution to this chapter: Together with Jonathan Voss, I learned the preparation of cryo-samples, the handling of cryo-equipment and the operation of a cryo-electron microscope from Davide Demurtas at CIME. With Jon, I also discovered the experimental approach of rapidly melting and revitrifiying cryo-samples in the vacuum of an electron microscope allowing us to avoid the enclosing graphene. Together, we collected the presented cryo-EM data. Lastly, I supported the preparation of this manuscript.

I'd like to stress, that the characterization of the time-scales of the laser-heating without the presence of vitreous ice had been carried out by Jonathan Voss, Christoph Schillai and Pavel Olshin before I joined the team.

particle cryo-electron microscopy (cryo-EM) [13 - 19] enables the observation of biological specimens in their frozen hydrated state.[20 21] The revolution that the field has recently undergone has also created new opportunities for obtaining time-resolved information.[22 23] In time-resolved cryo-EM, dynamics are induced by mixing two reactants [24 25 26] or exposing the sample to a short light pulse.[27 28] Short-lived intermediates are then trapped in vitreous ice by promptly plunge freezing the sample. However, with a time resolution of several milliseconds [22], which is ultimately limited by the timescales for plunging (~5 ms)[28] and vitrification (~1 ms) [21], this technique is currently too slow to capture many relevant processes.

Here, we propose a novel approach for carrying out time-resolved cryo-EM with microsecond time resolution. The concept (Fig. 1a–e) is based on rapidly melting a vitrified sample *in situ* with a heating laser (Fig. 1a). Once in their native liquid environment at room temperature (Fig. 1b), the embedded particles are subjected to an external stimulus that induces dynamics (Fig. 1c). For example, a second laser pulse can be used to photoactivate a caged compound and liberate ATP or a small peptide that interacts with the protein.[29 30] In the simplest case, the heating laser itself can be used to create a temperature jump to initiate conformational dynamics. At a well-defined point in time, the heating laser is switched off to induce rapid revitrification and trap the particles in their transient configurations (Fig. 1d), so that they can be subsequently characterized with established cryo-EM techniques (Fig. 1e).

It is not obvious that implementing such a scheme should be possible. Usually, warming up a cryo sample is scrupulously avoided in order to prevent devitrification. Here, we demonstrate that this obstacle can be overcome. We employ cryo samples with a holey gold film [31] supported by a gold mesh. For some experiments, we additionally sandwich the sample between two sheets of few layer graphene, as illustrated in Fig. 1f (Note S1 and Fig. S1), so as to reduce evaporation of the liquid water in the vacuum of the microscope.[32] The sample is heated *in situ* with a laser pulse of tens of microseconds duration (532 nm, 24 μm FWHM spot size), which we obtain by chopping the output of a continuous laser with an acousto-optic modulator (Note S3 and Fig. S2).[33] The gold film and graphene sheets strongly absorb at the laser wavelength and serve as the heat source to melt the ice. In contrast, neither the proteins nor the ice absorb the laser radiation, which prevents photodamage to the specimen. In all experiments, we have centered the heating laser onto the area under observation.

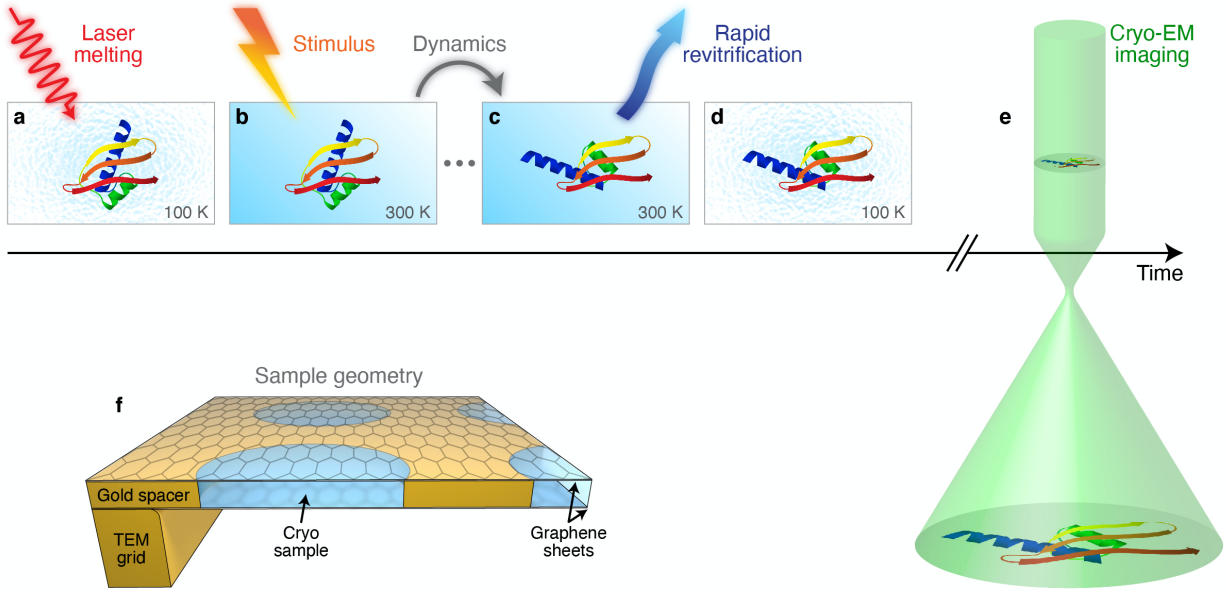

Fig. 1. Experimental concept and sample geometry. (a–e) Illustration of rapid *in situ* melting and revitrification for time-resolved cryo-EM. (a) A cryo sample is melted *in situ* with a heating laser. (b) Once the sample is liquid and has reached room temperature, dynamics of the embedded particles are induced with an external stimulus, *e.g.* a short second laser pulse that releases a caged compound such as ATP or a peptide. (c) While the particle undergoes conformational changes, the heating laser is switched off at a given point in time so that the sample rapidly cools and revitrifies. (d) The particle is trapped in its transient configuration and can be subsequently imaged with conventional cryo-EM techniques (e). (f) Illustration of the sample geometry. A cryo sample supported by a holey gold film is enclosed between two graphene layers, which prevent evaporation in the vacuum of the microscope as the sample is melted *in situ* with a laser pulse.

3.2 Results and Discussion

Rapid *in situ* melting and vitrification

We first demonstrate that it is indeed possible to melt a cryo sample *in situ* and subsequently achieve rapid vitrification. To this end, we intentionally prepare crystalline ice samples, which allows us to directly verify the success of the experiment. Fig. 2a shows a thin ice sheet held at 100 K that is suspended over a hole of the gold film and enclosed between graphene layers. Bend contours are visible, indicating that the ice sheet is crystalline. This is confirmed by the diffraction pattern, which exhibits the signature of hexagonal ice (Fig. 2b).[21] When we irradiate the sample with an individual 20 µs laser pulse with a power of 25 mW, the diffraction pattern remains largely unchanged (Fig. 2c), indicating that the sample has not melted. Laser pulses of up to 63 mW yield the same result (Fig. 2d–g).

However, a single pulse with a power of 75 mW provides sufficient heat to induce melting (Fig. 2h). Most of the ice sheet now exhibits homogeneous contrast, with the diffraction pattern revealing the signature of vitreous ice (Fig. 2i, selected area marked by the green circle in Fig. 2h).[21] In the top left of the sample, a small void has formed. We observe such voids if defects in the graphene sheets allow liquid water to evaporate. The lighter contrast on the right side of the sample indicates an area where some ice has remained crystalline, as a selected area diffraction pattern reveals (Fig. 2i inset, selected area indicated with a grey circle in Fig. 2h). Evidently, at this laser power, the ice sheet barely reaches the melting point and remains partially crystalline. Incrementally increasing the laser power thus provides an *in situ* calibration of the power required for melting.

For the experiment illustrated in Fig. 3a–d, the threshold laser power for melting and vitrification was first calibrated in a different area of the sample. When we use this power to heat the crystalline sample in Fig. 3a,b, melting and vitrification is achieved with a single laser pulse (Fig. 3c,d). The uniform contrast suggests that here, the ice film suspended across the hole has completely vitrified. We note that the laser power needed to induce melting is lower than in Fig. 2, where the sample is in close proximity to the bars of the TEM grid. Heat transfer simulations agree with this observation, showing that the required power increases closer to the bars (Note S4 and Fig. S3).

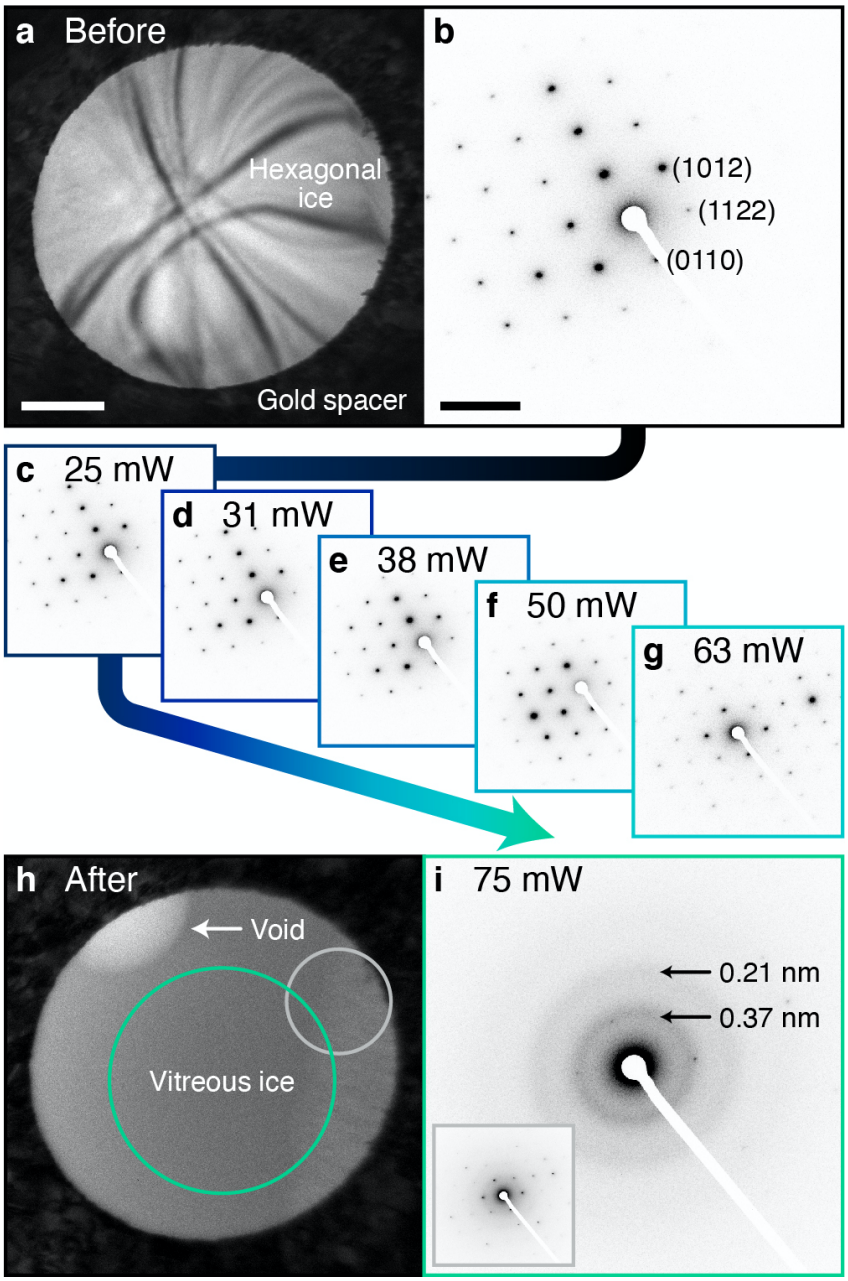

Fig. 2. Determination of the laser power required for *in situ* melting and vitrification. (a) Micrograph and (b) selected area diffraction pattern of a thin film of hexagonal ice. (c–g) The sample is irradiated with individual laser pulses of 20 μs duration. As the laser power is increased up to 63 mW, the diffraction pattern remains largely unchanged, indicating that melting has not occurred. (h,i) A single pulse with a power of 75 mW provides sufficient heat to melt the sample, which then rapidly vitrifies after the end of the laser pulse. Scale bars, 300 nm and 4 nm^{-1}.

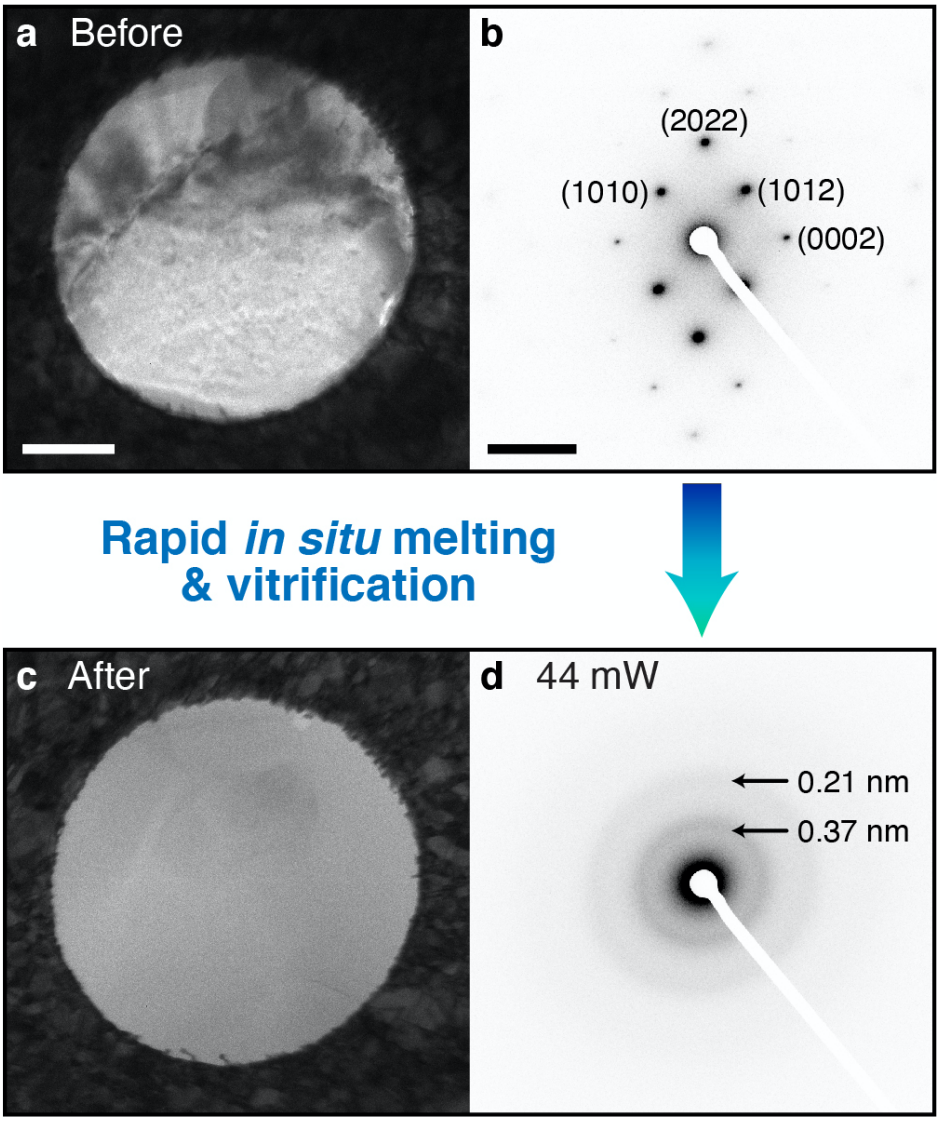

Fig. 3. *In situ* melting and vitrification with a single laser pulse. (a) Micrograph and (b) selected area diffraction pattern of a thin film of hexagonal ice. (c,d) After calibration of the laser power in a different area, the sample is successfully melted and vitrified with a single laser pulse. Scale bars, 300 nm and 4 nm^{-1}.

Characterization of the temperature evolution and time resolution

For the purpose of time-resolved cryo-EM experiments, it is crucial to have a detailed understanding of the temperature evolution of the sample, which ultimately determines the attainable time resolution. We therefore characterize the heating and cooling dynamics *in situ* with time-resolved electron microscopy (Note S5 and Fig. S2).[34 - 38] We heat the sample in Fig. 4a, which is held at 100 K, with a 20 μs laser pulse (13 mW). To probe its temperature at a specific point in time, we record a time-resolved diffraction pattern of a selected area of the gold film with a 1 ns electron pulse (~10^4 electrons).

The diffraction intensity of the gold film decreases exponentially with temperature and therefore provides a suitable probe of the sample temperature (Debye-Waller behavior [39]). We then repeat the experiment stroboscopically (1 kHz repetition rate) to probe the temperature at different points in time. Since a thin layer of ice would not be stable under illumination with thousands of laser pulses, we perform the experiment in the area shown in Fig. 4a, which is not covered by ice. Nevertheless, the temperature evolution of the bare gold film provides a good approximation of the heating and cooling dynamics of a cryo sample. As discussed in detail below, simulations confirm that the presence of a thin ice film barely alters the temperature evolution. Moreover, the ice and the underlying gold film have near-identical temperatures.

Fig. 4b shows a diffraction pattern of the holey gold film collected from the area marked with a red dot in Fig. 4a, onto which we have also aligned the heating laser. As the laser warms the sample, the diffraction intensity decreases quickly, as shown for the (331), (420), and (422) reflections in Fig. 4c. After only a few microseconds, the temperature in the selected area stabilizes, increasing only slightly over time. When the heating laser is switched off at 20 μs, the sample promptly recools as it dissipates heat towards its surroundings, which have remained at cryogenic temperature. From exponential fits (solid red curve, Note S6,7), we obtain heating and cooling times of 1.2 μs and 3.6 μs, respectively. Similar timescales are obtained in different areas of the sample (orange and yellow dots in Fig. 4a and Fig. S4e,f).

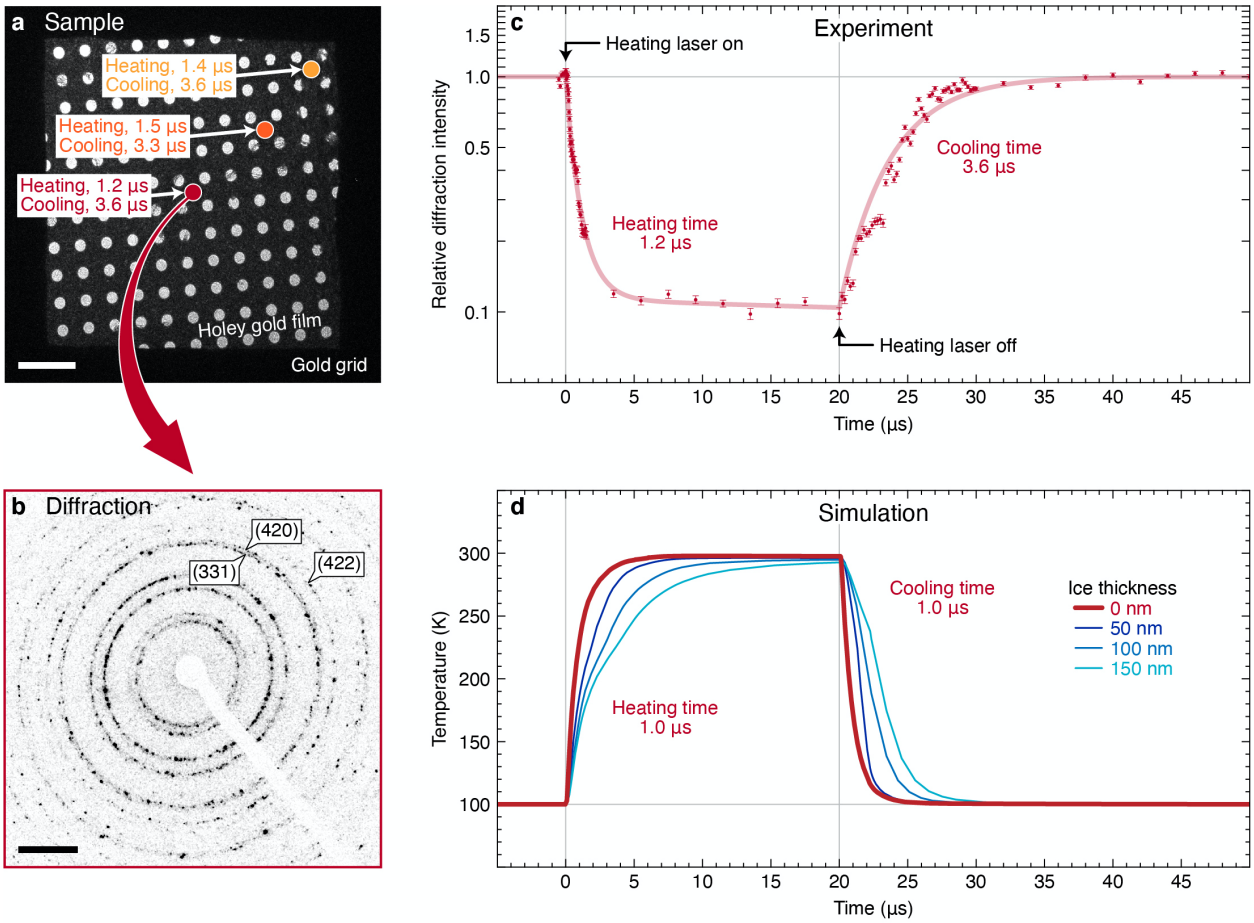

Fig. 4. Characterization of the temperature evolution of the sample under illumination with microsecond laser pulses. (a) Micrograph of the sample in an area that is free of ice. Heating and cooling timescales of the gold film were measured at three different positions (dots), onto which the laser was focused. Scale bar, 5 µm. (b) Selected area diffraction pattern of the area marked with a red dot in (a). Scale bar, 5 nm^{-1}. (c) Temporal evolution of the intensity of the (331), (420), and (422) reflections in (b) under irradiation with a 20 µs laser pulse (dots). Heating and cooling times of 1.2 µs and 3.6 µs, respectively, are determined from fits with exponential functions (solid curve). The error bars represent the standard error. (d) A simulation of the temperature evolution of the sample in (c) yields similar heating and cooling times of 1.0 µs (solid red curve). In the presence of a layer of vitreous ice (blue curves), heating and cooling times increase, while the maximum temperature at which the sample stabilizes barely changes.

Heat transfer simulations (Note S4 and Fig. S3) reproduce these timescales reasonably well, yielding 1.0 μs heating and cooling times (Fig. 4d, solid red curve). If we add a thin layer of vitreous ice, its temperature (blue curves) closely follows that of the underlying gold film, with which it is in close contact. With increasing ice thickness, the heating and cooling times become longer. However, the temperature at which the sample stabilizes during the laser pulse barely changes. We find that the sample temperature plateaus at 300 K for a laser power of 35 mW (Fig. 4d), which is in reasonable agreement with the experimentally determined power that induces melting.

It may appear counterintuitive that melting a cryo sample *in situ* should result in vitrification, since heating up a vitreous sample ordinarily causes irreversible crystallization.[40] The characterization of the temperature evolution reveals that this is made possible by the high heating and cooling rates of nearly 10^8 K/s, which is more than two orders of magnitude faster than what is required to outrun crystallization and achieve vitrification.[41 42] Several factors enable such fast cooling. The tightly focused laser beam heats the sample only locally, so that after the laser pulse, the heat can be rapidly dissipated to adjacent areas that have remained at cryogenic temperature.

Our simulations also reveal that the bars of the specimen grid play an important role in this respect. Due to their large heat capacity, they barely warm up and therefore act as an effective heat sink. Crucially, the cooling rate also determines how fast the dynamics of embedded particles can be arrested, which occurs when the sample is cooled below the glass transition temperature of water at 137 K.[43 44] We conclude that for ice thicknesses suitable for cryo-EM, our approach yields a time resolution of 5 μs or better, three orders of magnitude faster than what is currently possible with time-resolved cryo-EM.[22] Importantly, this matches the time resolution of cryo-EM to the characteristic timescale on which the relevant dynamics of most proteins occur.[1 2] Snapshots of the dynamics at different points in time can then be acquired by simply changing the duration of the heating laser pulse.

Proof of principle experiment

As a proof of principle, we study the rapid disassembly of the GroEL protein complex [45] in response to structural damage that we induce through electron beam irradiation. It is well-known that proteins are heavily damaged during cryo-imaging with typical electron doses.[46 47] However, the cryogenic matrix traps fragments in place and thus limits structural degradation, which would otherwise render high-resolution imaging impossible.[46 47] In a liquid environment, however, structural changes can freely occur. Melting a cryo sample *in situ* after it has been exposed to a significant electron dose should therefore allow the damaged proteins to unravel.

Fig. 5a shows a cryo sample of GroEL on a holey gold film, imaged with a dose of 14 electrons/Å^2. Here, we have illuminated only the top part, so that particles in the unexposed area do not incur any beam damage and can serve as a control. For simplicity, the sample is not enclosed between graphene sheets. Even though this allows some water to evaporate during laser heating, it is still possible to carry out experiments with laser pulse durations of tens of microseconds without evaporating the entire sample. In order to allow dynamics of the beam-damaged GroEL to occur, we melt the sample with a 10 μs laser pulse, after which it revitrifies, arresting the particles in their transient configurations (Fig. 5b).

The irradiated area (dashed line) appears lighter than the remainder of the sample, a phenomenon that we consistently observe, but that is absent without electron beam exposure. This suggests that this area has thinned as volatile radiolysis products trapped in the ice [47] were liberated during the melting process (see also Fig. S5). The proteins are no longer visible in this area, indicating that they have disintegrated, leaving only fragments that offer little contrast. A few larger fragments are visible near the edge of the irradiated area (red arrows). The proteins in the bottom part of the image, which had not been exposed to the electron beam, have remained intact. This demonstrates that the disintegration of GroEL particles we observe is caused by electron beam irradiation and not the melting and revitrification process.

Disassembly dynamics of GroEL (high electron dose)

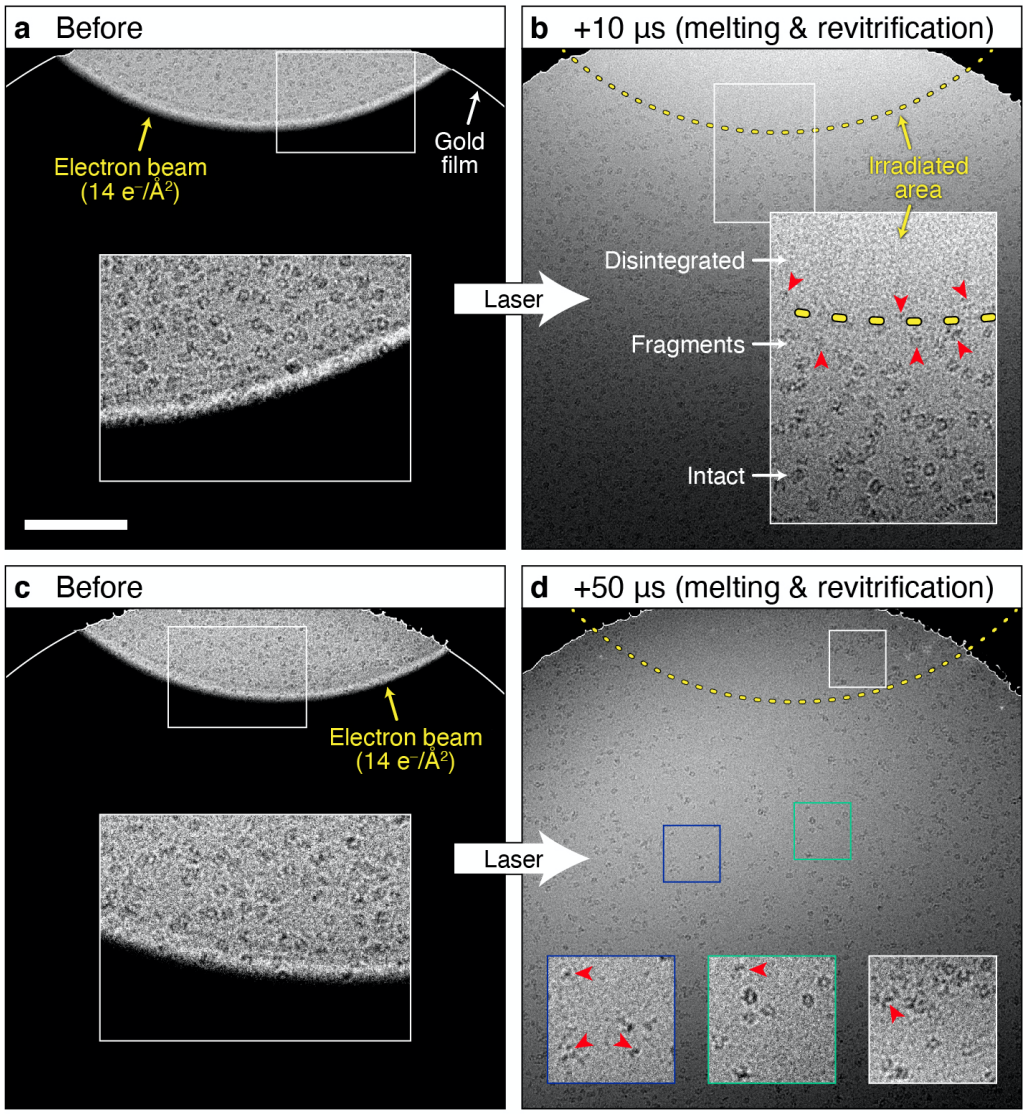

Disassembly dynamics of GroEL (low electron dose)

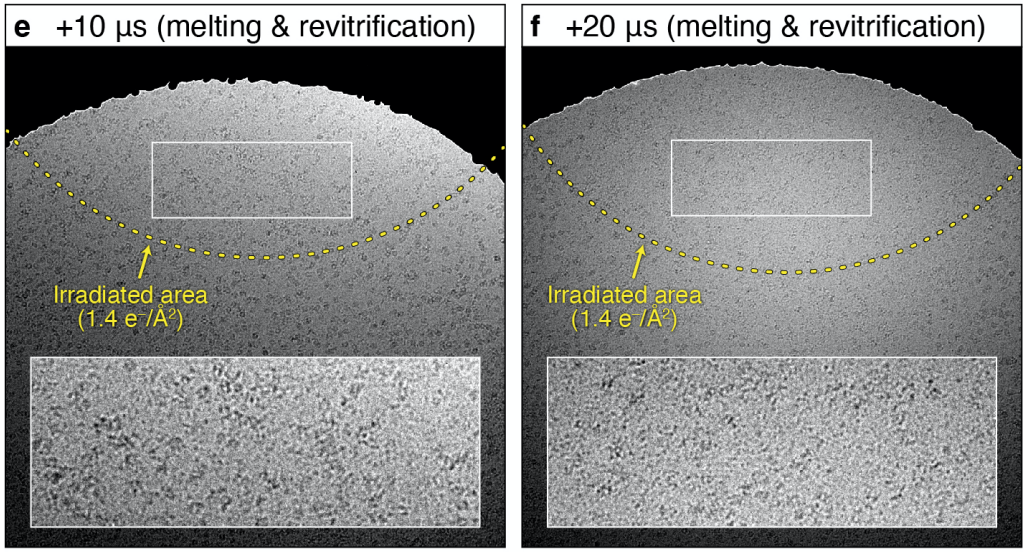

Fig. 5. Microsecond time-resolved cryo-EM of the rapid disassembly of GroEL following electron beam damage. (a) Micrograph of GroEL on a holey gold film. Only the top part is illuminated with the electron beam (14 electrons/Å^2) in order to limit beam damage to particles in that area. The lines sketch the outline of the hole of the gold film. (b) The sample is melted with a 10 μs laser pulse *in situ*, allowing the damaged GroEL particles to unravel. After the laser pulse, the sample revitrifies, trapping particles in their transient configurations. The dashed line delineates the sample area that was irradiated in (a). The red arrows highlight protein fragments that are visible at the boundary of the irradiated area. (c,d) The experiment in (a,b) is repeated with a 50 μs laser pulse. (e,f) The electron beam damage inflicted on the GroEL particles is reduced by lowering the electron dose to 1.4 electrons/Å^2. Melting the sample with a laser pulse of 10 μs (e) and 20 μs duration (f) traps the particles in different stages of the disassembly process. In the insets, the contrast has been adjusted to make the particles more easily visible. Scale bar, 250 nm.

The effect of exposure to the electron beam appears to extend beyond the irradiated area. In its immediate vicinity, the particle density is lower, and partially disassembled proteins as well as fragments are visible (red arrows). A possible explanation is that melting liberates highly reactive radiolysis products trapped in the ice, such as OH and H radicals, protons, and solvated electrons.[47] The diffusion lengths of these species within the laser pulse duration of 10 μs are hundreds of nanometers [48], suggesting that they will reach intact GroEL particles and damage them. It is also possible that convective flow of the water film occurs as areas of different thickness equilibrate. With increasing duration of the heating laser pulse, convection seems to play a larger role since the spatial distributions of intact particles and fragments are increasingly reshuffled, as shown for a 30 μs laser pulse in Fig. S5. After irradiation with a 50 μs laser pulse (Fig. 5c,d), the ice thickness is almost homogeneous across the hole in the gold film, with intact particles and fragments visible in both the exposed and unexposed areas (Fig. 5d, insets).

We note that the disintegration of the proteins observed in Fig. 5d does not result from the laser irradiation, but is only present if the sample has first been exposed to the electron beam. This is evidenced by Fig. S6, which shows a neighboring hole of the gold film that had not been irradiated by the electron beam. The particles in this hole are intact, even though they were exposed to a near-identical laser intensity

and reached a similar temperature (the FWHM of the Gaussian laser spot, which is centered on the sample, is more than an order of magnitude larger than the distance separating the holes).

Lowering the electron dose reduces the damage inflicted on the GroEL particles, so that their disintegration proceeds more slowly, allowing us to take snapshots of different stages. If we irradiate the sample with only 1.4 electrons/Å^2 (Fig. S7), the particles do not disintegrate entirely when the sample is melted with a 10 μs laser pulse (Fig. 5e). Instead, a large number of damaged proteins and fragments remain visible in the exposed area. Increasing the laser pulse duration to 20 μs allows the disassembly to proceed further (Fig. 5f). Few particles remain that resemble intact GroEL, while the size of the fragments has further decreased. We note that we have adjusted the laser power with the procedure described in Fig. 2, so that we can be certain that the plateau temperature of the sample exceeds the melting point of ice. Moreover, heat transfer simulations show that for the particular sample geometry used here, evaporative cooling limits the plateau temperature, so that it should not exceed room temperature for the laser powers employed (Fig. S8).

3.3 Conclusions and Outlook

We have demonstrated that it is possible to rapidly laser melt and revitrify a cryo sample *in situ*, so that particle dynamics can occur in liquid for a well-defined amount of time. This opens up the perspective of carrying out microsecond time-resolved cryo-EM experiments. In a proof of principle experiment, we have observed the disassembly of GroEL following electron beam damage, which reveals a surprising insight about cryo-imaging. Even at a dose as low as 1.4 electrons/Å^2, damage to the particles is so extensive that once the vitreous ice matrix that preserves their shape is melted, they completely disintegrate. These initial results suggest that our method may be applicable to a wider range of processes.

For instance, it is straightforward to implement temperature jump experiments by adjusting the laser power to heat the sample well above room temperature, which should make it possible to study folding and unfolding dynamics. Another possibility is to trigger dynamics with an additional laser pulse once the sample reaches room temperature. In the case of a photoactive protein, the laser pulse itself can initiate the dynamics.[8 49] Alternatively, it can provide a biomimetic trigger by dissociating a photo-activated caged compound to release ions, ATP, or small peptides, or to induce a pH jump.[29 30 50] Such experiments could be simplified by activating the photorelease compounds already in the vitreous state of the sample. Since the proteins are unable to undergo dynamics in the vitreous ice matrix, the trigger can only become active once the sample is melted. We have in fact demonstrated such a scheme in the experiments of Fig. 5, where the trigger, electron beam irradiation, was applied before *in situ* melting.

Precise control of the sample temperature will be crucial for such experiments to succeed. The laser power needed to reach a given sample temperature can be calibrated *in situ* by determining the threshold power for melting (Fig. 2). Fortunately, small variations in the thickness of the ice layer do not change the plateau temperature of the sample (Fig. 4d). This is particularly true for samples not enclosed in graphene, for which evaporative cooling stabilizes the temperature.

3.4 References

1. K. Henzler-Wildman, D. Kern, Dynamic personalities of proteins, Nature, 2007, 450, 964-972.

2. D.D. Boehr, H.J. Dyson, P.E. Wright, An NMR perspective on enzyme dynamics, Chem. Rev., 2006, 106, 3055–3079.

3. J. Frank, Conformational Proteomics of Macromolecular Architecture: Approaching the Structure of Large Molecular Assemblies and Their Mechanisms of Action Ch. 13, World Scientific, Singapore, 2004.

4. J. Frank, Three-Dimensional Electron Microscopy of Macromolecular Assemblies: Visualization of Biological Molecules in Their Native State, Oxford University Press, New York, 2006.

5. E. Cao, M. Liao, Y. Cheng, D. Julius, TRPV1 structures in distinct conformations reveal activation mechanisms, Nature, 2013, 504, 113–118.

6. J. Zhao, S. Benlekbir, J.L. Rubinstein, Electron cryomicroscopy observation of rotational states in a eukaryotic V-ATPase, Nature, 2015, 521, 241–245.

7. Y. Shi, A glimpse of structural biology through x-ray crystallography, Cell, 2014, 159, 995–1014.

8. F. Schotte, M. Lim, T.A. Jackson, A.V. Smirnov, J. Soman, J.S. Olson, G.N.Jr. Phillips, M. Wulff, P.A. Anfinrud, Watching a protein as it functions with 150-ps time-resolved x-ray crystallography, Science, 2003, 300, 1944–1947.

9. K. Pande, C.D.M. Hutchison, G. Groenhof, A. Aquila, J.S. Robinson, J. Tenboer, S. Basu, S. Boutet, D.P. DePonte, M. Liang, T.A. White, N.A. Zatsepin, O. Yefanov, D. Morozov, D. Oberthuer, C. Gati, G. Subramanian, D. James, Y. Zhao, J. Koralek, J. Brayshaw, C. Kupitz, C. Conrad, S. Roy-Chowdhury, J.D. Coe, M. Metz, P.L. Xavier, T.D. Grant, J.E. Koglin, G. Ketawala, R. Fromme, V. rajer, R. Henning, J.C.H. Spence, A. Ourmazd, P. Schwander, U. Weierstall, M. Frank, P. Fromme, A. Barty, H.N. Chapman, K. Moffat, J.J. van Thor, M. Schmidt, Femtosecond structural dynamics drives the trans/cis isomerization in photoactive yellow protein, Science, 2016, 352, 725–729.

10. S. Skou, R.E. Gillilan, N. Ando, Synchrotron-based small-angle x-ray scattering of proteins in solution, Nat. Protoc., 2014, 9, 1727–1739.

11. S.P. Meisburger, W.C. Thomas, M.B. Watkins, N. Ando, X-ray scattering studies of protein structural dynamics, Chem. Rev., 2017, 117, 7615–7672.

12. M.C. Deller, L. Kong, B. Rupp, Protein stability: a crystallographer's perspective, Acta Cryst. F72, 2016, 72–95.

13. X. Li, P. Mooney, S. Zheng, C.R. Booth, M.B. Braunfeld, S. Gubbens, D.A. Agard, Y. Cheng, Electron counting and beam-induced motion correction enable near-atomic-resolution single-particle cryo-EM, Nat. Methods, 2013, 10, 584–590.

14. W. Kuhlbrandt, The resolution revolution, Science, 2014, 343, 1443–1444.

15. R. Henderson, Overview and future of single particle electron cryomicroscopy, Arch. Biochem. Biophys., 2015, 581, 19–24.

16. Y. Cheng, N. Grigorieff, P.A. Penczek, T. Walz, A primer to single-particle cryo-electron microscopy, Cell., 2015, 161, 438–449.

17. X. Bai, G. McMullan, S.H.W. Scheres, How cryo-EM is revolutionizing structural biology, Trends Biochem. Sci., 2015, 40, 49–57.

18. A. Merk, A. Bartesaghi, S. Banerjee, V. Falconieri, P. Rao, M.I. Davis, R. Pragani, M.B. Boxer, L.A. Earl, J.L.S. Milne, S. Subramaniam, Breaking cryo-EM resolution barriers to facilitate drug discovery, Cell., 2016, 165, 1698–1707.

19. E. Nogales, The development of cryo-EM into a mainstream structural biology technique, Nat. Methods, 2016, 13, 24–27.

20. M. Adrian, J. Dubochet, J. Lepault, A.W. McDowall, Cryo-electron microscopy of viruses, Nature, 1984, 308, 32–36.

21. J. Dubochet, M. Adrian, J.-J. Chang, J.-C. Homo, J. Lepault, A.W. McDowall, P. Schultz, Cryo-electron microscopy of vitrified specimens, Q. Rev. Biophys., 1988, 21, 129–228.

22. B. Chen, J. Frank, Two promising future developments of cryo-EM: capturing short-lived states and mapping a continuum of states of a macromolecule, Microscopy, 2016, 65, 69–79.

23. J. Frank, Time-resolved cryo-electron microscopy: Recent progress, J. Struct. Biol., 2017, 200, 303–306.

24. Z. Lu, T.R. Shaikh, D. Barnard, X. Meng, H. Mohamed, A. Yassin, C.A. Mannella, R.K. Agrawal, T.-M. Lu, T. Wagenknecht, Monolithic microfluidic mixing–spraying devices for time-resolved cryo-electron microscopy, J. Struct. Biol., 2009, 168, 388–395.

25. T.R. Shaikh, A.S. Yassin, Z. Lu, D. Barnard, X. Meng, T.-M. Lu, T. Wagenknecht, R.K. Agrawal, Initial bridges between two ribosomal subunits are formed within 9.4 milliseconds, as studied by time-resolved cryo-EM, Proc. Natl. Acad. Sci., 2014, 111, 9822–9827.

26. V.P. Dandey, W.C. Budell, H. Wei, D. Bobe, K. Maruthi, M. Kopylov, E.T. Eng, P.A. Kahn, J.E. Hinshaw, N. Kundu, C.M. Nimigean, C. Fan, N. Sukomon, S.A. Darst, R.M. Saecker, J. Chen, B. Malone, C.S. Potter, B. Carragher, Time-resolved cryo-EM using Spotiton, Nat. Methods, 2020, 17, 897–900.

27. J.F. Menetret, W. Hofmann, R.R. Schroder, G. Rapp, R.S. Goody, Time-resolved cryo-electron microscopic study of the dissociation of actomyosin induced by photolysis of photolabile nucleotides, J. Mol. Biol., 1991, 219, 139–144.

28. T.R. Shaikh, D. Barnard, X. Meng, T. Wagenknecht, Implementation of a flash-photolysis system for time-resolved cryo-electron microscopy, J. Struct. Biol., 2009, 165, 184–189.

29. G.C.R. Ellis-Davies, Caged compounds: photorelease technology for control of cellular chemistry and physiology, Nat. Methods, 2007, 4, 619–628.

30. Y. Shigeri, Y. Tatsu, N. Yumoto, Synthesis and application of caged peptides and proteins, Pharmacol. Ther., 2001, 91, 85–92.

31. C.J. Russo, L.A. Passmore, Ultrastable gold substrates for electron cryomicroscopy, Science, 2014, 346, 1377–1380.

32. J.M. Yuk, J. Park, P. Ercius, K. Kim, D.J. Hellebusch, M.F. Crommie, J.Y. Lee, A. Zettl, A.P. Alivisatos, High-resolution EM of colloidal nanocrystal growth using graphene liquid cells, Science, 2012, 336, 61–64.

33. P.K. Olshin, M. Drabbels, U.J. Lorenz, Characterization of a time-resolved electron microscope with a Schottky field emission gun, Struct. Dyn., 2020, 7, 054304.

34. A.H. Zewail, Four-dimensional electron microscopy, Science, 2010, 328, 187–193.

35. U.J. Lorenz, A.H. Zewail, Observing liquid flow in nanotubes by 4D electron microscopy, Science, 2014, 344, 1496–1500.

36. R.J.D. Miller, Femtosecond crystallography with ultrabright electrons and x-rays: capturing chemistry in action, Science, 2014, 343, 1108–1116.

37. A. Feist, K.E. Echternkamp, J. Schauss, S.V. Yalunin, S. Schäfer, C. Ropers, Quantum coherent optical phase modulation in an ultrafast transmission electron microscope, Nature, 2015, 521, 200–203.

38. S.K. Sinha, A. Khammari, M. Picher, F. Roulland, N. Viart, T. LaGrange, F. Banhart, Nanosecond electron pulses in the analytical electron microscopy of a fast irreversible chemical reaction, Nat. Commun., 2019, 10, 3648.

39. B.E. Warren, X-Ray Diffraction, Dover Publications, New York, 1990.

40. P. Jenniskens, D.F. Blake, Structural transitions in amorphous water ice and astrophysical implications, Science, 1994, 265, 753–756.

41. P. Brüggeller, E. Mayer, Complete vitrification in pure liquid water and dilute aqueous solutions, Nature, 1980, 288, 569–571.

42. M.J. Dobro, L.A. Melanson, G.J. Jensen, A.W. McDowall, Methods in Enzymology Ch. 3, Elsevier, London, 2010.

43. J.A. McMillan, S.C. Los, Vitreous ice: irreversible transformations during warm-up, Nature, 1965, 206, 806–807.

44. G.P. Johari, A. Hallbrucker, E. Mayer, The glass–liquid transition of hyperquenched water, Nature, 1987, 330, 552–553.

45. S. Chen, A.M. Roseman, A.S. Hunter, S.P. Wood, S.G. Burston, N.A. Ranson, A.R. Clarke, H.R. Saibil, Location of a folding protein and shape changes in GroEL–GroES complexes imaged by cryo-electron microscopy, Nature, 1994, 371, 261–264.

46. R.M. Glaeser, K.A. Taylor, Radiation damage relative to transmission electron microscopy of biological specimens at low temperature: a review, J. Microsc., 1978, 112, 127–138.

47. R.M. Glaeser, Methods in Enzymology Ch. 2, Elsevier, London, 2016.

48. S. Uehara, H. Nikjoo, Monte Carlo Simulation of Water Radiolysis for Low-energy Charged Particles, J. Radiat. Res. (Tokyo), 2006, 47, 69–81.

49. R.J.D. Miller, O. Paré-Labrosse, A. Sarracini, J.E. Besaw, Three-dimensional view of ultrafast dynamics in photoexcited bacteriorhodopsin in the multiphoton regime and biological relevance, Nat. Commun., 2020, 11, 1240.

50. M. Gutman, Methods of Biochemical Analysis Ch. 1, John Wiley & Sons, Inc., New York, 1984.

Chapter 4: *Microsecond melting and revitrification of cryo samples*[2]

4.1 Introduction

Proteins enable living systems to process energy, self-regulate, respond to stimuli, grow, and reproduce. As nanoscale machines, they are inherently dynamic systems that undergo conformational rearrangements as they perform their tasks.[1–4] The characteristic timescales involved typically range from microseconds to milliseconds.[5,6] While cryo-electron microscopy (cryo-EM)[7–10] is rapidly becoming the preferred method in structural biology,[11] its time resolution is currently too low to observe such fast dynamics, leaving our understanding of protein function fundamentally incomplete.[6] In time-resolved cryo-EM, dynamics are usually induced by rapidly mixing two reactants or exposing the sample to a short stimulus, such as a pulse of light, after which the sample is rapidly plunge-frozen to trap the particles in short-lived states.[12–16] However, the time required for plunge-freezing limits the time resolution of this technique to several milliseconds,[16,17] too slow to observe many relevant processes.

We have recently demonstrated a novel approach to time-resolved cryo-EM with microsecond time resolution, three orders of magnitude faster than previously possible.[18,19] Our method involves melting a cryo sample with a laser beam for a duration of tens of microseconds or longer, which provides a tunable time window during which a stimulus can cause the particles to undergo conformational dynamics. When the heating laser is switched off, the sample revitrifies within just a few microseconds,[18] trapping the particles in their transient configurations, which can be subsequently imaged with the electron beam. A short laser pulse can serve as a suitable stimulus to induce dynamics, either by directly triggering a photoactive protein or by releasing a caged compound, such as ions, ATP, or peptides.[20,21] Some types of stimuli, such as the release of caged compounds, may already be applied before the sample is melted. Since the particles are unable to undergo conformational dynamics while they are trapped in the vitreous ice matrix, the stimulus only becomes active once the sample is melted.

---

[2] Reproduced with small adaptations from Jonathan M. Voss, Oliver F. Harder, Pavel K. Olshin, Marcel Drabbels, Ulrich J. Lorenz, Structural Dynamics 8, 054302 (2021).

Personal contribution to this chapter: I prepared the cryo-samples, and handled the cryo-equipment. With Jonathan Voss, I discovered the characteristic pattern of crystalline ice surrounding revitrified areas and collected the presented diffraction patterns, micrographs and cryo-EM data. Lastly, I supported the preparation of this manuscript.

4.2 Results

Figure 1 presents a demonstration of such a melting and revitrification experiment that makes use of the well-established phenomenon that particles incur electron beam damage during cryo imaging.[22,23] Vitreous ice is believed to fix fragments in place, thereby preserving the structure of the particles during imaging.[22,23] In contrast, melting the sample should allow fragments to diffuse apart. In our experiment, we study a cryo sample of apoferritin on a holey gold film[24] (Figure 1a).

The sample is irradiated with the electron beam, which induces fragmentation and thus acts as a stimulus for structural changes to occur (Figure 1b). Laser melting the sample (Figure 1c) should then allow the damaged particles to unravel in liquid (Figure 1d) and permit us to trap them in partially disassembled configurations when the heating laser is switched off and the sample rapidly revitrifies (Figure 1e). The experiment confirms this expectation. In the composite micrograph of Figure 1f, we have illuminated the sample only in the top left and bottom right with a dose of 5 and 10 electrons/Å^2, respectively, thus damaging only the proteins in these areas. We subsequently melt and revitrify the sample *in situ* with a 15 μs laser pulse[25] (532 nm, 63 mW, 24±1 μm spot size, see Supplementary Note S1 and Figure S1), after which we record the micrograph in Figure 1g.

The regions previously exposed to the electron beam (dashed circles) have visibly thinned, likely due to the evaporation of radiolysis products[23] that were liberated when the ice was melted. The particles in these areas have disassembled during the short time when the sample was liquid, leaving only fragments that offer little contrast. As evident in details of the areas marked with squares, disassembly is more extensive at higher electron dose (Figure 1i,j). In contrast, particles in the unexposed parts remain intact (Figure 1h).

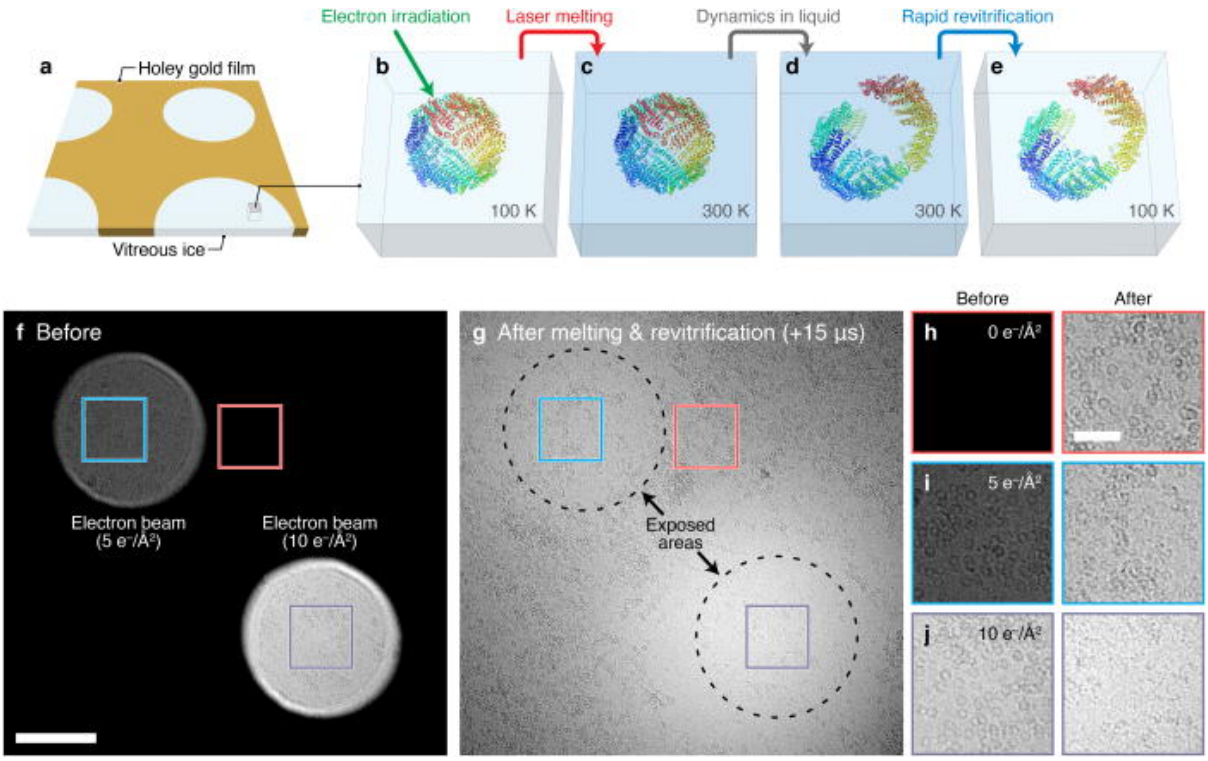

Figure 1. Rapid melting and revitrification of cryo samples, experimental concept and demonstration. (a) Illustration of the geometry of the cryo sample, which is supported by a holey gold film. (b–e) Experimental concept. (b) Apoferritin particles are irradiated with the electron beam, which alters their structure and thus serves as a stimulus for dynamics to occur. (c) The cryo sample is melted *in situ* by heating with a laser, (d) allowing the structure of the particles to freely evolve. (e) Once the laser is switched off, the sample rapidly revitrifies and particles are arrested in their transient configurations, which can be subsequently imaged with conventional cryo-EM techniques. Cartoon of apoferritin adapted from Ref. 24 (f–j) Proof-of-principle demonstration. (f) Composite micrograph of a cryo sample of apoferritin, in which only the two circular areas in the top left and bottom right have been exposed with a dose of 5 and 10 electrons/Å^2, respectively. Scale bar, 200 nm. (g) The sample is melted *in situ* with a 15 µs laser pulse and revitrifies. Particles that were illuminated with the electron beam prior to melting have unraveled during the short period when the sample was liquid, while those in the unexposed areas remain intact. (h–j) Details of the square areas marked in (f,g). Scale bar, 50 nm.

The success of melting and revitrification experiments crucially depends on the ability to accurately adjust the laser power, so that the sample reaches the desired temperature during the laser pulse. As shown in Figure 2, we calibrate the laser power *in situ* by heating a cryo sample with laser pulses of increasing power until it reaches the melting point of ice. The micrograph in Figure 2a shows a cryo sample on a holey gold film, where the hole that is visible is located in the center of a square of the gold mesh supporting the sample.

Figure 2b shows that irradiation with a 10 μs laser pulse of 14 mW power leaves the sample unchanged. Here and in the following experiments, the laser beam is centered onto the area under observation. In contrast, a 19 mW laser pulse induces devitrification (Figure 2c), as is observed when a cryo sample is warmed above a temperature of 150 K (Ref. 26). When we heat the sample with pulses of increasing power, the ice crystals can be seen to grow (Figure 2d–f). Finally, at a laser power of 46 mW, the sample melts and revitrifies (Figure 2g,n), allowing us to identify the power at which the sample reaches the melting point of ice.[18] To heat the sample to a specific temperature exceeding the melting point, the laser power can be adjusted by comparison with heat transfer simulations, as discussed below.

Figure 2h–m shows diffraction patterns of a second identical cryo sample, recorded after heating it with pulses of the same laser powers as above (see also Figure S2). The diffraction patterns confirm that the sample transforms from vitreous ice (Figure 2i) to a mixture of cubic and hexagonal ice (Figure 2j–m). Finally, Figure 2n displays a diffraction pattern of the revitrified sample in Figure 2g, in which diffraction spots originating from ice crystals are notably absent.

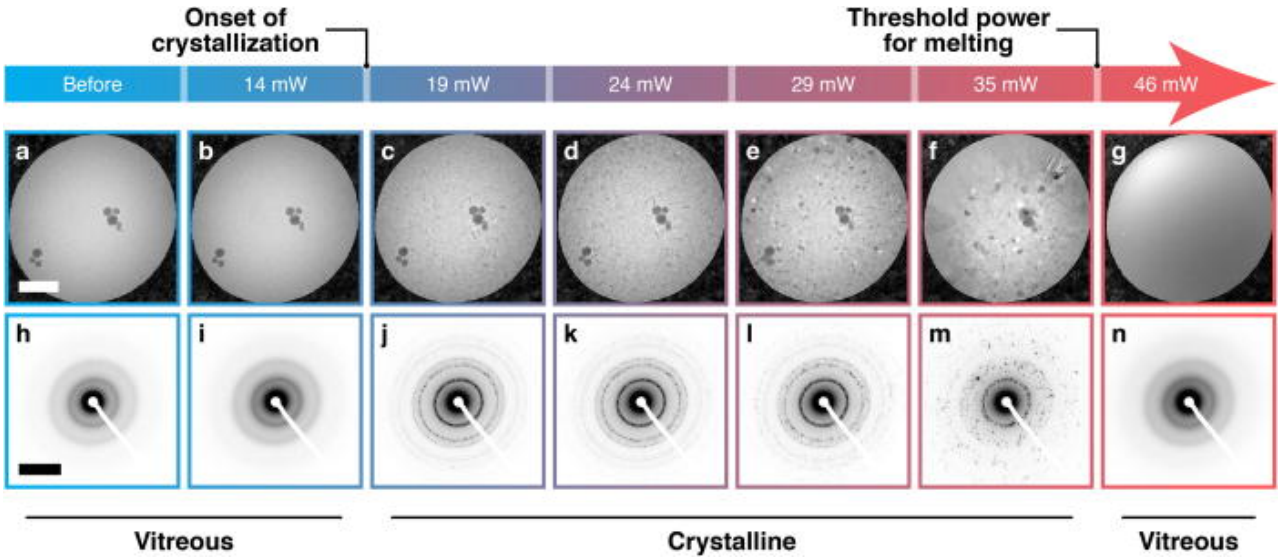

Figure 2. Phase behavior of cryo samples heated with laser pulses of increasing power. (a–g) Micrographs of a cryo sample under exposure to laser pulses of increasing power. (a) The sample (b) remains vitreous after heating with a 10 μs laser pulse of 14 mW power, but (c) crystallizes at a power of 19 mW. (d–f) The crystal morphology changes as the power is increased in steps to 35 mW. (g) A single pulse of 46 mW power melts the sample, causing it to revitrify when it cools after the end of the laser pulse. (h–m) Diffraction patterns of a second identical cryo sample under exposure to laser pulses of the same powers as in (a–f). (n) Diffraction pattern of the revitrified sample in (g). Scale bars, 500 nm and 5 nm^{-1}.

As illustrated in Figure 3, the phase behavior of the cryo sample under laser irradiation also provides a convenient means to verify *in situ* that the sample has reached the desired temperature in an individual melting and revitrification experiment as well as to make adjustments of the laser power on the fly. Figure 3a shows a low magnification micrograph of a cryo sample after irradiation with a 10 μs laser pulse (46 mW). As above, the laser beam has been centered onto the square of the gold mesh. The laser spot size is indicated with a green circle. In a time-resolved cryo-EM experiment, the laser power is typically adjusted to quickly heat the sample to room temperature. Here, we have instead chosen a laser power that will just barely heat the sample above the melting point in the center of the laser focus, as established with the procedure detailed in Figure 2. As discussed in the following, this choice facilitates the interpretation of our experiments. An enlarged view of the area marked with a square in Figure 3a reveals a spatial variation of the phase behavior of the sample (Figure 3b). As desired for a time-resolved cryo-EM experiment, the sample has melted and revitrified in the center of the laser focus (small solid circle).

In contrast, crystallization is apparent in the surrounding areas (large dashed circle), suggesting that further from the laser focus, where the sample has not been heated above the melting point, it has devitrified. At even larger distances closer to the grid bars, the sample has remained vitreous, having apparently not exceeded the crystallization temperature. The spatial variation of the phase behavior is also evident in micrographs (Figure 3c–h) and diffraction patterns (Figure 3i–n) of the areas marked with colored squares in Figure 3b. Near the center of the laser focus and close to the bars of the gold mesh, the homogeneous contrast of the micrographs (Figure 3c,h) and diffuse rings of the diffraction patterns (Figure 3i,n) confirm the presence of vitreous ice. In contrast, the areas in between exhibit crystals, which increase in size closer to the laser focus (Figure 3d–g) and whose diffraction patterns identify mixtures of cubic and hexagonal ice (Figure 3j–m).

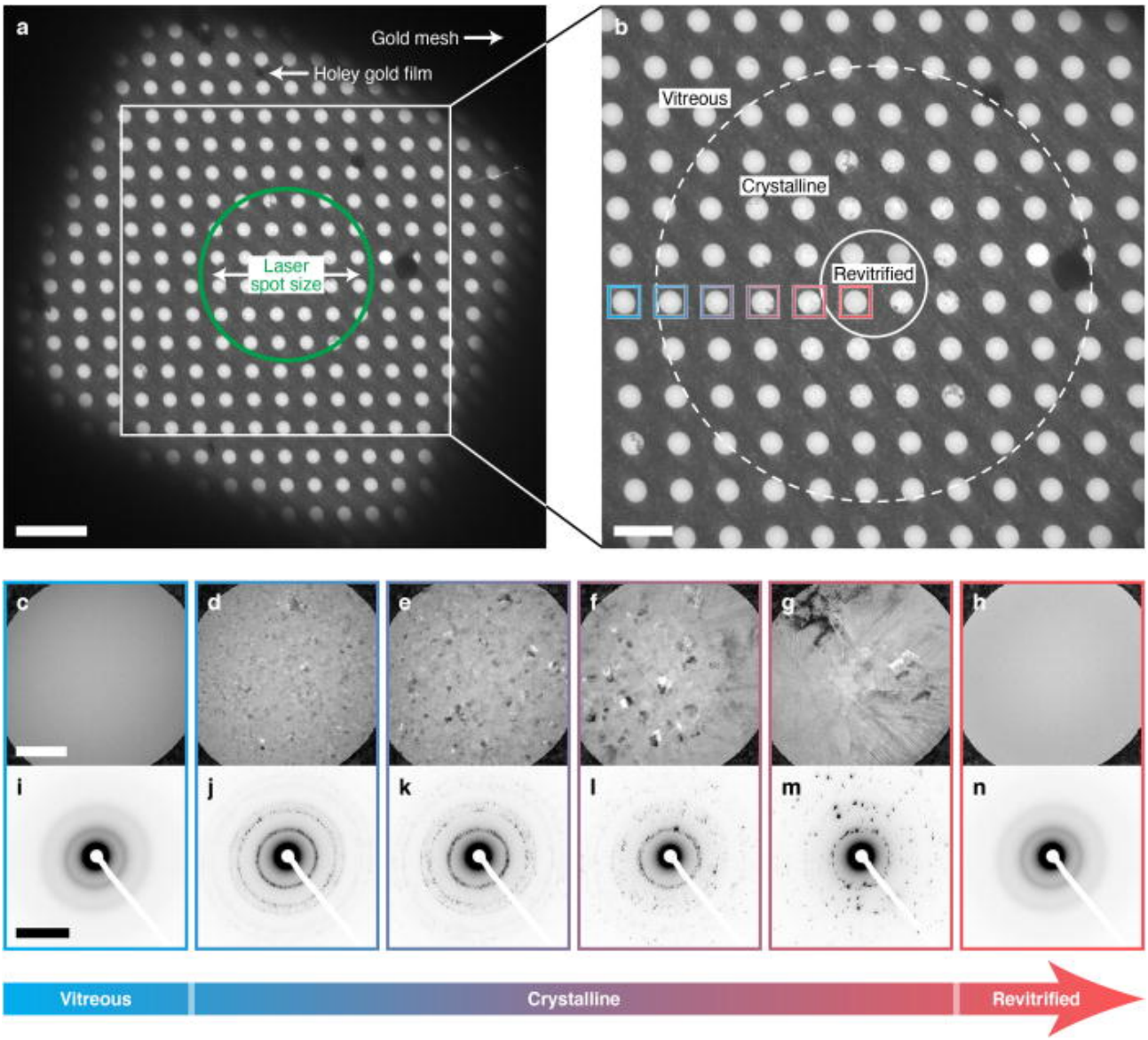

Figure 3. Phase behavior of a cryo sample in a melting and revitrification experiment. (a) Micrograph of a cryo sample after irradiation with a 10 μs laser pulse (46 mW). The green circle indicates the laser position and spot size (24 μm FWHM). Scale bar, 10 μm. (b) Enlarged view of the region marked with the white square in (a). Melting and revitrification has occurred in all but one of the holes in the area marked with the small solid circle, while the sample has crystallized within the bounds of the large dashed circle. The rest of the sample has remained vitreous. Scale bar, 5 μm. (c–h) Micrographs and (i–n) diffraction patterns of the regions marked with colored squares in (b). Scale bars, 500 nm and 5 nm^{-1}.

The phase behavior of the cryo sample as well as the crystal morphology in the devitrified areas can be understood when considering a time-temperature transformation diagram of supercooled water, as shown in Figure 4. Irradiation of the sample (~100 K) with a laser pulse rapidly heats the vitreous ice above its glass transition temperature (136 K), so that it melts into a supercooled liquid.[27] As the temperature rises further, the crystallization time of this metastable liquid decreases dramatically. The estimated crystallization time[28,29] (black curve, see also Note S2 and Figure S3) reaches a minimum of about 5 μs around 225 K. Due to the rapid crystallization between 150–235 K, this temperature range is frequently referred to as "no man's land," where the characterization of supercooled water has largely remained elusive.[30–34] Rapid crystallization in "no man's land" notably causes the formation of cubic ice in the cryo sample of Figure 2c when it is heated with a microsecond laser pulse of less than half the power needed to reach the melting point. We note that the crystallization times are estimated for pure water samples and therefore provide only a qualitative indication of the actual crystallization rates in our cryo samples. In the experiment of Figure 3, the laser power was adjusted such that the sample reaches the melting point only at the center of the laser focus. Correspondingly, we observe that only a small region of about 9 μm diameter revitrifies. Heat transfer simulations confirm that its size closely matches that of the area whose temperature exceeds the melting point by the end of the laser pulse, as discussed in more detail below. The crystallization of the surrounding areas likely does not occur while the sample cools, since the cooling rate of $>10^7$ K/s is much higher than is needed to outrun crystallization, as previously shown,[18] which allows the sample to revitrify in the center of the laser focus. Instead, it appears that crystallization already occurs during laser heating, as the sample traverses "no man's land." Only those areas that are subsequently heated above the melting point will then become liquid again and revitrify after the heating laser is switched off. The interpretation that crystal formation occurs during laser heating is also consistent with the spatial variation of the size of the crystallites that we observe in the crystalline regions (Figure 3d–g). Below 225 K, the crystallization process is characterized by fast nucleation, but slow crystal growth. The opposite holds above this temperature, where nucleation slows dramatically, and crystallization is dominated by fast crystal growth (Figure S3).[35] Sample areas closer to the laser focus heat up more rapidly and therefore spend less time at temperatures below 225 K, where nucleation rates are high. A smaller number of nuclei is thus formed that can subsequently grow to a larger size once the temperature exceeds 225 K, in agreement with our observations

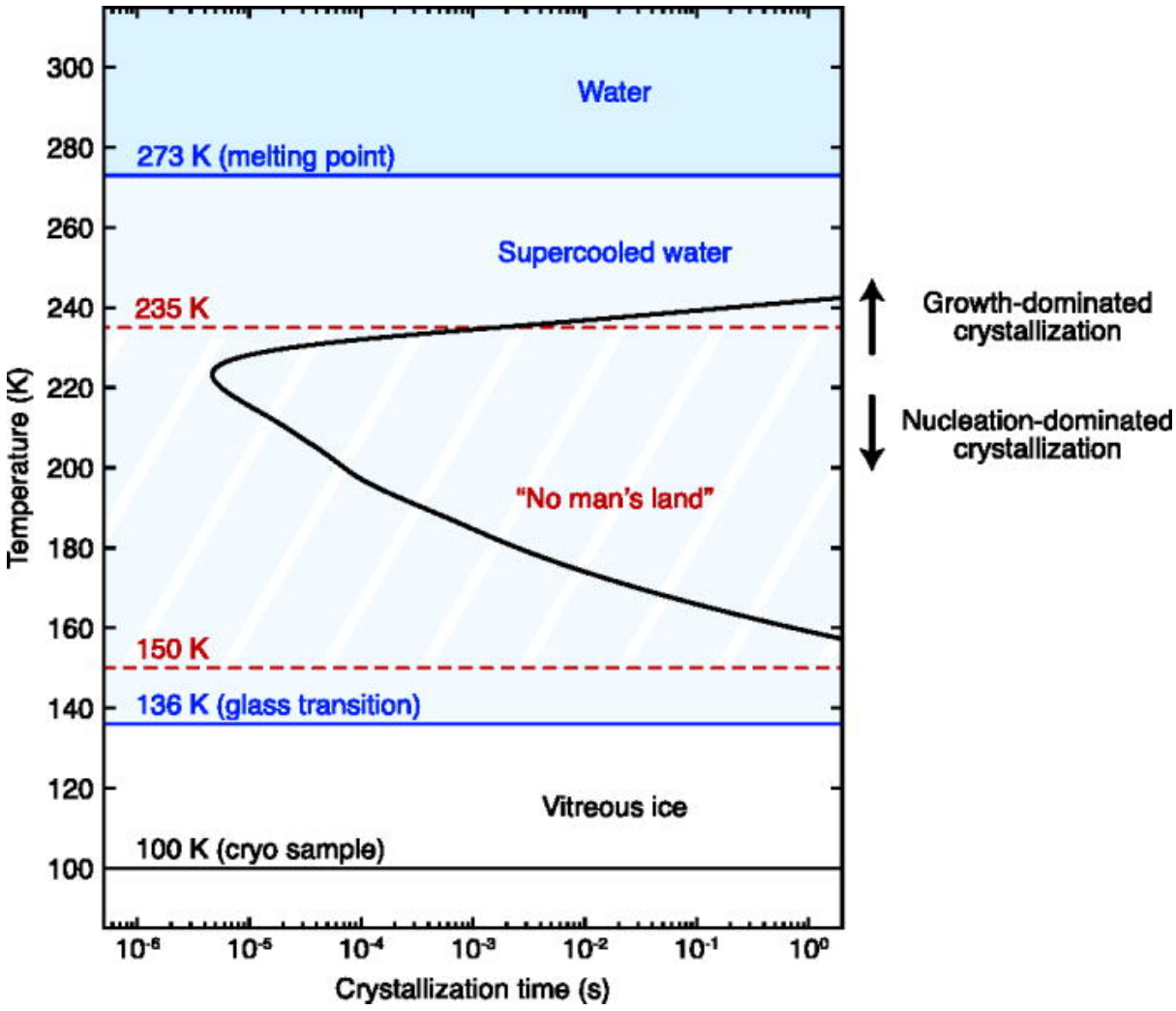

Figure 4. Time-temperature transformation diagram of supercooled water. The black curve indicates the crystallization time of supercooled water, which is estimated from experimental nucleation[43] and growth[44] rates (see Note S2). It exhibits a minimum of 5 μs at about 225 K, in a region of the phase diagram of water commonly referred to as "no man's land,"[30–34] where rapid crystallization hinders the characterization of supercooled water. Crystallization is dominated by rapid crystal growth above 225 K, while nucleation dominates at lower temperatures.[35] The solid blue lines indicate transition temperatures,[27] while the dashed red lines denote the boundaries of "no man's land."[26,45]

Simulations of the temperature evolution of the sample in the experiment of Figure 3 corroborate our interpretation of the observed phase behavior and provide further insight (Note S3 and Figure S4). In agreement with the experiment, the temperature in the holes closest to the laser focus barely exceeds the melting point at the end of the 10 μs laser pulse (46 mW, as in the experiment, see also Figure S5a). The corresponding temperature distribution of the cryo sample is depicted in Figure 5a, with the laser spot indicated by a green circle.

While the sample in the holes closest to the laser focus has reached a temperature of 273 K, regions close to the bars of the specimen grid have remained at the initial temperature of 100 K. The regular pattern of holes in the gold film support manifests itself in lower sample temperatures at the sites of the holes. As we discuss in Figure S5b, adding a layer of graphene to the sample removes these local temperature gradients. An enlarged view of the area marked with a white square is shown in Figure 5b, with the 273 K isotherm highlighted in white. Notably, the size of the area enclosed by the isotherm closely matches that of the revitrified area in our experiment, suggesting that the revitrified area corresponds to the region that melts during the laser pulse. The dashed circle in Figure 5b indicates the boundary of the crystalline region that we observe in the experiment. This boundary, for which the simulation predicts a temperature of about 170 K, is likely defined by the complex crystallization kinetics of the rapidly heated sample.

The temperature evolution of the sample and its phase behavior change in a characteristic fashion when the heating laser power is increased further. While the ice film in the holes closest to the laser focus (blue dot in Figure 5b) heats up more rapidly (Figure S5a), evaporative cooling limits the plateau temperature at which it stabilizes (blue curve in Figure 5c). Even at three times higher laser power, the temperature barely exceeds 300 K. This demonstrates that evaporative cooling can provide a negative feedback that stabilizes the plateau temperature for widely varying laser intensities, which facilitates control of the sample temperature. This negative feedback can be tuned by altering the sample geometry. For example, by reducing the hole size of the gold film from 2 μm to 1 μm, the sample temperature increases by about 25 K at the highest laser powers (yellow curve). Much higher temperatures can be reached by adding a graphene layer between the holey gold film and the vitreous ice (red curve).[36] This is desirable, for example, for the purpose of temperature jump experiments.

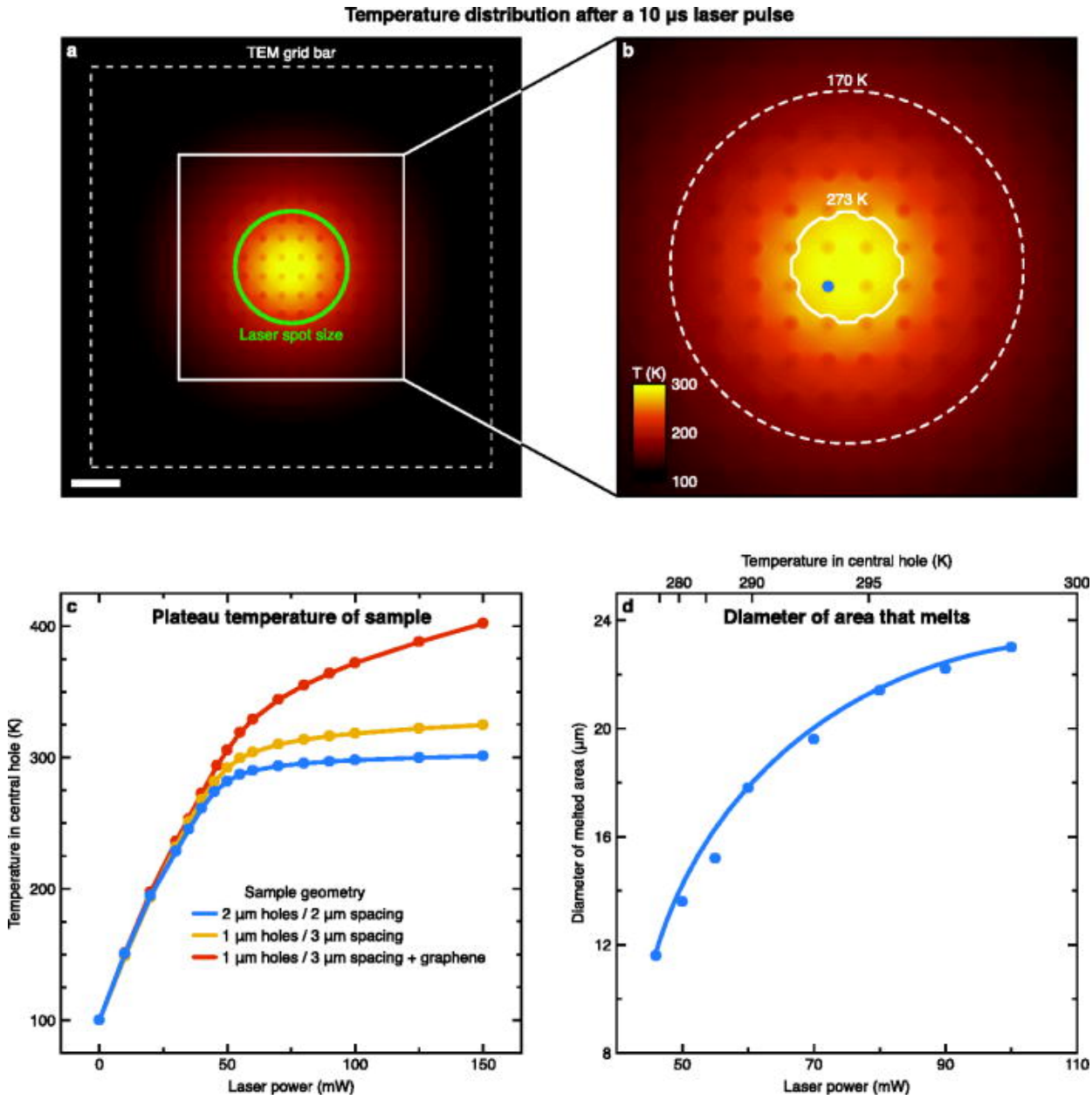

Figure 5. Heat transfer simulations of a melting and revitrification experiment. (a,b) Temperature distribution of a cryo sample after irradiation with a 10 µs laser pulse (46 mW, 24 µm spot size, indicated with a green circle). Scale bar, 10 µm. The white line in (b) indicates the isotherm at 273 K and the dashed circle represents the boundary of the crystalline region from the experiment in Figure 3b, at which the simulation predicts a temperature of 170 K. (c) Plateau temperature of the sample (at the position of the blue dot in (b)) as a function of laser power for different sample geometries. (d) Diameter of area that melts as a function of the laser power (probed at the position of the blue dot in (b)). The curve serves as a guide for the eye.

With increasing laser power, the diameter of the area that is melted and revitrified increases, as shown in Figure 5d. The temperature reached in the holes closest to the laser focus increases from 273 K to 298 K as the laser power is doubled. At the same time, the diameter of the revitrified area increases from 12 μm to 22 μm. This is borne out experimentally in Figure 6, which shows identical cryo samples after irradiation with 15 μs laser pulses of increasing power. Here, the revitrified holes are highlighted in red. As the laser power is increased from 63 mW to 79 mW, the diameter of the revitrified area increases from 10 μm to 22 μm.

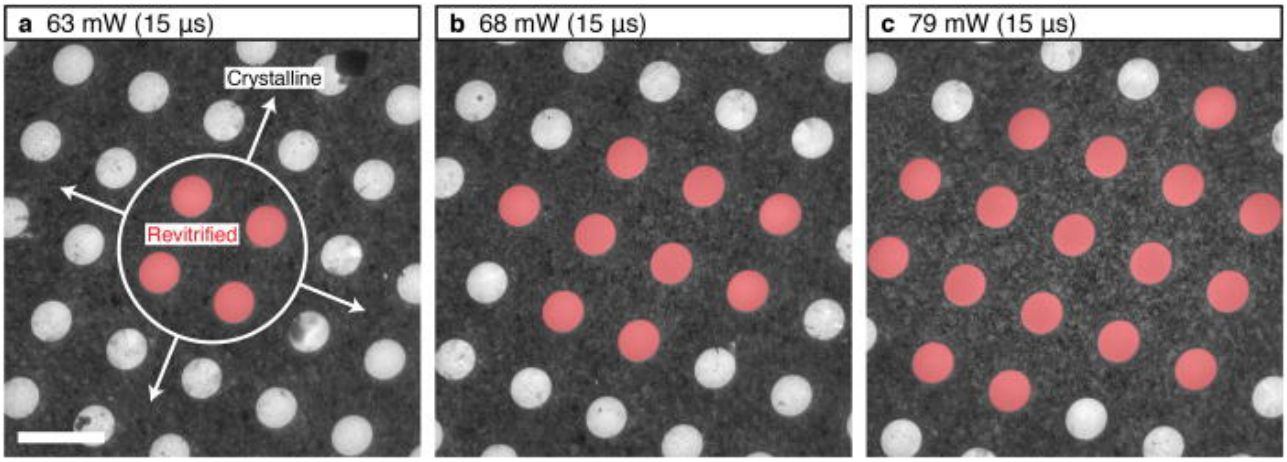

Figure 6. The size of the revitrified area increases with laser power. (a–c) Micrographs of cryo samples irradiated by a 15 μs laser pulse of increasing power. Areas that melted and revitrified are highlighted in red. Scale bar, 4 μm.

4.3 Discussion and Outlook

Our experiments show that the phase behavior of the cryo sample provides a convenient means to infer details of its temperature evolution during a rapid melting and revitrification experiment. The laser power required for such an experiment can be calibrated *in situ* by determining the power needed to melt a devitrified area. By comparison with simulations, the power can then be increased, so as to heat the sample to a desired temperature above the melting point of ice. The success of an experiment can be immediately verified by the presence of a revitrified area surrounded by a crystalline region, in which the sample has not melted.

The diameter of the revitrified area is characteristic of the temperature distribution of the sample at the end of the laser pulse, which can be compared with simulations to reconstruct the entire temperature evolution of the sample. The diameter of the revitrified area can also be used to quickly assess *in situ* whether experiments on different areas of the grid have been carried out under identical conditions, allowing one to adjust the laser power on the fly if required. Our heat transfer simulations demonstrate that evaporative cooling provides a negative feedback that stabilizes the plateau temperature that the sample reaches. Small changes in the power or alignment of the laser, as well as slight variations of the heat transfer properties between different areas, will therefore only lead to minor errors in the temperature.

By changing the sample geometry, evaporative cooling can be tuned either to limit the maximum temperature of the sample or enable temperature jump experiments. Intriguingly, our experiments suggest that crystallization occurs during laser heating as the sample traverses "no man's land." Time-resolved experiments with microsecond electron pulses[37] should allow us to verify this assumption by observing the phase behavior of water in real time.[38–41] Such experiments also offer the opportunity to study the crystallization kinetics of supercooled water, which is a rich topic in its own right.[31–34] We note that the transient formation of cubic ice during the laser melting process does not pose a problem for preserving the structure of the embedded proteins. In fact, it has recently been shown that high-resolution structures of particles can be obtained in devitrified samples.[42]

4.4 References

1. J. Frank, Conformational Proteomics of Macromolecular Architecture: Approaching the Structure of Large Molecular Assemblies and Their Mechanisms of Action Ch. 13, World Scientific, Singapore, 2004.

2. J. Frank, Three-Dimensional Electron Microscopy of Macromolecular Assemblies: Visualization of Biological Molecules in Their Native State, Oxford University Press, New York, 2006.

3. E. Cao, M. Liao, Y. Cheng and D. Julius, TRPV1 structures in distinct conformations reveal activation mechanisms, Nature, 2013, 504, 113–118.

4. J. Zhao, S. Benlekbir and J. L. Rubinstein, Electron cryomicroscopy observation of rotational states in a eukaryotic V-ATPase, Nature, 2015, 521, 241–245.

5. D. D. Boehr, H. J. Dyson and P. E. Wright, An NMR perspective on enzyme dynamics, Chem. Rev., 2006, 106, 3055–3079.

6. K. Henzler-Wildman, D. Kern, Dynamic personalities of proteins, Nature, 2007, 450, 964-972.

7. M. Adrian, J. Dubochet, J. Lepault and A. W. McDowall, Cryo-electron microscopy of viruses, Nature, 1984, 308, 32–36.

8. J. Dubochet, M. Adrian, J.-J. Chang, J.-C. Homo, J. Lepault, A. W. McDowall and P. Schultz, Cryo-electron microscopy of vitrified specimens, Q. Rev. Biophys., 1988, 21, 129–228.
9. Y. Cheng, Single-Particle Cryo-EM at Crystallographic Resolution, Cell, 2015, 161, 450–457.

10. T. Nakane, A. Kotecha, A. Sente, G. McMullan, S. Masiulis, P. M. G. E. Brown, I. T. Grigoras, L. Malinauskaite, T. Malinauskas, J. Miehling, T. Uchański, L. Yu, D. Karia, E. V. Pechnikova, E. de Jong, J. Keizer, M. Bischoff, J. McCormack, P. Tiemeijer, S. W. Hardwick, D. Y. Chirgadze, G. Murshudov, A. R. Aricescu and S. H. W. Scheres, Single-particle cryo-EM at atomic resolution, Nature, 2020, 587, 152–156.

11. E. Hand, Cheap Shots, Science, 2020, 367, 354–358.

12. B. Chen and J. Frank, Two promising future developments of cryo-EM: capturing short-lived states and mapping a continuum of states of a macromolecule, Microscopy, 2016, 65, 69–79.

13. Z. Lu, T. R. Shaikh, D. Barnard, X. Meng, H. Mohamed, A. Yassin, C. A. Mannella, R. K. Agrawal, T.-M. Lu and T. Wagenknecht, Monolithic microfluidic mixing–spraying devices for time-resolved cryo-electron microscopy, J. Struct. Biol., 2009, 168, 388–395.

14. T. R. Shaikh, A. S. Yassin, Z. Lu, D. Barnard, X. Meng, T.-M. Lu, T. Wagenknecht and R. K. Agrawal, Initial bridges between two ribosomal subunits are formed within 9.4 milliseconds, as studied by time-resolved cryo-EM, Proc. Natl. Acad. Sci., 2014, 111, 9822–9827.

15. J. F. Menetret, W. Hofmann, R. R. Schroder, G. Rapp and R. S. Goody, Time-resolved cryo-electron microscopic study of the dissociation of actomyosin induced by photolysis of photolabile nucleotides, J. Mol. Biol., 1991, 219, 139–144.

16. T. R. Shaikh, D. Barnard, X. Meng and T. Wagenknecht, Implementation of a flash-photolysis system for time-resolved cryo-electron microscopy, J. Struct. Biol., 2009, 165, 184–189.

17. J. Frank, Time-resolved cryo-electron microscopy: Recent progress, J. Struct. Biol., 2017, 200, 303–306.

18. J. M. Voss, O. F. Harder, P. K. Olshin, M. Drabbels and U. J. Lorenz, Rapid melting and revitrification as an approach to microsecond time-resolved cryo-electron microscopy, Chem. Phys. Lett., 2021, 778, 138812.

19. M. J. Dobro, L. A. Melanson, G. J. Jensen and A. W. McDowall, Methods in Enzymology Ch. 3, Elsevier, London, 2010.

20. G. C. R. Ellis-Davies, Caged compounds: photorelease technology for control of cellular chemistry and physiology, Nat. Methods, 2007, 4, 619–628.

21. Y. Shigeri, Y. Tatsu and N. Yumoto, Synthesis and application of caged peptides and proteins, Pharmacol. Ther., 2001, 91, 85–92.

22. R. M. Glaeser and K. A. Taylor, Radiation damage relative to transmission electron microscopy of biological specimens at low temperature: a review, J. Microsc., 1978, 112, 127–138.

23. R. M. Glaeser, Methods in Enzymology Ch. 2, Elsevier, London, 2016.

24. C. J. Russo and L. A. Passmore, Ultrastable gold substrates for electron cryomicroscopy, Science, 2014, 346, 1377–1380.

25. P. K. Olshin, M. Drabbels and U. J. Lorenz, Characterization of a time-resolved electron microscope with a Schottky field emission gun, Struct. Dyn., 2020, 7, 054304.

26. G. P. Johari, A. Hallbrucker and E. Mayer, The glass–liquid transition of hyperquenched water, Nature, 1987, 330, 552–553.

27. K. Amann-Winkel, C. Gainaru, P. H. Handle, M. Seidl, H. Nelson, R. Bohmer and T. Loerting, Water's second glass transition, Proc. Natl. Acad. Sci., 2013, 110, 17720–17725.

28. P. G. Debenedetti, Metastable Liquids: Concepts and Principles, Princeton University Press, Princeton, 1997.

29. H. Tanaka, Possible resolution of the Kauzmann paradox in supercooled liquids, Phys. Rev. E, 2003, 68, 011505.

30. O. Mishima and H. E. Stanley, The relationship between liquid, supercooled and glassy water, Nature, 1998, 396, 329–335.

31. P. G. Debenedetti, Supercooled and glassy water, J Phys Condens Matter, 2003, 15, R1669–R1726.

32. J. A. Sellberg, C. Huang, T. A. McQueen, N. D. Loh, H. Laksmono, D. Schlesinger, R. G. Sierra, D. Nordlund, C. Y. Hampton, D. Starodub, D. P. DePonte, M. Beye, C. Chen, A. V. Martin, A. Barty, K. T. Wikfeldt, T. M. Weiss, C. Caronna, J. Feldkamp, L. B. Skinner, M. M. Seibert, M. Messerschmidt, G. J. Williams, S. Boutet, L. G. M. Pettersson, M. J. Bogan and A. Nilsson, Ultrafast x-ray probing of water structure below the homogeneous ice nucleation temperature, Nature, 2014, 510, 381–384.

33. P. Gallo, K. Amann-Winkel, C. A. Angell, M. A. Anisimov, F. Caupin, C. Chakravarty, E. Lascaris, T. Loerting, A. Z. Panagiotopoulos, J. Russo, J. A. Sellberg, H. E. Stanley, H. Tanaka, C. Vega, L. Xu and L. G. M. Pettersson, Water: A Tale of Two Liquids, Chem. Rev., 2016, 116, 7463–7500.

34. L. Kringle, W. A. Thornley, B. D. Kay and G. A. Kimmel, Reversible structural transformations in supercooled liquid water from 135 to 245 K, Science, 2020, 369, 1490–1492.

35. E. B. Moore and V. Molinero, Structural transformation in supercooled water controls the crystallization rate of ice, Nature, 2011, 479, 506–508.

36. C. J. Russo and L. A. Passmore, Controlling protein adsorption on graphene for cryo-EM using low-energy hydrogen plasmas, Nat. Methods, 2014, 11, 649–652.

37. P. K. Olshin, G. Bongiovanni, M. Drabbels and U. J. Lorenz, Atomic-Resolution Imaging of Fast Nanoscale Dynamics with Bright Microsecond Electron Pulses, Nano Lett., 2021, 21, 612–618.

38. B. J. Siwick, J. R. Dwyer, R. E. Jordan and R. J. D. Miller, An Atomic-Level View of Melting Using Femtosecond Electron Diffraction, Science, 2003, 302, 1382–1385.

39. J. S. Kim, T. LaGrange, B. W. Reed, M. L. Taheri, M. R. Armstrong, W. E. King, N. D. Browning and G. H. Campbell, Imaging of Transient Structures Using Nanosecond in Situ TEM, Science, 2008, 321, 1472–1475.

40. M. Z. Mo, Z. Chen, R. K. Li, M. Dunning, B. B. L. Witte, J. K. Baldwin, L. B. Fletcher, J. B. Kim, A. Ng, R. Redmer, A. H. Reid, P. Shekhar, X. Z. Shen, M. Shen, K. Sokolowski-Tinten, Y. Y. Tsui, Y. Q. Wang, Q. Zheng, X. J. Wang and S. H. Glenzer, Heterogeneous to homogeneous melting transition visualized with ultrafast electron diffraction, Science, 2018, 360, 1451–1455.

41. J. Yang, R. Dettori, J. P. F. Nunes, N. H. List, E. Biasin, M. Centurion, Z. Chen, A. A. Cordones, D. P. Deponte, T. F. Heinz, M. E. Kozina, K. Ledbetter, M.-F. Lin, A. M. Lindenberg, M. Mo, A. Nilsson, X. Shen, T. J. A. Wolf, D. Donadio, K. J. Gaffney, T. J. Martinez and X. Wang, Direct observation of ultrafast hydrogen bond strengthening in liquid water, Nature, 2021, 596, 531–535.

42. J.-P. Wieferig, D. J. Mills and W. Kühlbrandt, Devitrification reduces beam-induced movement in cryo-EM, IUCrJ, 2021, 8, 186–194.

43. A. J. Amaya and B. E. Wyslouzil, Ice nucleation rates near ~225 K, J Chem Phys, 2018, 148, 084501.

44. Y. Xu, N. G. Petrik, R. S. Smith, B. D. Kay and G. A. Kimmel, Growth rate of crystalline ice and the diffusivity of supercooled water from 126 to 262 K, Proc. Natl. Acad. Sci., 2016, 113, 14921–14925.

45. H. Kanno, R. J. Speedy and C. A. Angell, Supercooling of Water to -92 C Under Pressure, Science, 1975, 189, 880–881.

Chapter 5: *Microsecond melting and revitrification of cryo samples: protein structure and beam-induced motion*[3]

5.1 Introduction

Cryo-electron microscopy has been undergoing a stunning development in recent years, fueled by the introduction of a number of crucial innovations. Improved sample preparation methods [1 2 3 4], ever more powerful electron microscopes [5 6], faster and more sensitive electron detectors [7], and more sophisticated computational tools [8 9] have recently made it possible to obtain reconstructions of proteins at atomic resolution.[5 6] At its current rate of growth, cryo-EM is predicted to rival x-ray crystallography as the most popular method in structural biology in just a few years.[10 11] Another exciting frontier in cryo-EM is the study of dynamics, which can reveal insights into the function of a protein beyond the information that is available from a static structure.[12 13 14] Conformational sorting with advanced computation tools can be used to map out the free energy surface that a protein explores under equilibrium conditions in great detail.[15 16 17]

However, short-lived intermediates or transient states as well as fast out-of-equilibrium processes are more difficult to access. Time-resolved cryo-EM enables the study of such processes in principle, where dynamics are typically initiated with a light pulse [18 19] or through rapid mixing.[20 21 22] The sample is plunge frozen as the dynamics occur, trapping intermediates that can be subsequently imaged.[13 14 22 23]However, the time resolution of this approach is several milliseconds and is fundamentally limited by the timescale of plunge freezing, about 1 ms.[14 19] It is therefore too slow to capture many relevant processes, in particular the domain motions of proteins that are typically associated with their activity and that frequently occur on the microsecond to millisecond timescale.[24 25]

[3] Reproduced with small adaptations from Oliver F. Harder, Jonathan M. Voss, Pavel K. Olshin, Marcel Drabbels, Ulrich J. Lorenz, Acta Crystallogr D Struct Biol 78, (2022).

Personal contribution to this chapter: I prepared the cryo-samples, handled the cryo-equipment, finetuned the microscope alignment for high resolution data collection and discovered the need for magnification distortion correction. I conducted the experimental demonstration, collected the cryo-EM data and carried out preliminary data treatment, reconstructions in CryoSPARC, to verify structural conservation upon revitrification. Lastly, I supported the preparation of this manuscript.

We have recently established a novel approach to time-resolved cryo-EM that affords microsecond time resolution.[26 27] We illuminate a cryo sample with a focused laser beam to locally melt it and thus allow particle dynamics to briefly occur in liquid. After tens of microseconds, the heating laser is turned off and the sample rapidly cools and revitrifies, arresting the particles in their transient configurations, in which they can be subsequently imaged. Importantly, the time resolution of our approach is determined by the timescale of vitrification, which occurs within just a few microseconds.[27] Our method thus affords a time resolution that is three orders of magnitude higher than in conventional time-resolved experiments [14 19], which makes it possible to study a wide range of fast dynamics that have previously remained inaccessible.

Here, we add crucial details to the characterization of our method. While we have previously shown that the melting and revitrification process leaves the proteins intact [26 27], we here corroborate this finding by demonstrating that reconstructions obtained from conventional and revitrified cryo samples are indistinguishable within the spatial resolution of our instrument. Moreover, we analyze how the revitrification process alters the properties of the ice, showing that revitrified samples exhibit similar amounts of beam-induced motion as conventional samples, albeit with small differences in the drift behavior.

5.2 Methods

Cryo samples were prepared on UltrAuFoil R1.2/1.3 300 mesh grids (Quantifoil). The grids were rendered hydrophilic through 10 minutes of plasma cleaning in an ELMO glow discharge system operating with negative polarity, 0.8 mA plasma current, and 0.2 mbar residual air pressure. Approximately 3–3.5 μl of sample solution were applied to the foil side of the grids – either 1.70 mg/ml mouse heavy chain apoferritin in 20 mM HEPES buffer with 300 mM sodium chloride at pH 7.5 (Figure 1), 0.33 mg/ml mouse heavy chain apoferritin in 20 mM Tris buffer with 150 mM sodium chloride at pH 7.4 (Figure 2,3), or 11.5 mg/ml CCMV in 0.1 M sodium acetate buffer with 1 mM Na2EDTA and 1 mM NaN3 at pH 5.0 (Figure 2,3). The samples were plunge frozen with a Vitrobot MarkIV (Thermo Fisher Scientific) that was operated at 100 % relative humidity and a temperature of 22 °C, using a blotting time of 3–4 s. For imaging, the apoferritin and CCMV grids were loaded into either a Gatan 626 or a Gatan Elsa single tilt cryo-transfer specimen holder, respectively.

Experiments were performed with a JEOL 2200FS transmission electron microscope that we have modified for time-resolved experiments, as previously described.[28] The microscope is operated at 200 kV accelerating voltage and is equipped with an in-column Omega-type energy filter and a K3 direct electron detector (Gatan). Microsecond laser pulses for in situ melting and revitrification of the sample are obtained by chopping the output of a continuous laser (532 nm) with an acousto-optic modulator. The laser is reflected off a mirror located above the upper pole piece of the objective lens and strikes the sample at close to normal incidence. The laser beam is focused to a spot size of 24±1 μm FWHM, as measured by a knife-edge scan in the sample plane.

Micrographs were zero-loss filtered with a 10 eV slit width. The electron detector was operated in counting mode to acquire 30-frame movies with a total dose of 60 electrons/Å^2 and 2 and 3 s exposure times for apoferritin and CCMV, respectively. Micrographs were recorded with a pixel size of 0.9750 Å and 0.8514 Å for apoferritin and CCMV, respectively. Defocus values were in the range of 0.5–2.5 μm.

All images were corrected for the magnification distortion [29], which we determined from micrographs of a gold calibration standard (Ted Pella, product #673) with the mag_distortion_estimate_1.0.1 script.[29]

Single-particle reconstructions (see Fig. S1 for workflows) were carried out with cryoSPARC version 3.2.0.[8] The conventional apoferritin dataset consisted of 167 images. After patch motion correction and patch CTF estimation, 109 micrographs with CTF fits below 6.5 Å were selected. Following blob picking and inspection, particles were sorted into 30 classes, and 5 were used as templates to pick 146,763 particles from the micrographs. Of the picked particles, 81,332 were selected and sorted into 50 classes with a 160 Å circular mask. After removal of junk, 76,144 particles from 38 classes were selected and subjected to another round of 2D classification (50 classes, 140 Å mask). From this round of sorting, 55,183 particles across a total of 13 classes were selected. After ab initio reconstruction (O symmetry) and heterogeneous refinement (O symmetry) into 2 classes, the high-resolution class (49,885 particles) was homogeneously refined using O symmetry, resulting in a 4.57 Å map.

The revitrified apoferritin dataset was comprised of 100 micrographs taken from 6 melted and revitrified areas on 1 grid. After patch motion correction and patch CTF estimation, 70 images with CTF fits under 5.5 Å were chosen. Following blob picking and inspection, particles were sorted into 30 classes, and 27 were used as templates to pick 93,800 particles from the micrographs. Next, 58,792 particles were selected and sorted into 50 classes with a 160 Å circular mask. After removal of junk, 53,783 particles from 33 classes were chosen and again subjected to another round of 2D classification (50 classes, 140 Å mask). A total of 40 classes, corresponding to 49,476 particles, were selected. After ab initio reconstruction (O symmetry) and heterogeneous refinement (O symmetry) into 2 classes, the high-resolution class (45,953 particles) was homogenously refined using O symmetry, resulting in a 4.25 Å map.

The conventional CCMV dataset consisted of 269 images. After patch motion correction and patch CTF estimation, 97 micrographs with CTF fits below 6.0 Å were selected. Following blob picking and inspection, particles were sorted into 30 classes, and 27 were used as templates to pick 36,783 particles from the micrographs. Of the picked particles, 6,616 were selected and sorted into 50 classes with a 320 Å circular mask. After removal of junk, 6,554 particles from 21 classes were selected. After ab initio reconstruction (I symmetry) and heterogeneous refinement (I symmetry) into 2 classes, the high-resolution class (3,560 particles) was homogeneously refined using I symmetry, resulting in a 4.98 Å resolution map.

The revitrified CCMV dataset consisted of 391 images taken from 22 melted and revitrified areas on 7 grids. After patch motion correction and patch CTF estimation, 120 images with CTF fits below 6.5 Å were chosen. After blob picking and inspection, particles were sorted into 30 classes, and 10 were used as templates to pick 42,201 particles from the micrographs. Of the picked particles, 7,866 particles were selected and sorted into 50 classes with a 320 Å circular mask. After removal of junk, 7,240 particles from 16 classes were selected. After ab initio reconstruction (C1 symmetry) and heterogeneous refinement (I symmetry) into 2 classes, the high-resolution class (5,029 particles) was homogeneously refined using I symmetry, resulting in a 5.20 Å resolution map.

Single-particle reconstructions were visualized with ChimeraX.[30] The volumes of apoferritin in Figure 2 are displayed with contour levels of 0.20 and 0.15 for the conventional and revitrified samples, respectively. The molecular model from PDB 6V21 [31] was placed into the density through rigid body fitting. The details in Figure 2 show the density within 3.3 Å of residues 13–42 of chain C. The volumes for CCMV are displayed with contour levels of 0.100 and 0.115, for the conventional and revitrified samples, respectively. The molecular model from PDB 1CWP [32] was placed into the density through rigid body fitting. Details are shown for the density within 3.3 Å of residues 76–86 and 142–153 of chains A, B, and C.

Drift trajectories of apoferritin and CCMV were determined with local motion correction in cryoSPARC. The average displacement of the particles as a function of dose (Figure 3) was calculated using only the particles that were included in the reconstructions in Figure 2. We note that if we include all particles, the result is qualitatively the same.

5.3 Results and Discussion

Figure 1a,b illustrates the sample geometry and experimental approach. Cryo samples are prepared on UltrAuFoil R1.2/1.3 300 mesh gold grids [1], and the melting laser (532 nm, 24±1 μm spot size in the sample plane) is centered on a grid square (Figure 1a). Under illumination with a 20 μs laser pulse, the sample rapidly melts in the vicinity of the laser focus and subsequently revitrifies, arresting the motions of the embedded particles (Figure 1b).

Figure 1c–f displays micrographs of a typical experiment with a cryo sample of mouse apoferritin. Figure 1d shows a low magnification view of the grid square before laser irradiation, and Figure 1c a micrograph collected from the hole marked with a grey arrow. The sample is then illuminated *in situ* with a 20 μs laser pulse (205 mW), with the laser beam aligned to the central hole, which is marked with a crosshair. As indicated in Figure 1e, a circular area around the center of the laser focus has melted and revitrified (dashed semicircle).

In contrast, the adjacent regions, in which the temperature has remained below the melting point of water, have crystallized.[26] We then collect micrographs from holes within the revitrified area, such as that of Figure 1f, which reveals intact apoferritin particles. We note that in order to ensure a comparable temperature evolution in all melting and revitrification experiments, the laser power (typically about 165 mW) was always adjusted to obtain a revitrified region of similar size to that in Figure 1e. [26] We note that while aligning the laser, the sample is exposed to a dose of about 10^{-3} electrons/Å^2 before it is melted and revitrified. This dose is too low to induced any detectable amount of beam damage.

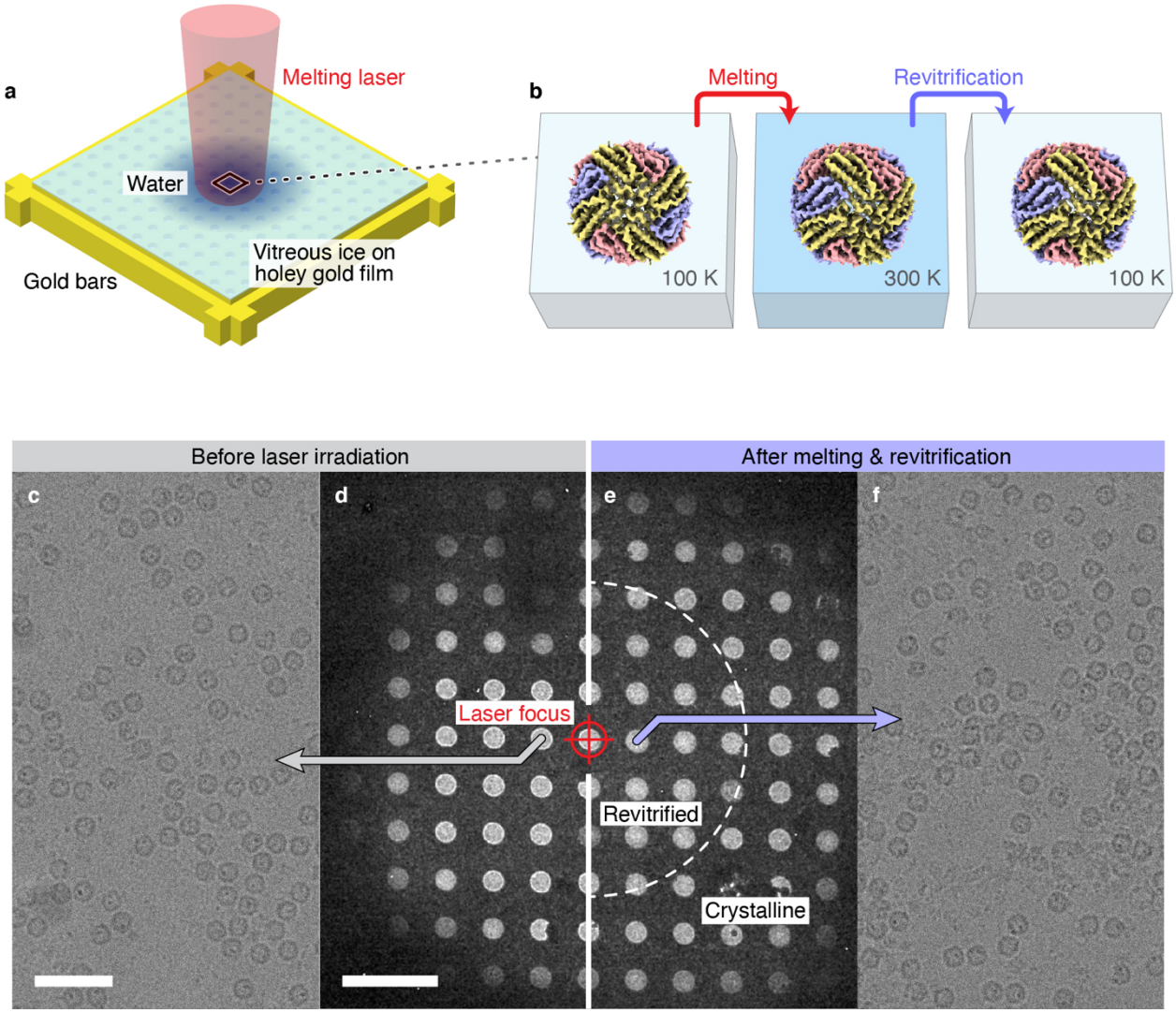

Figure 1. Rapid melting and revitrification of cryo samples, concept and experimental demonstration. (a) Illustration of the geometry of the cryo sample, which is prepared on a holey gold film supported by a gold mesh. The sample is irradiated *in situ* with a laser beam that is centered onto a grid square. (b) In the vicinity of the laser focus, the sample rapidly melts, allowing embedded particles to undergo equilibrium dynamics in the liquid phase. When the laser is switched off, the sample rapidly revitrifies, trapping the particles, so that they can be subsequently imaged. (c–f) Micrographs of a cryo sample of apoferritin (c,d) and of the same sample after melting and revitrification with a 20 μs laser pulse (e,f). The laser focus is aligned to the central hole, which is marked with a crosshair. The outline of the revitrified area is indicated in (e) with a dashed semicircle. Adjacent regions have crystallized. Scale bars, 50 nm in (c) and 5 μm in (d).

Single-particle reconstructions confirm that the melting and revitrification process preserves the structure of apoferritin.[31] Figure 2a compares the density map obtained from a conventional cryo sample (left, 4.57 Å resolution) with that obtained after melting and revitrification (right, 4.25 Å resolution). We note that the resolution is consistent with that previously obtained on a similar instrument.[33] Individual helices are clearly resolved in both reconstructions. As evident in the details shown on the left and right, some side chain density is visible, which is slightly more pronounced in the higher resolution map obtained from the revitrified samples.

Within the resolution afforded by our instrument, the structures are indistinguishable. This result is confirmed by a second set of experiments on cryo samples of CCMV, an icosahedral plant virus [32,34] (Figure 2b). We obtain near-identical reconstructions of CCMV with a resolution of 4.98 Å and 5.20 Å for the conventional (left) and the revitrified cryo samples (right), respectively. Secondary structural elements of the viral capsid are well resolved, which is also evident in the details of the density in the vicinity of the quasi three-fold symmetry axis. We note that the viral RNA inside the capsid is disordered and therefore not resolved. We conclude that the melting and revitrification process leaves the particles intact and that within the spatial resolution of our experiment, it does not alter their structure.

Evidently, rapid melting and revitrification does not expose the particles to any mechanical forces or other processes that damage their structure. This conclusion is supported by a consideration of the different elements of the experiment, including the nature of the interaction between the laser beam and the particles, the melting and revitrification steps, as well as the interactions that the particles encounter while the sample is liquid.

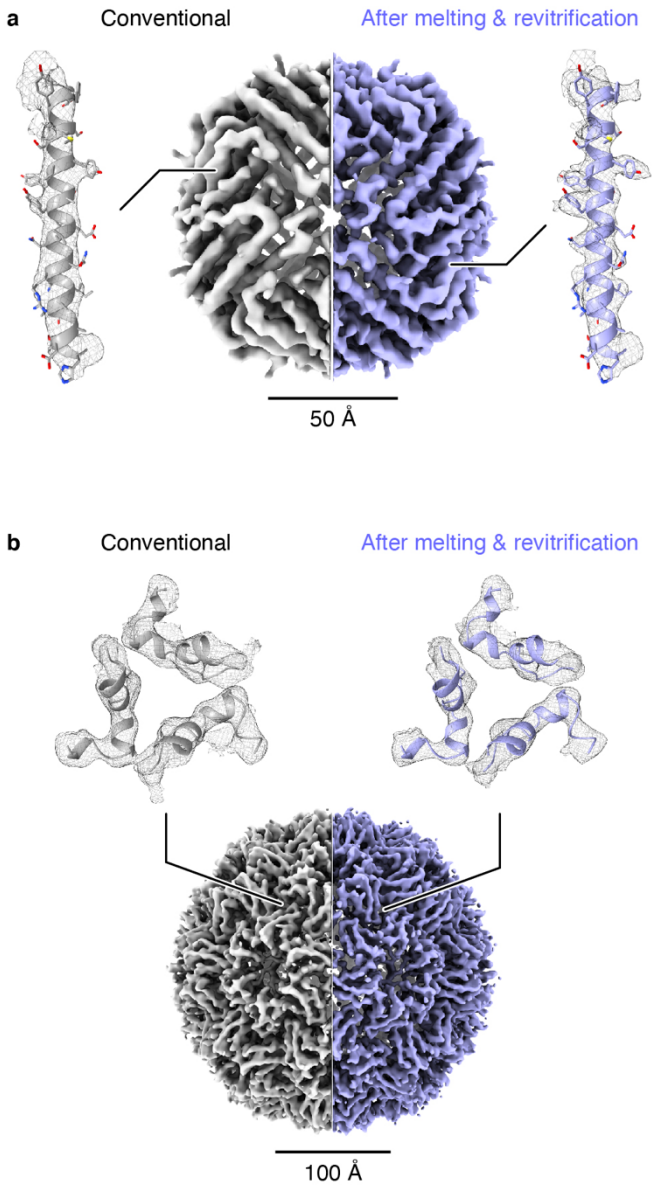

Figure 2. Comparison of single-particle reconstructions obtained from conventional and revitrified cryo samples. (a) Reconstructions of apoferritin from a conventional cryo sample (left, 4.57 Å resolution) and a melted and revitrified cryo sample (right, 4.25 Å). Details are shown for the densities of an alpha helix that has been fitted with PDB model 6V21.[31] (b) Single-particle reconstructions of CCMV from a conventional cryo sample (left, 4.98 Å) and a melted and revitrified cryo sample (right, 5.20 Å). Details of the densities of the capsid are shown in the vicinity of the quasi three-fold symmetry axis. The densities have been fitted with PDB model 1CWP.[32] The structures from conventional and revitrified samples are indistinguishable within the resolution of our instrument.

The interaction of the particles with the 532 nm laser beam is only indirect, since neither the particles nor the vitreous ice film absorb visible light, which prevents any type of photodamage. Instead, the laser heats the holey gold film of the specimen grid, which then melts the vitreous ice through fast heat diffusion. We have previously shown that the sample temperature can be controlled to prevent heat denaturation of the particles. In particular, evaporative cooling provides a negative feedback that stabilizes the sample temperature.[26 27]

While the sample is liquid, the particles may interact with the interface between the water film and the vacuum of the microscope. Interactions with the air-water interface have previously been shown to lead to particle denaturation.[35] However, the number of such collisions on the timescale of our experiment, tens of microseconds, is significantly lower than during the plunge-freezing process, where the time between blotting and vitrification is on the order of a second. Furthermore, it has previously been concluded that during this time, a layer of unraveled proteins forms at the aqueous surface that protects particles from reaching the interface.[36 37] We therefore expect the number of collisions that lead to denaturation to be small as long as the thickness of the sample remains large enough.

The rapid revitrification of the sample after the laser pulse should certainly not damage the particles, since it is well established that vitrification preserves the structure of a protein. In fact, the significantly higher cooling rate in our experiment [27], compared with that typically reached during plunge freezing[14 19], should be better suited to trap the room temperature structure of proteins. The melting step resembles the revitrification process in that it occurs on the same timescale of a few microseconds, just with the temperature evolution reversed.[27] One notable difference, however, is that cubic ice forms during the early stages of laser heating, which only melts once the temperature exceeds 273 K.[26] While the formation of cubic ice crystals could conceivably damage the proteins, this does not appear to be the case. In fact, it has recently been shown that the structure of proteins in devitrified cryo samples is unchanged and that devitrification can even be used to reduce sample drift and improve resolution.[38]

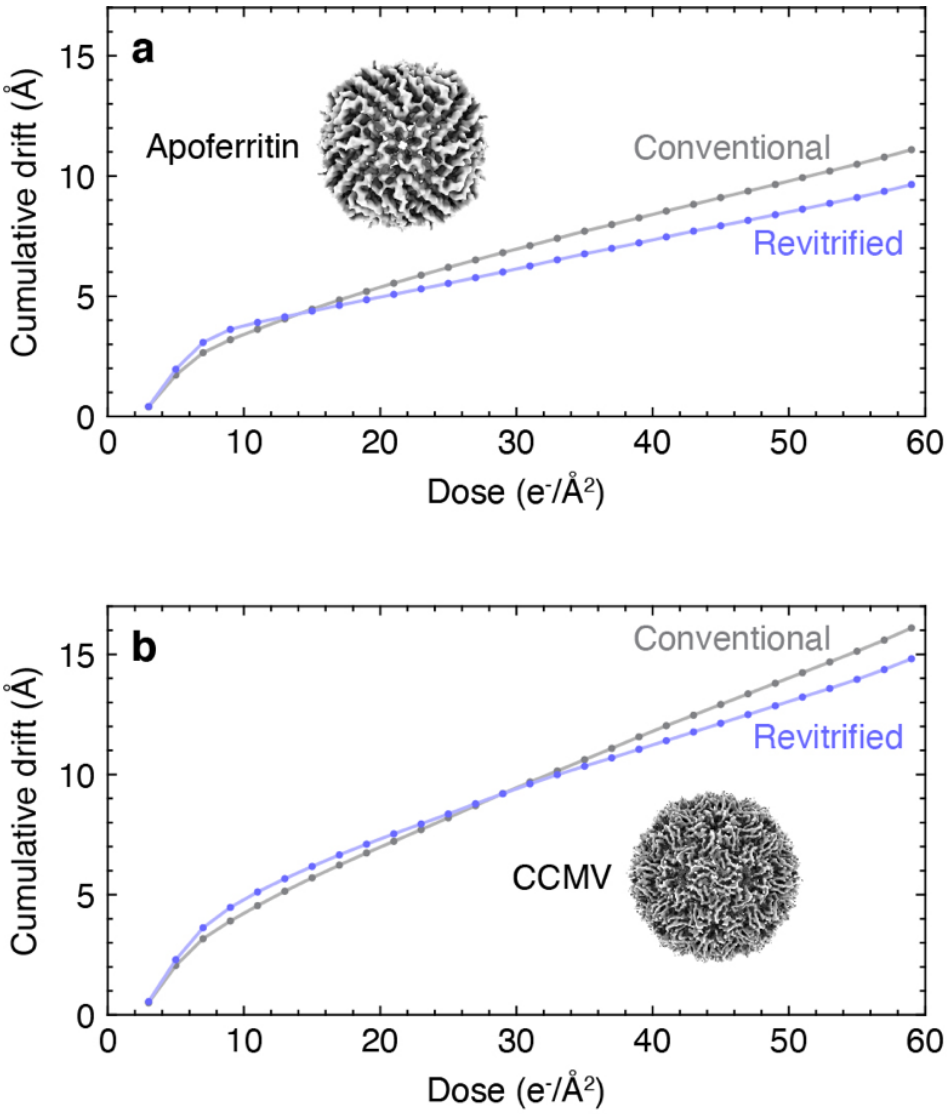

Figure 3. Comparison of sample drift in conventional and revitrified cryo samples. (a) Average cumulative specimen drift of apoferritin in a conventional cryo sample (grey) and a melted and revitrified cryo sample (purple). (b) Average cumulative specimen drift of CCMV in a conventional cryo sample (grey) and a melted and revitrified cryo sample (purple).

While we conclude that the structure of the proteins is not altered, an important related question is whether melting and revitrification changes the properties of the ice. In particular, it is important to establish how it affects the beam-induced motion that occurs during imaging and that limits the obtainable spatial resolution. Such motion arises when mechanical stresses in the vitreous ice, which have built up during plunge freezing, are released under electron irradiation.[1 2 39 40 41 42 43] Figure 3a shows that the average cumulative drift of the apoferritin particles, which is displayed as a function of the electron dose, follows a typical behavior for both the conventional (grey) and revitrified cryo samples. They initially drift quickly, before slowing to a lower and constant drift rate after a dose of 10–20 electrons/Å^2. The revitrified samples exhibit a slightly larger initial drift, but a smaller asymptotic drift rate. Their average cumulative drift therefore drops below that of the conventional samples after 15 electrons/Å^2. It is 1.5 Å lower at a dose of 60 electrons/Å^2, for a total drift of 10 Å. Qualitatively similar, although less pronounced differences are observed for the beam-induced motion of the CCMV samples (Figure 3b). The cumulative drift of the rivitrified samples drops below that of the conventional samples after 30 electrons/Å^2 and is 1.3 Å lower at a dose of 60 electrons/Å^2, for a total drift of 15 Å.

We conclude that revitrified samples exhibit comparable amounts of beam-induced motion to conventional samples, an observation that can shed new light on the mechanism that causes stress buildup in the ice during vitrification. It has been proposed that this stress results from the large temperature difference during plunge freezing between the holey gold film and the grid bars. Because of their large heat capacity, the bars cool more slowly and thus exert a compressive force on the vitreous ice film once they contract.[42 43] Since melting and revitrification is highly localized and the grid bars remain at cryogenic temperatures throughout the entire process, this mechanism alone cannot easily explain the beam-induced motion of the revitrified samples.[26 27] Our results are also seemingly at odds with the previous observation that drift increases with vitrification speed, which has been ascribed to the fact that faster cooling provides less time for stresses in the ice to dissipate during plunge freezing.[42 44] Since the cooling rate during revitrification is almost two orders of magnitude higher, one would therefore expect the beam-induced motion to become even more pronounced. We speculate that this is not the case since revitrification removes stresses that arise from large-scale deformations of the entire grid during plunge freezing [42 43], which compensates for the additional local stress induced by the high cooling rate.

5.4 Conclusion

Our experiments demonstrate that rapid melting and revitrification of cryo samples leaves embedded particles intact, providing a central piece of evidence that our approach is suitable to study the dynamics of proteins on the microsecond timescale. We find that proteins do not undergo structural changes within the spatial resolution afforded by our instrument. However, subtle structural differences, such as a side chain adopting a different conformation, may become apparent at higher resolution, a possibility that we have begun to explore.

Temperature-resolved cryo-EM experiments have long established that for some proteins, different conformational ensembles are obtained when the sample is cooled to a lower temperature before vitrification.[45] [46] Functional states present at physiological temperatures may even be depopulated during the plunge freezing process if the conformational transitions involved are fast relative to the cooling rate.[47] Melting and revitrification may provide a tool to investigate such effects systematically and even repopulate high-temperature states that are inaccessible at lower vitrification speeds. We also expect that the significantly faster cooling rate in our experiments should lead to a higher glass transition temperature (Angell, 2008)[48] and thus cause subtle changes in the structure of the water network surrounding the proteins, which should become evident at atomic resolution.[5] [6]

Our experiments also open up new possibilities for studying the vitrification process in real time [49] and how it leads to the buildup of stress that results in beam-induced motion. By suitably modulating the laser power, the cooling rate can be varied by more than three orders of magnitude, and the temperature evolution of the sample can be precisely controlled. This has been difficult to achieve with plunge freezing, where the complex fluid dynamics of the cryogen and its vapor phase as well as the heterogeneous heat transfer properties of the sample lead to widely varying vitrification speeds, even across a single specimen grid.[44] Even though we observe only small differences in the beam-induced motion of revitrified samples, our initial results suggest that it may be possible to release stress through irradiation with a sequence of laser pulses.

In the future, we envision using the microsecond melting and revitrification approach to study the dynamics of proteins, as outlined previously.[27] Several approaches are available for initiating dynamics. The intensity of the melting laser can be increased to heat the sample to elevated temperatures and thus induce a temperature jump, or a second laser pulse can be employed to directly trigger a photoactivated process. Alternatively, caged compounds can be used to provide a range of biomimetic stimuli by inducing a pH jump [50] or releasing ATP, ions, or even small peptides.[51] [52] Conveniently, these compounds can already be released with the sample still in the frozen state. Since the matrix of vitreous ice prevents the motions of the proteins, dynamics will only occur once the sample is melted. By revitrifying different areas of the sample after different amounts of time, reconstructions can then be obtained of several time points, so as to capture the complete structural evolution of the particles.

5.5 References

1. C.J. Russo, L.A. Passmore, Electron microscopy: Ultrastable gold substrates for electron cryomicroscopy, Science, 2014, 346, 1377-80.

2. K. Naydenova, P. Jia, C.J. Russo, Cryo-EM with sub-1 Å specimen movement, Science, 2020, 370, 223-226.

3. V.P. Dandey, W.C. Budell, H. Wei, et al., Time-resolved cryo-EM using Spotiton, Nature Methods, 2020, 17, 897-900.

4. R.B.G. Ravelli, F.J.T. Nijpels, R.J.M Henderikx, et al., Cryo-EM structures from sub-nl volumes using pin-printing and jet vitrification, Nature Communications, 2020, 11, 2563.

5. T. Nakane, A. Kotecha, A. Sente, et al., Single-particle cryo-EM at atomic resolution, Nature, 2020, 587, 152-156.

6. K.M. Yip, N. Fischer, E. Paknia, A. Chari, H. Stark, Atomic-resolution protein structure determination by cryo-EM, Nature, 2020, 587, 157-161.

7. X. Li, P. Mooney, S. Zheng, et al., Electron counting and beam-induced motion correction enable near-atomic-resolution single-particle cryo-EM, Nat Methods, 2013, 10, 584-590.

8. A. Punjani, J.L. Rubinstein, D.J. Fleet, M.A. Brubaker, cryoSPARC: algorithms for rapid unsupervised cryo-EM structure determination, Nat Methods, 2017, 14, 290-296.

9. J. Zivanov, T. Nakane, S.H.W. Scheres, Estimation of high-order aberrations and anisotropic magnification from cryo-EM data sets in RELION-3.1, IUCrJ, 2020, 7, 253-267.

10. E. Hand, Cheap shots, Science, 2020, 367, 354-358

11. Callaway E. Revolutionary cryo-EM is taking over structural biology. Nature. 2020, 578, 201.

12. J. Frank, Conformational Proteomics of Macromolecular Architecture: Approaching the Structure of Large Molecular Assemblies and Their Mechanisms of Action Ch. 13 World Scientific, 2004, Singapore.

13. B. Chen, J. Frank, Two promising future developments of cryo-EM: capturing short-lived states and mapping a continuum of states of a macromolecule, Microscopy (Oxf), 2016, 65, 69-79.

14. J. Frank, Time-resolved cryo-electron microscopy: Recent progress, J. Struct. Biol., 2017, 200, 303-306.

15. P. Schwander, R. Fung, A. Ourmazd, 2014 Conformations of macromolecules and their complexes from heterogeneous datasets, Phil. Trans. R. Soc. B, 2013, 369, 0567.

16. A. Hosseinizadeh, A. Dashti, P. Schwander, R. Fung, A. Ourmazd, Single-particle structure determination by X-ray free-electron lasers: Possibilities and challenges, Struct Dyn., 2015, 041601.

17. E.D. Zhong, T. Bepler, B. Berger, J.H. Davis, CryoDRGN: reconstruction of heterogeneous cryo-EM structures using neural networks, Nat Methods, 2021, 18, 176-185.

18. J.F. Ménétret, W. Hofmann, R.R. Schröder, G. Rapp, R.S. Goody, Time-resolved cryo-electron microscopic study of the dissociation of actomyosin induced by photolysis of photolabile nucleotides, J. Mol. Biol. 1991, 219, 139-144.

19. T.R. Shaikh, D. Barnard, X. Meng, T. Wagenknecht, Implementation of a flash-photolysis system for time-resolved cryo-electron microscopy, J. Struct. Biol., 2009, 165, 184-189.

20. Z. Lu, T.R. Shaikh, D. Barnard, X. Meng, H. Mohamed, A. Yassin, C.A. Mannella, R.K. Agrawal, T.M. Lu, T. Wagenknecht, Monolithic microfluidic mixing-spraying devices for time-resolved cryo-electron microscopy, J. Struct. Biol., 2009, 168, 388-95.

21. T.R. Shaikh, A.S. Yassin, Z. Lu, D. Barnard, X. Meng, T.M. Lu, T. Wagenknecht, R.K. Agrawal, Initial bridges between two ribosomal subunits are formed within 9.4 milliseconds, as studied by time-resolved cryo-EM, Proc. Natl. Acad. Sci. USA, 2014, 111, 9822-7.

22. J. Berriman, N. Unwin, Analysis of transient structures by cryo-microscopy combined with rapid mixing of spray droplets, Ultramicroscopy, 1994, 56, 241-252.

23. N. Unwin, Y. Fujiyoshi, Gating movement of acetylcholine receptor caught by plunge-freezing, J. Mol. Biol., 2012, 422, 617-634.

24. K. Henzler-Wildman, D. Kern, Dynamic personalities of proteins, Nature, 2007, 450, 964-972.

25. D.D. Boehr, H.J. Dyson, P.E. Wright, An NMR perspective on enzyme dynamics, Chem. Rev., 2006, 106, 3055-3079.

26. J.V. Voss, O.F. Harder, P.K. Olshin, M. Drabbels, U.J. Lorenz, Rapid melting and revitrification as an approach to microsecond time-resolved cryo-electron microscopy, Chemical Physics Letters, 2021, 778, 138812.

27. J.V. Voss, O.F. Harder, P.K. Olshin, M. Drabbels, U.J. Lorenz, Microsecond melting and revitrification of cryo samples, Struct. Dyn., 2021, 8, 054302.

28. P.K. Olshin, M. Drabbels, U.J. Lorenz, Characterization of a time-resolved electron microscope with a Schottky field emission gun, Struct. Dyn., 2020, 7, 054304.

29. T. Grant, N. Grigorieff, Automatic estimation and correction of anisotropic magnification distortion in electron microscopes, J. Struct. Biol., 2015, 192, 204-208.

30. T.D. Goddard, C.C. Huang, E.C. Meng, et al., UCSF ChimeraX: Meeting modern challenges in visualization and analysis, Protein Sci., 2018, 27, 14-25.

31. M. Wu, G.C. Lander, M.A. Jr. Herzik, Sub-2 Angstrom resolution structure determination using single-particle cryo-EM at 200 keV, J. Struct. Biol. X., 2020, 4, 100020.

32. J.A. Speir, S. Munshi, G. Wang, T.S. Baker, J.E. Johnson, Structures of the native and swollen forms of cowpea chlorotic mottle virus determined by X-ray crystallography and cryo-electron microscopy, Structure, 1995, 3, 63-78.

33. Y. Kayama, R.N. Burton-Smith, C. Song, et al., Below 3 Å structure of apoferritin using a multipurpose TEM with a side entry cryoholder, Sci. Rep. 2021, 11, 8395.

34. D.M. Vriezema, M. Comellas Aragonès, J.A. Elemans, J.J. Cornelissen, A.E. Rowan, R.J. Nolte, Self-assembled nanoreactors, Chem. Rev., 2005, 105, 1445-1489.

35. E. D'Imprima, D. Floris, M. Joppe, R. Sánchez, M. Grininger, W. Kühlbrandt, Protein denaturation at the air-water interface and how to prevent it, Elife, 2019, 8, 42747.

36. H. Yoshimura, T. Scheybani, W. Baumeister, K. Nagayama, Two-Dimensional Protein Array Growth in Thin Layers of Protein Solution on Aqueous Subphases, Langmuir, 1994, 10, 3290-3295.

37. R.M. Glaeser, Proteins, Interfaces, and Cryo-EM Grids, Curr. Opin. Colloid. Interface Sci., 2018, 34, 1-8.

38. J.P. Wieferig, D. J. Mills, W. Kühlbrandt, Devitrification reduces beam-induced movement in cryo-EM. IUCrJ, 2021, 8, 186–194.

39. E.R. Wright, C.V. Iancu, W.F. Tivol, G.J. Jensen. Observations on the behavior of vitreous ice at approximately 82 and approximately 12 K, J. Struct Biol., 2006, 153, 241-252.

40. A.F. Brilot, J.Z. Chen, A. Cheng, et al., Beam-induced motion of vitrified specimen on holey carbon film, J. Struct. Biol., 2012, 177, 630-637.

41. S.Q. Zheng, E. Palovcak, J.P. Armache, K.A. Verba, Y. Cheng, D.A. Agard, MotionCor2: anisotropic correction of beam-induced motion for improved cryo-electron microscopy, Nat. Methods, 2017, 14, 331-332.

42. T. Engstrom, J.A. Clinger, K.A. Spoth, et al., High-resolution single-particle cryo-EM of samples vitrified in boiling nitro-gen, IUCrJ. 2021, 8, 867-877.

43. R.E. Thorne, Hypothesis for a mechanism of beam-induced motion in cryo-electron microscopy, IUCrJ., 2020, 7, 416-421.

44. C. Wu, H. Shi, D. Zhu, K. Fan, X. Zhang, Low-cooling-rate freezing in biomolecular cryo-electron microscopy for recovery of initial frames, QRB Discovery, 2021, 2, 11.

45. N. Fischer, A.L. Konevega, W. Wintermeyer, M.V. Rodnina, H. Stark, Ribosome dynamics and tRNA movement by time-resolved electron cryomicroscopy, Nature, 2010, 466, 329-333.

46. C.Y. Chen, Y.C. Chang, B.L. Lin, C.H. Huang, M.D. Tsai, Temperature-Resolved Cryo-EM Uncovers Structural Bases of Temperature-Dependent Enzyme Functions, Journal of the American Chemical Society, 2019, 141, 19983-19987.

48. C.A. Angell, Insights into Phases of Liquid Water from Study of Its Unusual Glass-Forming Properties, Science, 2008, 319, 582-587.

48. R. Mehra, B. Dehury, K.P. Kepp, Cryo-temperature effects on membrane protein structure and dynamics, Physical Chemistry Chemical Physics, 2020, 22, 5427-5438.

49. P.K. Olshin, G. Bongiovanni, M. Drabbels, U.J. Lorenz, Atomic-Resolution Imaging of Fast Nanoscale Dynamics with Bright Microsecond Electron Pulses, Nano Lett., 2021, 13, 612-618.

50. M. Gutman, Methods of Biochemical Analysis Ch. 1 John Wiley & Sons, Inc., 1984, New York.

51. G.C. Ellis-Davies, Caged compounds: photorelease technology for control of cellular chemistry and physiology, Nature Methods, 2007, 4, 619-628.

52. Y. Shigeri, Y. Tatsu, N. Yumoto, Synthesis and application of caged peptides and proteins, Pharmacology & Therapeutics, 2001, 91,85-92.

Chapter 6: *Fast Viral Dynamics Revealed by Microsecond Time-Resolved Cryo-Electron Microscopy*[4]

6.1 Introduction

Cowpea chlorotic mottle virus is an icosahedrally symmetric plant virus in the *Bromoviridae* family that infects cowpea plants (*Vigna unguiculata*).[1] As with most viruses, CCMV faces the challenge of safely packaging its genetic material for transport, but then releasing it at the appropriate time to infect the host. As illustrated in Fig. 1, CCMV is thought to achieve this by detecting a change in its chemical environment upon entering the host cell, which causes its capsid to swell, increasing in diameter by about 10 %.[2] This extended state, which is unstable and disassembles, releases the viral RNA, thus infecting the host.[3] The capsid swelling is triggered by a decrease in the concentration of divalent ions and a simultaneous increase in pH upon entry into the host cell. This causes calcium ions to vacate their binding sites on the capsid interior, where they are complexed by several negatively charged sidechains.[3 4] Once the calcium ions are no longer present to compensate these negative charges, electrostatic repulsion causes the capsid to expand.[3 4 5] In the absence of divalent ions, the virus can also be artificially contracted by lowering the pH below 5, which protonates the negatively charged residues and thus removes their repulsion.[6]

[4] Reproduced with small adaptations from Harder, O.F., Barrass, S.V., Drabbels, M., Lorenz, U.J. Fast viral dynamics revealed by microsecond time-resolved cryo-EM. Nat Commun 14, 5649 (2023).

Personal contribution to this chapter: I conducted all the experimental work consisting of wet chemical preparation of virus solutions at different pH, precise addition of photoacid, cryo-sample preparation, structure determination of initial samples with single particle cryo-EM, ex-situ UV irradiation to activate the photoacid and in-situ revitrification. I collected all the high-resolution datasets, conducted preliminary data analysis in CryoSPARC, identified and visualized the apparent structural differences in CHIMERA.

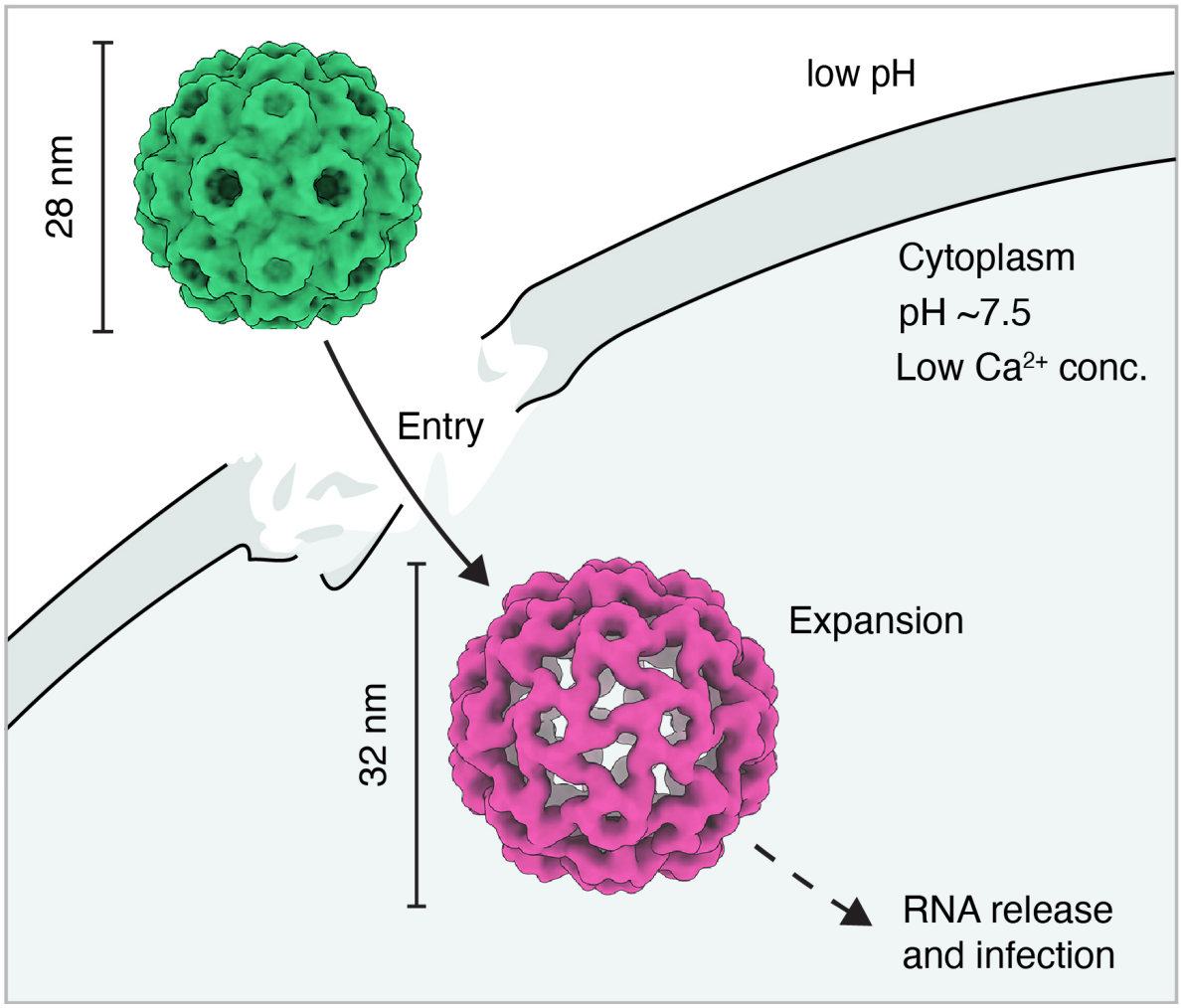

Figure 1. Illustration of the entry of CCMV into the plant cell. The virus in its contracted state (green) enters the plant cell through damaged sites in the cell wall. Once inside the cytoplasm, the virus experiences a decrease in the concentration of divalent ions and an increase in pH, which causes its capsid to swell. The extended state, which is unstable and disassembles, then releases the viral RNA, thus infecting the host.

Our understanding of how the CCMV capsid functions has remained incomplete due to a lack of direct observations of the fast motions of this intricate nanoscale machine, or methods that would enable such observations. A comparison of the contracted and expanded virus structures[6] suggests that the mechanics of the capsid motion must involve several large-scale translations and rotations of the capsid proteins. However, it is unclear whether they occur in a concerted or asynchronous fashion. [3 5]

Moreover, it is unknown how fast these motions are. The pH induced contraction of a another icosahedral virus, Nudaurelia Capensis ω, was observed to be complete after 10 ms, but is thought to be significantly faster.[7] This suggests that the capsid motions of CCMV would be too fast to be captured by traditional time-resolved cryo-EM, which affords only millisecond time resolution.[8] Ultrafast x-ray crystallography[9] [10], while sufficiently fast, is likely not suitable either to study these dynamics, since the crystal environment would hinder the large-amplitude motions involved.[10 11]

The difficulty of observing the fast motions of the CCMV capsid exemplifies the broader challenge of observing proteins as they perform their tasks. This has largely remained elusive, which has left our understanding of protein function fundamentally incomplete.[12] In order to enable such observations, we have recently proposed microsecond time-resolved cryo-EM[13–17], which affords a time resolution of about 5 μs or better[13] and enables near-atomic resolution reconstructions.[17]

6.2 Results

Here, we employ microsecond time-resolved cryo-EM to observe the pH jump induced contraction of CCMV and elucidate its capsid mechanics. The experimental approach is illustrated in Fig 2a-d. Cryo samples of extended CCMV at pH 7.6 (containing no divalent ions) are prepared in the presence of a photoacid (NPE-caged proton). The pH of the cryo sample is then lowered to 4.5 by releasing the photoacid through UV irradiation (266 nm). Even though the fully contracted state of CCMV is the most stable at this low pH [18] (Fig. 2e), the matrix of vitreous ice surrounding the particles prevents their contraction, locking them in their extended configuration. However, when we rapidly melt the sample with a laser beam (532 nm, Fig. 2b), the particles begin to contract as soon as the sample is liquid (Fig. 2c). After 30 μs, we then switch off the heating laser, and the sample cools and revitrifies within microseconds, trapping the particles in their partially contracted configurations (Fig. 2d), which we subsequently image.

Figure 3a shows a single-particle reconstruction of CCMV in its extended state (4.1 Å resolution). The sample was plunge-frozen at pH 7.6, after which the pH was lowered to 4.5 by releasing the photoacid. The capsid has a diameter of 32 nm (Materials and Methods), with the disordered RNA in its interior not resolved. The reconstruction is indistinguishable from one obtained without first lowering the pH (Supplementary Fig. 2a). This confirms that the vitreous ice matrix has prevented the particles from contracting, even though the negatively charged residues whose repulsion keeps the capsid inflated are likely protonated due to the high proton conductivity of vitreous ice.[19] In contrast, a sample prepared at pH 5.0 yields the structure of the fully contracted state with a diameter of 28 nm (Fig. 3c). The resolution of 1.6 Å is considerably higher than that of the extended state, which is more flexible and prone to partial disassembly.

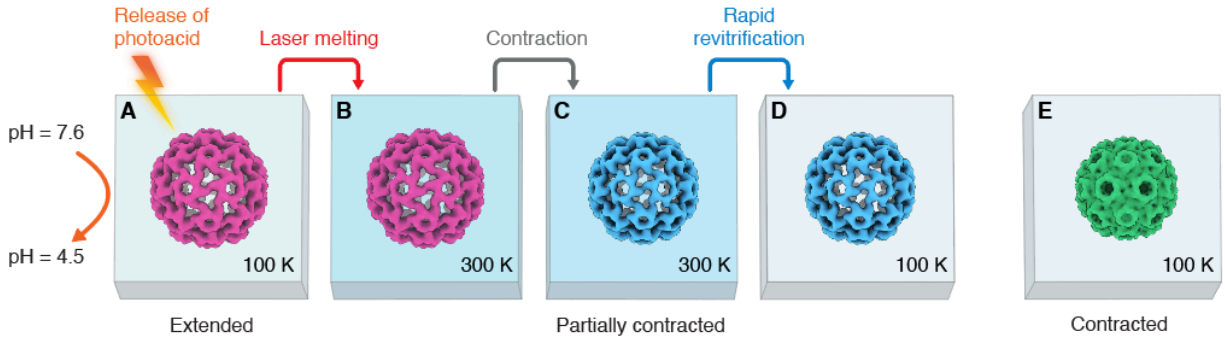

Figure 2. Microsecond time-resolved cryo-EM of the contraction of CCMV - experimental concept. (a) The expanded form of CCMV is prepared at pH 7.6 and plunge frozen in the presence of a photoacid (NPE-caged proton). The pH of the cryo sample is then lowered to 4.5 by releasing the photoacid through UV irradiation. At such a low pH, the contracted state of the capsid (e) is more stable. However, contraction cannot occur since the virus is trapped in the vitreous ice. (b) The sample is rapidly melted through irradiation with a laser beam. (c) Once the sample is liquid, the capsid starts to contract. (d) The laser is switched off, which causes the sample to cool and revitrify within microseconds, trapping the virus in partially contracted configurations, which are subsequently imaged. (e) A reconstruction of the fully contracted virus is separately obtained from a sample prepared at pH 5.

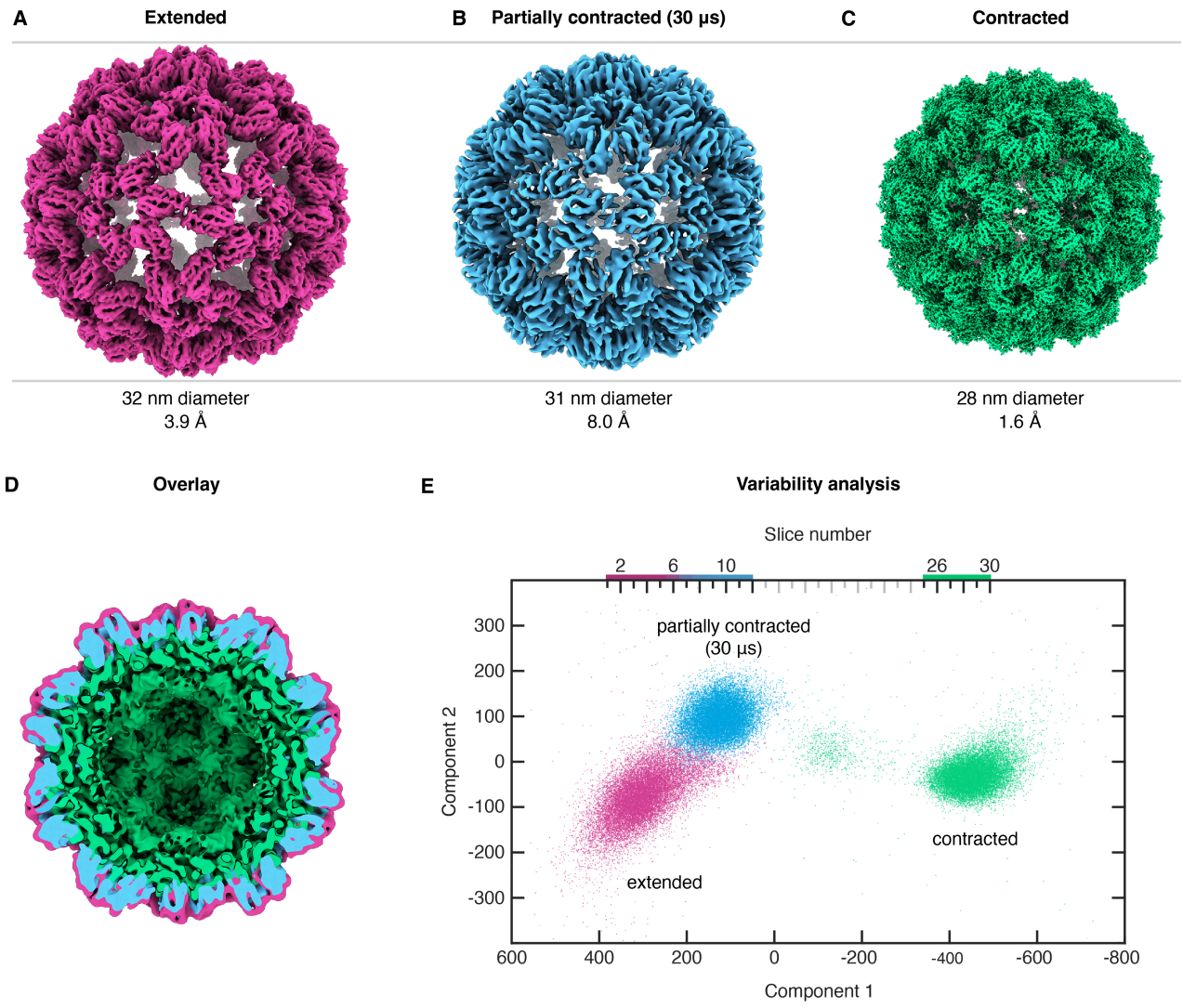

Figure 3. Single-particle reconstructions of different stages of the contraction of CCMV and variability analysis. (a-c) Comparison of the expanded state (plunge frozen at pH 7.6), the partially contracted configuration obtained with a 30 µs laser pulse, and the fully contracted state (prepared at pH 5.0). Before acquiring micrographs of the expanded state, the pH of the cryo sample was lowered to 4.5 by releasing a photoacid through UV irradiation. The particles nevertheless remain expanded because the surrounding matrix of vitreous ice prevents their contraction. (d) Cross section of an overlay of the three reconstructions (filtered to 8 Å), highlighting that the structure obtained after 30 µs of laser irradiation (blue) corresponds to a partially contracted configuration. (e) Variability analysis (cryoSPARC 4.0.1 20) of the extended, partially contracted, and fully contracted configurations (21,675 randomly selected particles of each). The particle distribution is shown as a function of the first two components, which are

predominantly associated with the diameter change of the particle (component 1) and with motions of the capsid proteins (component 2). The particle distribution is divided into 30 slices along the first component, and a reconstruction is obtained for each.

When we prepare CCMV in its extended state and lower the pH to 4.5, melting and revitrification of the sample allows the particles to partially contract. A reconstruction from a revitrified sample (Fig. 3b, 8.0 Å resolution) features a particle diameter of 31 nm, which lies in between that of the extended and the contracted configurations. This is also evident in Fig. 3d, which shows a cross section of the three reconstructions overlayed. Since the particles do not contract in samples that are UV irradiated, but do not contain any photoacid (Supplementary Fig. 2b), we conclude that the contraction is induced by the pH jump.

The partially contracted CCMV particles obtained after revitrification feature substantial conformational heterogeneity, which limits the resolution of the reconstruction in Fig. 3b to 8.0 Å. This is confirmed by a variability analysis (cryoSPARC 4.0.1).[20] Figure 3e displays the distribution of the particles in the extended, intermediate, and contracted configurations (21,675 randomly selected particles of each) as a function of the first two variability components. The first component predominantly corresponds to a change in particle diameter, while the second is associated with motions of the capsid proteins. The three configurations appear as distinct clusters, with the extended and partially contracted ensemble closer to each other and partly overlapping. Interestingly, the variability analysis in Fig. 3e suggests that the reaction path may be curved, indicating that different motions involved in the contraction process occur on different timescales.

An analysis of the translations and rotations of the capsid proteins confirms that contraction involves different timescales. We divide the particle distribution in Fig. 3e into 30 equally spaced slices along the first variability component and perform a reconstruction for each (Supplementary Fig. 4). We then dock atomic models of the extended configuration into slices 1–12 (extended and partially contracted particles) and of the contracted configuration into slices 25–30 (fully contracted particles), from which we determine the motions of the capsid proteins (Supplementary Methods). Figure 4a illustrates these motions, with the icosahedral capsid shown in its extended form. The 180 identical capsid proteins are arranged in 12 pentamers and 20 hexamers. The asymmetric unit (highlighted) contains three subunits A, B, and C (magenta, green, and blue, respectively). Figure 4b displays the particle diameter as a function of the slice number, with the diameter measured along the five-fold symmetry axis (indicated in Fig. 4a). In slices 1–5, which contain extended particles, as well as in slices 25–30, which contain fully contracted particles, the diameter is constant. In contrast, a continuous distribution of diameters is found for the partially contracted particles in slices 8–12, with the particle diameter in slice 12 about halfway between the fully extended and contracted configurations. This wide distribution highlights the conformational heterogeneity of the ensemble obtained after melting and revitrification. Evidently, the particles contract at different speeds.

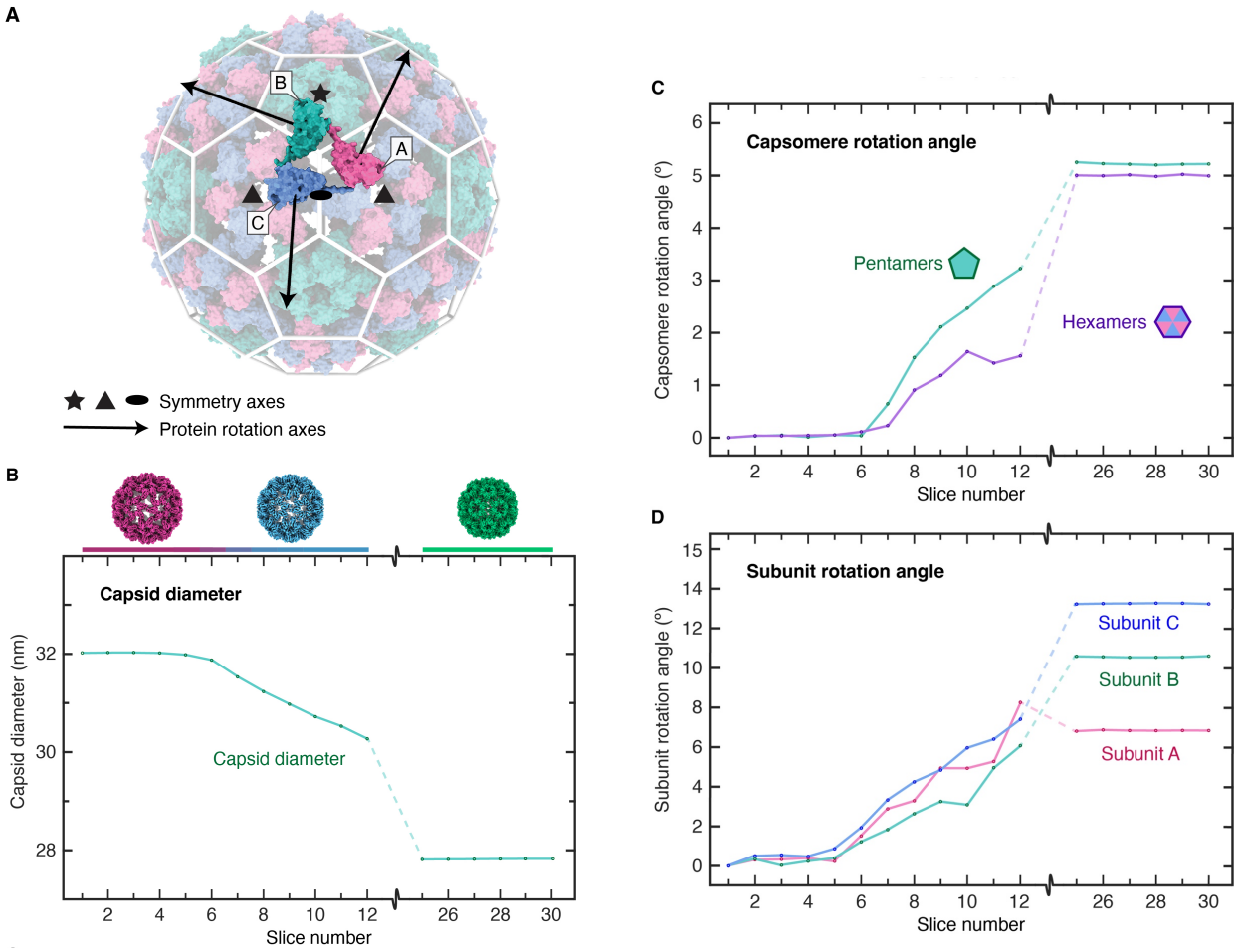

Figure 4. Analysis of the capsid motions involved in the contraction of CCMV. (a) Geometry of the icosahedral capsid (extended form). The asymmetric unit (highlighted) contains three protein subunits A, B, and C (magenta, green, and blue, respectively). Five-, three-, and two-fold symmetry axes are indicated with a star, triangle, and ellipse, respectively. Arrows indicate the rotation axes of the capsid proteins. (b-d) Analysis of the motions of the capsid proteins. The particle distribution in Fig. 3e is divided into 30 slices along the first component, and reconstructions are obtained for each. Atomic models are then docked into the density, from which the motions of the capsid proteins are extracted for each slice. (b) Particle diameter as a function of slice number. (c) Rotation angles of the capsid pentamers and hexamers. (d), Angles of the superimposed rotation of the A, B, and C subunits around the rotation axes indicated with arrows in (a).

The contraction of CCMV is accompanied by a simultaneous anticlockwise rotation of the pentamers and hexamers, which are both rotated by about 5 degrees in the fully contracted state. Figure 4c displays the rotation angles as a function of slice number. It reveals that the pentamers rotate about twice as fast as the hexamers, adopting a rotation angle of over 3 degrees in slice 12, while the hexamers reach only about 1.5 degrees. This rotation of the capsomeres is accompanied by a superimposed rotation of the capsid subunits around the axes indicated with black arrows in Fig. 4a. This rotation causes the capsomeres to adopt a domed structure in the contracted state. Figure 4d reveals that subunits A–C rotate with similar speeds. However, whereas subunit A has already reached its final rotation angle of ~7 degrees in slice 12, subunits B and C have completed only about half their rotations of ~11 and ~13 degrees, respectively. Clearly, while the different motions of the capsid proteins occur simultaneously, they are associated with different timescales.

Our experiments elucidate the capsid mechanics of the pH jump induced contraction of CCMV. Given the large amplitude of the motions involved, the contraction is surprisingly fast, with some particles completing half the contraction within the time window imposed by the 30 μs laser pulse. The process thus resembles a collapse that is triggered when the electrostatic repulsion is removed that keeps the capsid inflated. While this collapse is a concerted process, the associated translations and rotations of the capsid subunits occur on slightly different timescales, which results in a curved reaction path. Our analysis also reveals a large spread in the speed with which the particles contract. This is an expected result since the contraction occurs in a dissipative medium. For the same reason, conformational heterogeneity will likely be a feature of most protein dynamics than can be observed with microsecond time-resolved cryo-EM. It is therefore advantageous to design experiments such that they start from a homogeneous ensemble. As we have shown here, conformational sorting [21,22] will be crucial to obtain detailed structural information and elucidate reaction paths. We note that CCMV exists in three virions, which each package a different RNA strand [23,24] and will therefore likely contract at slightly different speeds. A further contribution to the observed spread in contraction speeds will likely arise from small variations in the temperature evolution of the revitrified area.[13]

While we have previously characterized our technique with the help of proof-of-principle experiments, we here show that microsecond time-resolved cryo-EM can be successfully employed to study fast protein dynamics that occur *in vivo*. We demonstrate a general approach for triggering such dynamics with the help of photorelease compounds.[14] Instead of uncaging the compound while the sample is liquid, we already do so with the sample still in its vitreous state. This offers the advantage that much larger changes in the chemical environment of the embedded particles can be induced, in particular for caged compounds with small quantum yields. Our experiments confirm that while the particles remain trapped in the matrix of vitreous ice, they cannot react to this stimulus, but will only begin to undergo conformational dynamics once the sample is melted with the laser beam. It should be possible to extend this principle to a wide range of other stimuli that can be applied with photorelease compounds, including caged small molecules, ATP, ions, amino acids, or peptides.[25,26] This suggests that microsecond time-resolved cryo-EM will be broadly applicable and that it has the potential to elucidate the dynamics of a wide variety of proteins that previously were too fast to be observed.

It is difficult to conceive how a similarly detailed view of the fast structural dynamics of the CCMV contraction could have been obtained with any other technique. This is particularly true for methods that do not offer a sufficiently high time resolution and are therefore limited to observing proteins at equilibrium. For example, an ordinary conformational analysis of a cryo sample prepared under equilibrium conditions would be unable to access the partially contracted transient configurations that we observe. This highlights the need for fast observations of protein dynamics under out-of-equilibrium conditions. In fact, it is a defining feature of life that it occurs far from equilibrium.[27] By enabling fast observations of non-equilibrium dynamics, microsecond time-resolved cryo-EM thus promises to fundamentally advance our understanding of living systems.

Data availability: The data that support the findings of this study are available from the corresponding author upon request. The maps of extended, partially contracted, and contracted CCMV from Fig. 3a–c have been deposited on EMDB

EMD-16790 [https://www.ebi.ac.uk/pdbe/entry/emdb/EMD-16790]

EMD-16798[https://www.ebi.ac.uk/pdbe/entry/emdb/EMD-16978]

EMD-16400 [https://www.ebi.ac.uk/pdbe/entry/emdb/EMD-16400]

together with the maps of extended CCMV in Supplementary Fig. 2:

EMD-16857 [https://www.ebi.ac.uk/pdbe/entry/emdb/EMD-16857]

EMD-16858 [https://www.ebi.ac.uk/pdbe/entry/emdb/EMD-16858]

The corresponding data set are accessible on EMPIAR:

EMPIAR-11487, EMPIAR-11473, EMPIAR-11461, EMPIAR-11489, EMPIAR-11488

The atomic coordinates of the models of extended and contracted CCMV are available on wwPDB:

8CPY [https://doi.org/10.2210/pdb8CPY/pdb]

8C38 [https://doi.org/10.2210/pdb8C38/pdb]

Code availability: Computer code used to generate the results of this paper are available from the corresponding author upon reasonable request.

6.3 References

1. A.F.S. Mello, A.J. Clark, K.L. Perry, Capsid protein of cowpea chlorotic mottle virus is a determinant for vector transmission by a beetle, J. Gen. Virol. 91, 545–551 (2010).

2. L. H. Wegner, et al., Biochemical and biophysical pH clamp controlling Net H^+ efflux across the plasma membrane of plant cells, New Phytol. 230, 408–415 (2021).

3. F. Tama, C. L. Brooks, The mechanism and pathway of pH induced swelling in cowpea chlorotic mottle virus, J. Mol. Biol. 318, 733–747 (2002).

4. R. Konecny, et al., Electrostatic properties of cowpea chlorotic mottle virus and cucumber mosaic virus capsids, Biopolymers 82, 106–120 (2006).

5. Y. Miao, J. E. Johnson, P. J. Ortoleva, All-atom multiscale simulation of cowpea chlorotic mottle virus capsid swelling, J. Phys. Chem. B. 114, 11181–11195 (2010).

6. J. A. Speir, S. Munshi, G. J. Wang, T. S. Baker, J. E. Johnson, Structures of the native and swollen forms of cowpea chlorotic mottle virus determined by X-Ray crystallography and cryoelectron microscopy, Structure. 3, 63–78 (1995).

7. T. Matsui, H. Tsuruta, J. E. Johnson, Balanced electrostatic and structural forces guide the large conformational change associated with maturation of T = 4 virus, Biophys. J. 98, 1337–1343 (2010).

8. M.-E. Mäeots, R.I. Enchev, Structural dynamics: review of time-resolved cryo-EM, Acta Crystallogr. Sect. Struct. Biol. 78, 927–935 (2022).

9. H. Ki, K.Y. Oang, J. Kim, H. Ihee, Ultrafast X-Ray crystallography and liquidography, Annu. Rev. Phys. Chem. 68, 473–497 (2017).

10. G. Brändén, R. Neutze, Advances and challenges in time-resolved macromolecular crystallography, Science 373, eaba0954 (2021).

11. J. Heberle, T. Gensch, When FT-IR spectroscopy meets X-ray crystallography, Nat. Struct. Biol. 8, 195–197 (2001).

12. K. Henzler-Wildman, D. Kern, Dynamic personalities of proteins, Nature 450, 964–972 (2007).

13. J.M. Voss, O.F. Harder, P.K Olshin, M. Drabbels, U.J. Lorenz, Microsecond melting and revitrification of cryo samples, Struct. Dyn. 8, 054302 (2021).

14. J.M. Voss, O.F. Harder, P.K. Olshin, M. Drabbels, U.J. Lorenz, Rapid melting and revitrification as an approach to microsecond time-resolved cryo-electron microscopy, Chem. Phys. Lett. 778, 138812 (2021).

15. O.F. Harder, J.M. Voss, P.K Olshin, M. Drabbels, U.J. Lorenz, Microsecond melting and revitrification of cryo samples: protein structure and beam-induced motion, Acta Crystallogr. Sect. Struct. Biol. 78, 883–889 (2022).

16. G. Bongiovanni, O.F. Harder, M. Drabbels, U.J. Lorenz, Microsecond melting and revitrification of cryo samples with a correlative light-electron microscopy approach, Front. Mol. Biosci. 9, 1044509 (2022).

17. G. Bongiovanni, O.F. Harder, J.M. Voss, M. Drabbels, U.J. Lorenz, Near-atomic resolution reconstructions from in situ revitrified cryo samples. Acta Crystallogr. Sect. Struct. Biol. 79, 473–478 (2023).

18. L. Lavelle, J.P. Michel, M. Gingery, The disassembly, reassembly and stability of CCMV protein capsids, J. Virol. Methods 146, 311–316 (2007).

19. N.N. Khusnatdinov, V.F. Petrenko, Experimental study of ice electrolysis under UV irradiation, J. Phys. Chem. B. 101, 6208–6211 (1997).

20. A. Punjani, J.L. Rubinstein, D.J. Fleet, M.A. Brubaker, cryoSPARC: algorithms for rapid unsupervised cryo-EM structure determination, Nat. Methods 14, 290–296 (2017).

21. S. Jonić, Cryo-electron microscopy analysis of structurally heterogeneous macromolecular complexes, Comput. Struct. Biotechnol. J. 14, 385–390 (2016).

22. B. Toader, F. J. Sigworth, R. R. Lederman, Methods for Cryo-EM single particle reconstruction of macromolecules having continuous heterogeneity. J. Mol. Biol., 168020 (2023).

23. J.J. Bujarski, Bromoviruses (Bromoviridae). in Encyclopedia of Virology 260–267 (Elsevier, 2021).

24. A. Chakravarty, A.L.N. Rao, Modulation of Capsid Dynamics in Bromoviruses by the Host and Heterologous Viral Replicase, J. Virol. 97, e01284-22 (2023).

25. G.C.R. Ellis-Davies, Caged compounds: photorelease technology for control of cellular chemistry and physiology, Nat. Methods 4, 619–628 (2007).

26. D.C.F. Monteiro, E. Amoah, C. Rogers, A.R. Pearson, Using photocaging for fast time-resolved structural biology studies, Acta Crystallogr. Sect. Struct. Biol. 77, 1218–1232 (2021).

27. E. Schrödinger, R. Penrose, What is life?: With mind and matter and autobiographical sketches (Cambridge University Press, ed. 1, 1992;

Chapter 7: Conclusion and Outlook

7.1 Conclusion

Concluding this thesis, I would first like to highlight what has been achieved, discovered or gained in terms of knowledge during this work in a compact manner.

Achievements, in the sense of accomplished goals outlined during the inception of this thesis fall into two categories. First, the primary goal of combining time-resolved electron microscopy with methods from cryo-electron microscopy was achieved. On one hand, the temporal resolution of time-resolved cryo-EM has been improved by three orders of magnitude from a few milliseconds to a few microseconds. One the other hand, a new contribution to the field of time-resolved electron microscopy has been established where, potentially, a wide range of processes can now be resolved by in-situ revitrification of cryo-samples.

Second, a new approach to directly resolve protein dynamics has been developed: Currently, the entire workflow, all the way from laser-melting and revitrification of cryo-samples to reconstructing the density map of a transient ensemble, can be carried out routinely. At this point, the major hurdle to microsecond time-resolved cryo-electron microscopy is, just like in conventional cryo-EM, the preparation of samples and data treatment.

Discoveries, in the sense of insights gained by accident or fortune, are truly plentiful. Foremost, it was discovered that samples can be melted and vitrified within microseconds in the vacuum of an electron microscope. By fortune, evaporative cooling has precisely the right stabilizing effect on the sample temperature for it to remain in a range around room temperature, ideal for typical biological activity. The circumstance that no additional modifications such as enclosing layers of graphene or the addition of surfactants are necessary is a very welcome discovery that has allowed for a much faster and wider range of applications, such as the deposition and revitrification of amorphous solid water.[1]

Another exciting discovery is the fundamental properties of water in its asymmetric behaviour during heating and cooling. As characterized in Chapter 4, vitreous ice crystallizes within microseconds upon heating, while water crystallizes much slower than a few milliseconds upon cooling.

A very practical and useful discovery is the characteristic crystallization pattern around revitrified areas as outlined in Chapter 3. Colloquially termed "crater", this handy phenomenon makes it much easier to identify desired areas at lower magnifications with lower electron doses. Recently, we even demonstrated its visibility with optical microscopy.[2]

A general and more overarching discovery is that rapid cooling seems to produce different kinds of vitreous ice as hinted at by a wide range of discoveries: Build-up of charge on the vitreous ice film due to electron irradiation can lead to microlensing effects.[3] It was discovered that this microlensing effect can be discharged by increasing charge carrier mobility during laser heating.[4] Additionally, revitrified areas appear to be of a different structure as microlensing effects look visually different compared to the microlensing, previously observed for conventional vitreous ice.[4]

Beam-induced motion and restructuring of the ice has been found to be different as well. Moreso, it is at odds with current theories that propose a significant mismatch in temperature and cooling rates between the gold film and the comparatively much more massive grid bars.[5] In turn, this mismatch should lead to stress which manifests as beam induced motion when the film relaxes during electron irradiation.[5] With revitrification not leading to greater beam induced motion, we discovered that the current theories on beam induced motion seem to be incomplete.

Due to the rapid cooling, it is possible to discover and probe the vitreous ice film in conditions further from equilibrium than otherwise accessible with conventional plunge freezing. Crucially, proteins are more frequently found in non-equilibrium distributions, more clumped together and in different orientations compared to conventional cryo-samples.

Lastly, some knowledge in the sense of scientific insights into biology and protein dynamics has been gained. Foremost, we managed to elucidate biological processes by preparing and resolving transient configurations of cowpea chlorotic mottle virus particles. The microsecond viral capsid motion could be resolved and studied by applying microsecond time-resolved cryo-electron microscopy.

Given the interpretation of the transient density maps, its contraction process seems to involve large-scale translations and rotations of the capsid proteins. These motions occur at slightly different timescales, indicating that the capsid proteins move asynchronously during the contraction. Interestingly, the rotations of the pentamers and hexamers differ in magnitude as pentamers rotate about twice as fast as the hexamers during the contraction process. Overall, one could conclude that the contraction of the capsid is surprisingly fast, with some particles completing half of the contraction within the 30 µs time window imposed by the laser pulse. This demonstrates how efficiently the unstable extended capsid virus can respond to environmental cues by undergoing structural changes.

The partially contracted configurations of the capsid show significant conformational heterogeneity, indicating that the particles could contract at drastically different speeds and adopt various intermediate states between the fully extended and contracted configurations. Here, an investigation that can produce high-resolution density maps, maybe with more advanced reconstruction algorithms, is necessary to provide the insights required to fully understand the underlying mechanisms leading to the change in capsid size.

All of these observations align with the initially outlined issues regarding the study of protein dynamics. Many detailed and complex aspects of dynamic structures, like their heterogeneity, fragility, susceptibility to external influences or their intrinsic chaotic behaviour, are to be expected but have been, at least partially, addressed.

Additional knowledge was also added to the field of structural biology: High resolution density maps of cowpea chlorotic mottle virus in its fully contracted and extended conformation have been reconstructed and fitted with atomic models, respectively.

7.2 Ongoing Research

Aside from the previously presented results, there are further projects that have not been published as of this writing. Orthogonal and more technical is my work on addressing preferred orientation (or orientation bias) in cryo-samples by rapid melting and revitrification, a major issue for conventional cryo-EM.[6] Conceptually, during the few microseconds the proteins spend in liquid, proteins assume a more random orientation distribution. Rapid microsecond cooling, unlike slower millisecond cooling during plunge freezing, reduces the time proteins have to assume their preferred orientation.

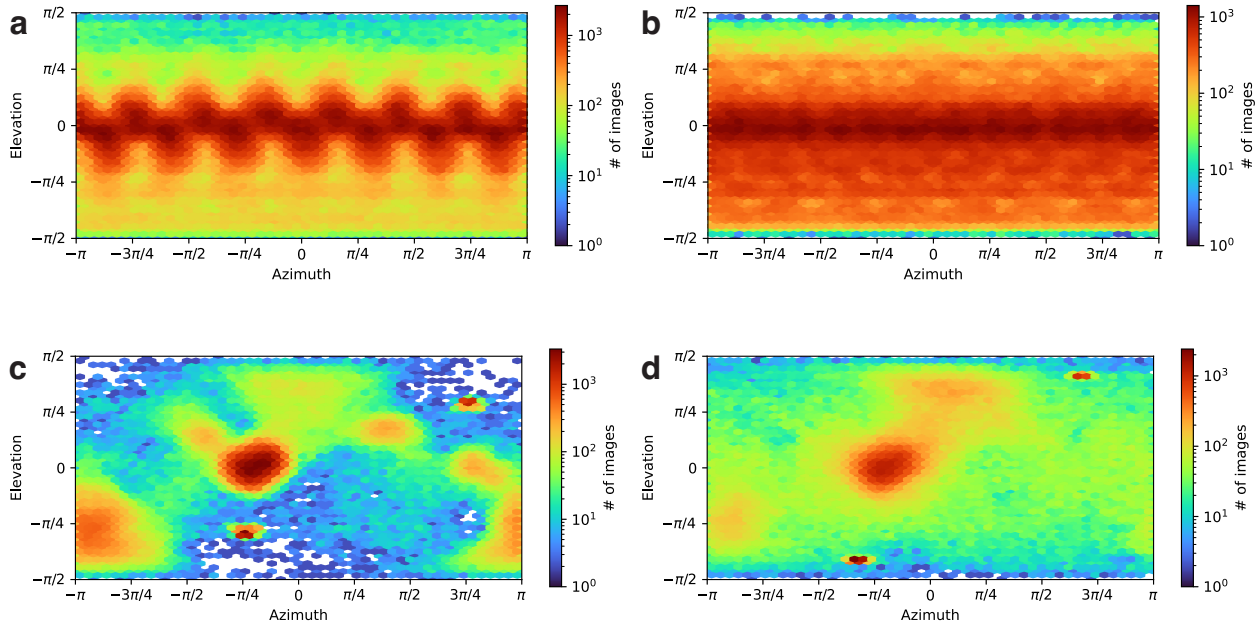

Figure 7. Orientation distribution plot of T20S Proteasome before (a) and after (b) revitrification. Orientation distribution plot of 50S Ribosome before (c) and after (d) revitrification.

Two systems that exhibit orientation bias, the 50S Ribosome and the T20S Proteasome, have been investigated. Both model systems sample orientation space more evenly (as in Fig. 7b, d) after revitrification compared to conventional plunge freezing (as in Fig. 7a, c). Notably, this is in line with the research on faster millisecond cooling times, such as Chamaeleon, which addresses orientation bias with the same principle.[7] An alternative explanation might be the formation of crystals during the rapid melting, leading to the physical displacement and reorientation of proteins. In the context of this work, a complementary approach relying on gold grids instead of self-wicking grids has been developed.

7.3 Outlook

Looking to the future, three areas of research seem promising to generate significant and long-term contributions to the field. First and foremost, microsecond time-resolved cryo-electron microscopy should be employed to study fast protein dynamics and produce further biological insights. Second, microsecond time-resolved cryo-EM should be improved to increase the range of possible experiments. Finally, the overarching vision is to combine microsecond time-resolved cryo-EM with advanced computational methods. Ideally this can realize a future where investigations into protein dynamics and protein function are conducted routinely and frequently.

Very similar to cowpea chlorotic mottle virus is adeno-associated virus with already well-resolved low and high pH conformations.[9] Following the approach applied to study CCMV, intermediates for adeno-associated virus could be prepared and resolved. Adeno-associated virus and any insights into its life-cycle are of great interest for gene therapy as AAV is currently one of the safest and most effective delivery system.[10]

As for pH-sensitive proteins, hemagglutinin (HA) promises great insights: Hemagglutinin acts as a membrane fusing protein during the infection cycle of the influenza virus.[11] Membrane fusion is initiated by a local decrease in pH, which could be triggered experimentally just as laid out in Chapter 6. Investigations into hemagglutinin's structural dynamics have already been carried out by high-speed atomic force microscopy.[12] But the preparation and resolution of intermediates during membrane fusion with microsecond time-resolved cryo-EM might provide further understanding, insights or ideas for vaccine and drug development.

In my opinion, melting and revitrification should be widely used to aid to structural biology in solving structures with preferred orientation. The major advantage is that this approach only relies on holey gold foil grids, which nowadays are standard tools in state-of-the-art cryo-electron microscopy. Hence, many sample preparation protocols can be expected to transfer seamlessly.

To improve the range of possible experiments, the timescales currently accessible by microsecond time-resolved cryo-EM have to be extended. There are several conceivable strategies that could allow for nanosecond temporal resolution. Equally, the gap to the millisecond regime could be bridged by employing a variety of approaches. For example, Chapter 3 demonstrates the possibility to sandwich a film of vitreous ice between two layers of graphene. Such a liquid cell can delay or prevent evaporation allowing the film to remain in liquid for several hundreds of microseconds. This approach has largely been left unexplored since these timescales are not directly relevant to the projects outlined. While slightly cumbersome, our current expertise has reached a state where the routine addition of graphene is more feasible.

A wide range of different triggers should be explored to allow the study of different systems. As mentioned in previous Chapters, there are a several photoactive compounds that can allow for changes in pH, the release of caged ions, caged ATP or other smaller caged molecules relevant to biology.[13] Ultimately, one can imagine several approaches to more precisely control concentration, activate or trigger compounds and even mix different types of proteins on-grid. Innovations of this kind will certainly allow stunning experiments when built on this foundational research.

Finally, I have the hope that this work can open up new opportunities for the field when combined with advanced computational techniques. As outlined in Chapter 1, Structural Biology has reached such an impressive state, especially with the advent of AlphaFold, that the goalpost for the field is slowly but surely shifting. With novel computational tools to study continuous conformational heterogeneity backed by powerful hardware, the eyes are set on understanding function and dynamics. The long-term vision is clear. Protein function has to be as easily accessible as static structures are today with computational means such as Alphafold.[14]

The first steps in such a direction have already been taken and show astonishing promise. Most recently, the interactions of small molecules with protein structures were modelled using a diffusive denoising approach.[15] Shockingly, it promises to model entire biological assemblies containing proteins, nucleic acids, small molecules, metals and covalent modifications given the sequences of the polymers and the atomic bonded geometry of the small molecules and covalent modifications.[15] From a long-term perspective, further advances will require experimental validation and larger training data sets to infer dynamics computationally. Such datasets will be provided by a large set of techniques where microsecond time-resolved cryo-EM is poised to play a crucial role.

For microsecond time-resolved cryo-EM experiments, advances in computational techniques will in turn improve the data analysis and modelling of conformational heterogeneity generally prevalent in biological systems. Deep neural networks can already make astonishing use of energy-based models or latent space representations as demonstrated by CryoDRGN.[16] Such tools could allow to generate images of transients along hypothetical reaction trajectories if the initial and final structures are provided. Even if microsecond time-resolved cryo-EM cannot provide a high-resolution reconstruction of transient configurations due to system-specific constraints, it might still capture poses of transients. These can be matched to generated ones in order to statistically verify a proposed trajectory in conformational space from experimental data.

In general, the field of protein dynamics seems to enter a period of high innovation driven fast-paced, accelerating self-reinforcing progress due to the newly discovered applications for AlphaFold that can be combined with already established or newly emerging experimental techniques.[17]

That is precisely why microsecond time-resolved cryo-EM finds itself today in a unique and fortunate position to contribute experimentally to the overarching vision of routinely understanding of a protein's dynamic nature. The method's seamless integration into conventional cryo-EM workflows promises that a large fraction of the work carried out for structural studies during the last decades can be translated directly, with comparatively little effort, into functional studies on the microsecond-scale.

7.4 References

1. C.R. Krüger, M.J. Mowry, G. Bongiovanni, et al., Electron diffraction of deeply supercooled water in no man's land. Nat Communications 14, 2812 (2023).

2. G. Bongiovanni, O.F. Harder, M. Drabbels, U.J. Lorenz, Microsecond melting and revitrification of cryo samples with a correlative light-electron microscopy approach, Front Mol Biosci. 2022 Nov 10;9:1044509.

3. C.J. Russo, R. Henderson, Charge accumulation in electron cryomicroscopy, Ultramicroscopy, Volume 187, 2018, Pages 43-49.

4. Chengcheng Yan, In Situ and Time-Resolved Electron Microscopy of Nanoscale Processes, Thesis, Chapter 4, 2023.

5. R.E. Thorne, Hypothesis for a mechanism of beam-induced motion in cryo-electron microscopy, IUCrJ, 7, 416–421, 2020.

6. Y. Tan, P. Baldwin, J. Davis et al., Addressing preferred specimen orientation in single-particle cryo-EM through tilting, Nat Methods 14, 793–796 2017.

7. D.P. Klebl, M.S.C. Gravett, D. Kontziampasis, et al., Need for Speed: Examining Protein Behavior during CryoEM Grid Preparation at Different Timescales. Structure. 2020 Nov 3;28(11):1238-1248.e4.

8. Zhou T, Tsybovsky Y, Gorman J, et al. Cryo-EM Structures of SARS-CoV-2 Spike without and with ACE2 Reveal a pH-Dependent Switch to Mediate Endosomal Positioning of Receptor-Binding Domains. Cell Host Microbe. 2020;28(6):867-879.e5.

9. J.J. Penzes, P. Chipman, N. Bhattacharya, A. Zeher, R. Huang, R. McKenna, M. Agbandje-McKenna, Adeno-associated Virus 9 Structural Rearrangements Induced by Endosomal Trafficking pH and Glycan Attachment, J Virol. 2021 Sep 9;95(19).

10. H.K.E. Au, M. Isalan, M. Mielcarek, Gene, Therapy Advances, A Meta-Analysis of AAV Usage in Clinical Settings. Front Med (Lausanne). 2022 Feb 9;8:809118.

11. S.J. Gamblin, S.G. Vachieri, X. Xiong, J. Zhang, S.R. Martin, J.J. Skehel, Hemagglutinin Structure and Activities. Cold Spring Harb Perspect Med. 2021 Oct 1;11(10).

12. K. Lim, N. Kodera, H. Wang et al., High-Speed AFM Reveals Molecular Dynamics of Human Influenza A Hemagglutinin and Its Interaction with Exosomes, Nano Letters, 2020, 20, (9), 6320-6328.

13. Ellis-Davies GC, Caged compounds: photorelease technology for control of cellular chemistry and physiology. Nat Methods. 2007 Aug;4(8):619-28.

14. A. Ourmazd, K. Moffat, E.E. Lattman, Structural biology is solved - now what?, Nat Methods 2022;19(1):24-26.

15. R. Krishna et al, Generalized Biomolecular Modeling and Design with RoseTTAFold All-Atom, bioRxiv (2023)

16. E.D. Zhong, T. Bepler, B. Berger, J.H. Davis, CryoDRGN: reconstruction of heterogeneous cryo-EM structures using neural networks, Nat Methods. 2021 Feb;18(2):176-185.

17. H.K. Wayment-Steele, A. Ojoawo, R.Otten et al. Predicting multiple conformations via sequence clustering and AlphaFold2. Nature (2023).

Appendix I – Supporting Information for Chapter 3

A1.1 Notes

Note S1. Graphene-enclosed cryo sample preparation

The graphene-enclosed cryo samples are prepared with the procedure illustrated in Fig. S1. The gold spacer is obtained by evaporating 30 nm of gold onto a Quantifoil TEM grid (R1.2/1.3 holey carbon film on 200 mesh copper, Fig. S1a,b). The coated grid is placed onto the surface of a concentrated aqueous solution of $(NH4)2S2O8$ for 15 minutes to etch away the copper mesh and is subsequently transferred to a bath of deionized water for 10 minutes to remove the etchant (Fig. S1c). The carbon/gold film is then transferred onto bilayer CVD graphene on copper foil (ACS Material, Fig. S1d). To remove water and improve the contact between the graphene and amorphous carbon layers, the assembly is gently heated on a hotplate for 10 minutes at 50 °C. Once dried, the entire assembly is floated on the surface of a $(NH4)2S2O8$ etching solution for approximately 2 hours to dissolve the copper foil (Fig. S1e). Once the copper has been completely removed, the assembly is transferred to a deionized water bath for 10 minutes in order to remove the etchant. Next, a 600 mesh gold TEM grid is submerged into the water and delicately drawn out to suspend the assembly onto the TEM grid (Fig. S1f). The grid is then dried on a hotplate for 10 minutes at 50 °C, after which a 10 μL drop of deionized water is placed on the surface of the gold film. Another multilayer graphene film (3-5 layers, ACS Material) is floated on the surface of a deionized water bath. The TEM grid is submerged in the water and withdrawn to suspend the graphene across the gold film and thus trap water in the holes of the gold film (Fig. S1g). The grid assembly is then blotted with filter paper for approximately 10 seconds to remove excess water and is immediately plunge frozen (Fig. S1h) and loaded into a cryo specimen holder.

Note S2. Preparation of cryo samples of GroEL

Cryo samples of GroEL were prepared on Quantifoil UltraAuFoil TEM grids (R1.2/1.3 holey gold film on 300 mesh gold or R2/2 holey gold film on 200 mesh gold, 50 nm film thickness). The grids were plasma cleaned for 30 seconds using an ELMO glow discharge system operating with negative glow discharge head polarity, 0.860 mA plasma current, and 0.2 mBar residual air pressure. A 3 μL drop of a 1.3 mg/mL GroEL solution (Takara Bio Europe SAS, used without further purification) was placed on each of the plasma cleaned grids. The grids were inserted into a Vitrobot MarkIV (Thermo Fisher Scientific) held at 100% relative humidity and 22 °C and were blotted with 595 filter paper for 2.5 seconds with a blotting force of -15. Immediately after blotting, the samples were vitrified by plunge freezing in liquid ethane.

Note S3. Rapid *in situ* melting and vitrification

All experiments were carried out with a modified JEOL 2200FS transmission electron microscope operating at 160 kV accelerating voltage (Fig. S2).[1] To induce rapid melting and vitrification, the sample is irradiated *in situ* with microsecond laser pulses (532 nm, tens of microseconds) that are obtained by chopping the output of a continuous laser with an acousto-optic modulator (20–80% rise and fall times of 73 ns and 134 ns, respectively, see Fig. S3c for the pulse shape). The laser beam is directed at the sample by means of a mirror located above the upper pole piece of the objective lens and strikes it at close to normal incidence. A 25 cm lens focuses the laser beam to a spot size of 24±1 μm FWHM, as measured by a knife edge scan at the sample location.

Note S4. Heat transfer simulations

Finite element heat transfer simulations of the temperature evolution of the sample under irradiation with microsecond laser pulses were performed with COMSOL Multiphysics. The simulation geometry is shown in Fig. S3a,b. A gold film (30 nm thickness) rests on top of an amorphous carbon substrate (20 nm thickness), which is supported by a 600 mesh gold TEM grid (14.5 μm wide and 10 μm thick bars, 30 μm x 30 μm viewing area). The amorphous carbon/gold film features a regular pattern of holes (1.2 μm diameter, 2.8 μm pitch) and supports a thin layer of vitreous ice (0–150 nm, Fig. S3b). In order to reduce computational cost, we have omitted the graphene sheets that enclose the cryo samples in our experiments. As the thickness of the graphene layers are small, their heat capacity and thermal conductivity are negligible compared to the remainder of the assembly [2], so that omitting them in the simulation does not change the temperature evolution. We have, however, considered that the graphene layers absorb the heating laser radiation and have included this contribution in our calculation of the total absorption cross section of the sample. The simulation area is limited to a square of 122.5 μm side length, which is more than five times larger than the laser spot size (24 μm FWHM, indicated by empty circles in Fig. S3a). At the boundaries of the simulated area, we fix the temperature to the initial temperature of the geometry (100 K) in order to account for the large heat capacity of the remainder of the sample. We note that even if we do not apply this boundary condition, the temperature evolution is virtually identical.

We use literature values for the temperature dependent heat capacity and thermal conductivity of gold [3] as well as for the thermal conductivity of amorphous carbon.[4] Since reliable low-temperature values for the heat capacity of amorphous carbon are not available [5], we use its room temperature value [6] and scale it to low temperatures assuming the temperature dependence for graphite.[7] We note that when we change the heat capacity of amorphous carbon in a wide range, the temperature evolution changes only nominally. The heat capacity and thermal conductivity of supercooled water are unknown in a wide temperature range known as 'no man's land', where rapid crystallization has so far prevented the study of its thermal properties.[8,9] We therefore use the heat capacity of supercooled water in silica nanopores instead, which is available for the whole temperature range.[10] For the thermal conductivity of water, we use its room temperature value, which is also close to that of amorphous ice at 100 K.[11]

The temperature of the entire geometry is initially set to 100 K. Heating with a 20 μs laser pulse is then simulated by placing a Gaussian heat source (24 μm FWHM) on the top surface of the gold film, with the heating rate calculated from the incident laser power and the absorption of both gold and graphene.[12 13 14] For the temporal structure of the 20 μs heating laser pulse, we use the experimentally determined pulse shape (black curve in Fig. S3c). In Fig. 4D and Fig. S3c, the heating laser power (35 mW) is chosen such that the temperature at the center of the laser focus plateaus at ~300 K when the laser beam is centered on the simulation geometry. We simulate three different positions of the laser focus (solid dots in Fig. S3a) and probe the evolution of the sample temperature in their center (Fig. S3c, no added layer of ice). While heating and cooling times remain virtually unchanged (~1 μs), the plateau temperature of the sample decreases as the laser focus approaches the bars of the TEM grid. Therefore, the distance of the sample to the bars of the TEM grid has to be taken into account when the laser power required for melting is calibrated *in situ*, as shown in Fig. 2. In the simulations reported in Fig. 4d, the laser beam was centered on the simulation geometry (red dot in Fig. S3a). For simulations that include a layer of vitreous ice, we report the temperature of the ice, not the temperature of the amorphous carbon/gold film, although they are nearly identical.

In order to understand how evaporative cooling affects the temperature evolution of the sample during irradiation with microsecond laser pulses, we perform heat transfer simulations using the experimental geometry from Fig. 5. A gold film (50 nm thickness) is supported by a 200 mesh gold TEM grid (38.5 μm wide and 15 μm thick bars, 86.8 μm x 86.8 μm viewing area). The gold film features a regular pattern of holes (2 μm diameter, 4 μm pitch). A thin layer of vitreous ice (100 nm thickness) fills the holes and covers both sides of the gold film. The simulation area is limited to a square of 190 μm side length. To account for the large heat capacity of the specimen grid, the gold bars extend 435 μm past the simulation area in each direction. The temperature of the entire geometry is initially set to 100 K.

Heating with a 15 μs laser pulse is simulated by placing a Gaussian heat source (24 μm FWHM) on the top surface of the gold film in the center of the simulation geometry. To account for evaporative cooling, we apply a negative heat source to both surfaces of the water film. The cooling rate is determined from the temperature-dependent enthalpy of evaporation [15] and the temperature-dependent evaporation rate [16] (Fig. S8a), which we calculate using literature values of the vapor pressure [17] assuming an evaporation coefficient of 1.[9]

We probe the temperature evolution of vitreous ice located in the middle of the central hole in the gold film. Fig. S8b shows the heating and cooling dynamics of the ice film for different laser powers. With a 40 mW laser pulse, the ice just barely surpasses the melting point. As the laser power is increased further, the plateau temperature of the sample increases only slightly, reaching 284 K at 120 mW. Evaporative cooling acts as a negative feedback that leads to a small variation in plateau temperature for a large range of laser powers

Note S5. Characterization of the temperature evolution and time resolution with time-resolved EM

The temperature evolution of the sample under irradiation with microsecond laser pulses (Fig. 4) was characterized with time-resolved electron microscopy. This technique uses short electron pulses to capture processes that are faster than the time resolution of the electron camera.[18] For these experiments, the temperature of the emitter is lowered until electron emission ceases. Short electron pulses (1 ns, ~10^4 electrons) are then generated by irradiating the Schottky emitter of the microscope with a UV laser pulse (266 nm, 1 ns, 200 nJ pulse energy). A precisely timed electron pulse is then used to record a selected area diffraction pattern of the sample at a specific point in time during irradiation with a microsecond laser pulse. The experiment is repeated stroboscopically in order to acquire a range of time frames and thus capture the entire heating and cooling dynamics of the sample. Every stroboscopic diffraction pattern was acquired with 8,000 electron pulses, and the dynamics at each position of the heating laser were recorded at least five times.

For the stroboscopic diffraction experiments, we reduced the power of the heating laser to 13 mW in order to minimize small irreversible deformations of the sample that slowly occur under exposure to thousands of laser pulses and that interfere with the stroboscopic experiment (see below). Our heat transfer simulations confirm that while different laser powers result in different plateau temperatures of the sample, they barely change the heating and cooling timescales, which are the figures of merit that we extract from the experiment.

Note S6. Analysis of the time-resolved diffraction patterns

For our analysis of the temperature evolution of the sample, we monitor the intensity of the (331), (420), and (422) reflections of the gold film (Fig. 4b). We note that if we choose different reflections, we obtain very similar, albeit noisier transients of the diffraction intensity.

The intensity of each selected diffraction spot is determined by integrating a rectangular region of interest centered around the diffraction spot (green boxes in Fig. S4c) and subtracting the intensity of the diffraction background, as determined from the average intensity of the areas marked in blue boxes in Fig. S4c. Over the course of a stroboscopic experiment (several hours), the electron beam intensity slowly varies and causes the intensities of the diffraction spots to change accordingly. To account for this effect, the diffraction intensities are normalized by the electron beam intensity, which we estimate with the following procedure.

We calculate the total intensity of the diffraction spots included in our analysis for time frames recorded before time zero and after 40 μs, when the sample temperature has returned to 100 K. We then use a spline of this total diffraction intensity to estimate the intensity the electron beam had when each individual time- resolved diffraction pattern was recorded. After normalization, we average the intensity of each diffraction spot over all delay scans and calculate the corresponding standard error. Both the average and error are weighted by the relative electron beam intensity of the frame. Finally, the average intensities of the diffraction spots are summed up to give the transients shown in Fig. 4c and Fig. S4d–f. The reported errors are obtained through error propagation.

In our analysis, we have excluded diffraction spots whose intensity changes irreversibly over the course of the stroboscopic experiment or that yield a very poor signal-to-noise ratio. We note that when this exclusion is not made, the transients obtained are very similar, albeit noisier, and the heating and cooling timescales we extract are virtually identical. Irreversible changes of the intensity of some diffraction spots occur as the gold film slowly deforms under exposure to thousands of laser pulses, which causes some grains to slowly move into or out of the diffraction condition. As noted above, we have reduced the power of the heating laser to minimize such effects. Diffraction spots that nevertheless exhibit such

irreversible changes are excluded from the analysis, as they would otherwise distort the stroboscopic measurement.

We have also excluded diffraction spots that exhibit obvious non-Debye-Waller behavior and whose intensity increases as the sample is being heated, instead of decreasing. Such behavior is frequently observed in nanocrystalline thin films and occurs as individual grains move into or out of the diffraction condition under the strain that laser heating induces. These effects may still be present for the diffraction spots included in our analysis. For a large enough sample, such effects should cancel out, so that Debye-Waller behavior is observed on average. However, this is not the case for the small number of grains in our experiment that fulfill the diffraction condition within the selected area (1.7 μm diameter). It is therefore important to note that one cannot easily draw conclusions about the magnitude of the induced temperature jump from the observed drop in diffraction intensity. For the same reason, the relative intensity drop observed in the measurements of Fig. S4d–f does not accurately reflect that the plateau temperature is highest in the center of the gold film in Fig. S4a. However, the determination of the heating and cooling times remains unaffected. We also note that if we do not exclude the diffraction spots whose intensity increases with temperature, the heating and cooling timescales do not change significantly.

Note S7. Fitting procedure for the heating and cooling times

In order to determine the heating and cooling times from the time-resolved diffraction experiments, we fit the logarithm of the relative diffraction intensity, log (I/I_0), which the Debye-Waller effect predicts to decrease linearly with temperature.[19] Here, I is the diffraction intensity and I_0 is the diffraction intensity before time zero. We fit the heating dynamics (≤ 20 μs) with the empirical piecewise function $f"(t)$,

$$\log\left(\frac{I}{I_0}\right) = f_1(t) = \begin{cases} 0 & \text{for } t \leq 0 \\ -a(1 - e^{-t/\tau_{heating}}) - bt & \text{for } t > 0 \text{ and } t \leq 20\ \mu s \end{cases}$$

where $\tau_{heating}$, is the heating time, and a and b are fit parameters. For the cooling dynamics after the end of the laser pulse at t = 20 μs, we fit the transient with the function $f\text{-}(t)$,

$$\log\left(\frac{I}{I_0}\right) = f_2(t) = f_1(t = 20\ \mu s) \cdot e^{-(t-20\ \mu s)/\tau_{cooling}} \qquad \text{for } t \geq 20\ \mu s$$

where $\tau_{cooling}$, is the cooling time.

In the stroboscopic experiments, we sampled the rapid heating and cooling of the sample with shorter time steps in order to better capture these fast dynamics. Without accounting for the uneven spacing of the data points, a least-squares fit would be biased towards the regions of high sampling rate. We therefore employ weighting factors in the fit that are inversely proportional to the standard error of the data point and inversely proportional to the sampling rate. The sampling rate is determined from the time steps between each data point and its nearest neighbors.

The heating and cooling times in the heat transfer simulations are determined in an analogous manner by fitting the temperature change, $T(t) - T(t < 0)$, with the functions $f"(t)$ and $f\text{-}(t)$ as described above.

A1.2 Figures

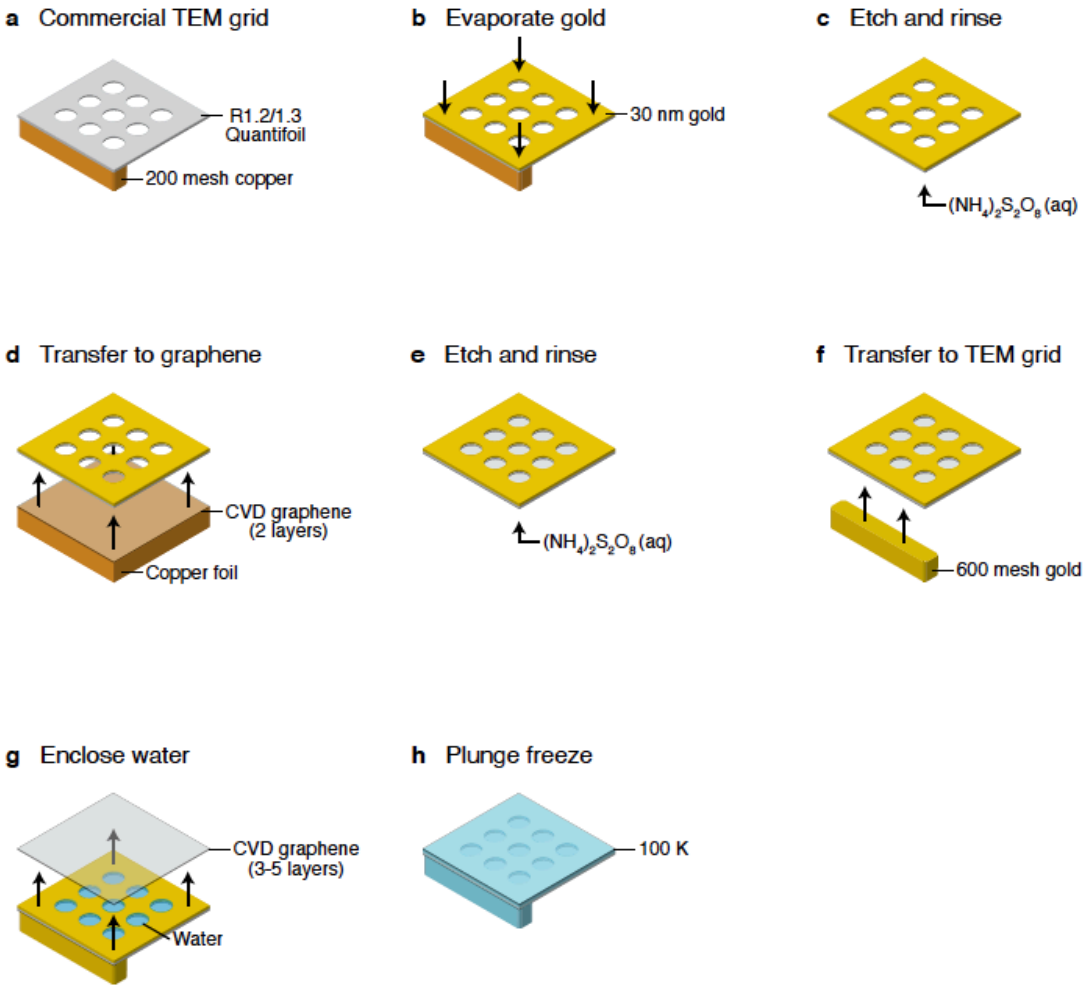

Fig. S1. Sample preparation workflow for graphene-enclosed cryo samples. (a,b) A Quantifoil TEM grid is coated with gold. (c) The copper mesh of the TEM grid is etched away and the gold film is rinsed. (d) The film is placed onto bilayer graphene on copper foil. (e) The copper foil is etched away and the film is rinsed. (f) The film is transferred onto a gold TEM grid and (g) water is enclosed with graphene. (h) The assembly is plunge frozen.

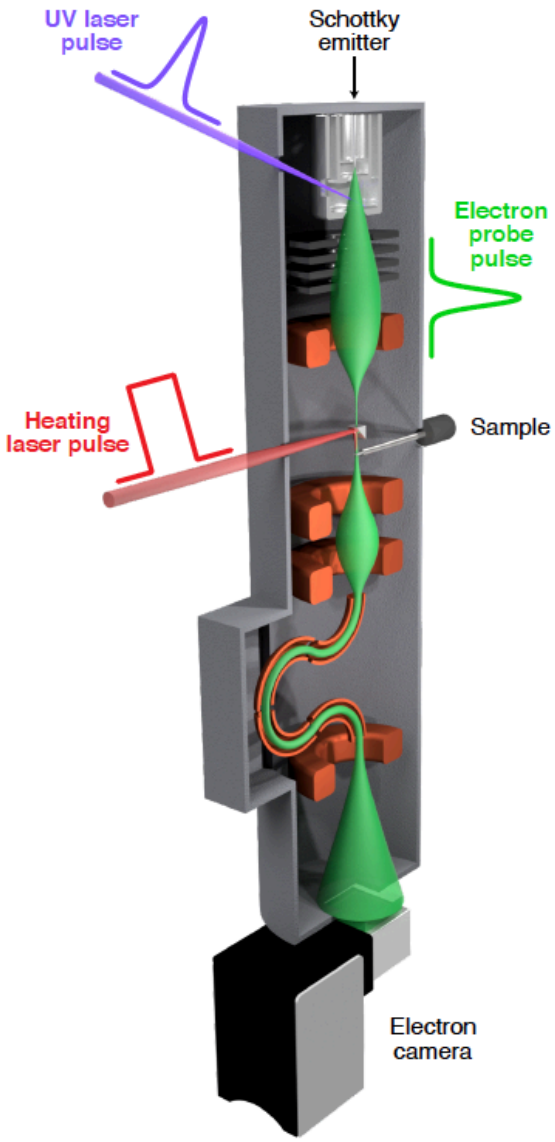

Fig. S2. Sketch of the modified transmission electron microscope. The sample is heated in situ with a laser pulse of tens of microseconds duration, obtained by chopping the output of a continuous laser with an acousto-optic modulator. In the stroboscopic experiments characterizing the temperature evolution of the sample (Fig. 4 of the main text and Fig. S4), electron probe pulses are generated by illuminating the Schottky emitter of the microscope with a UV laser pulse.

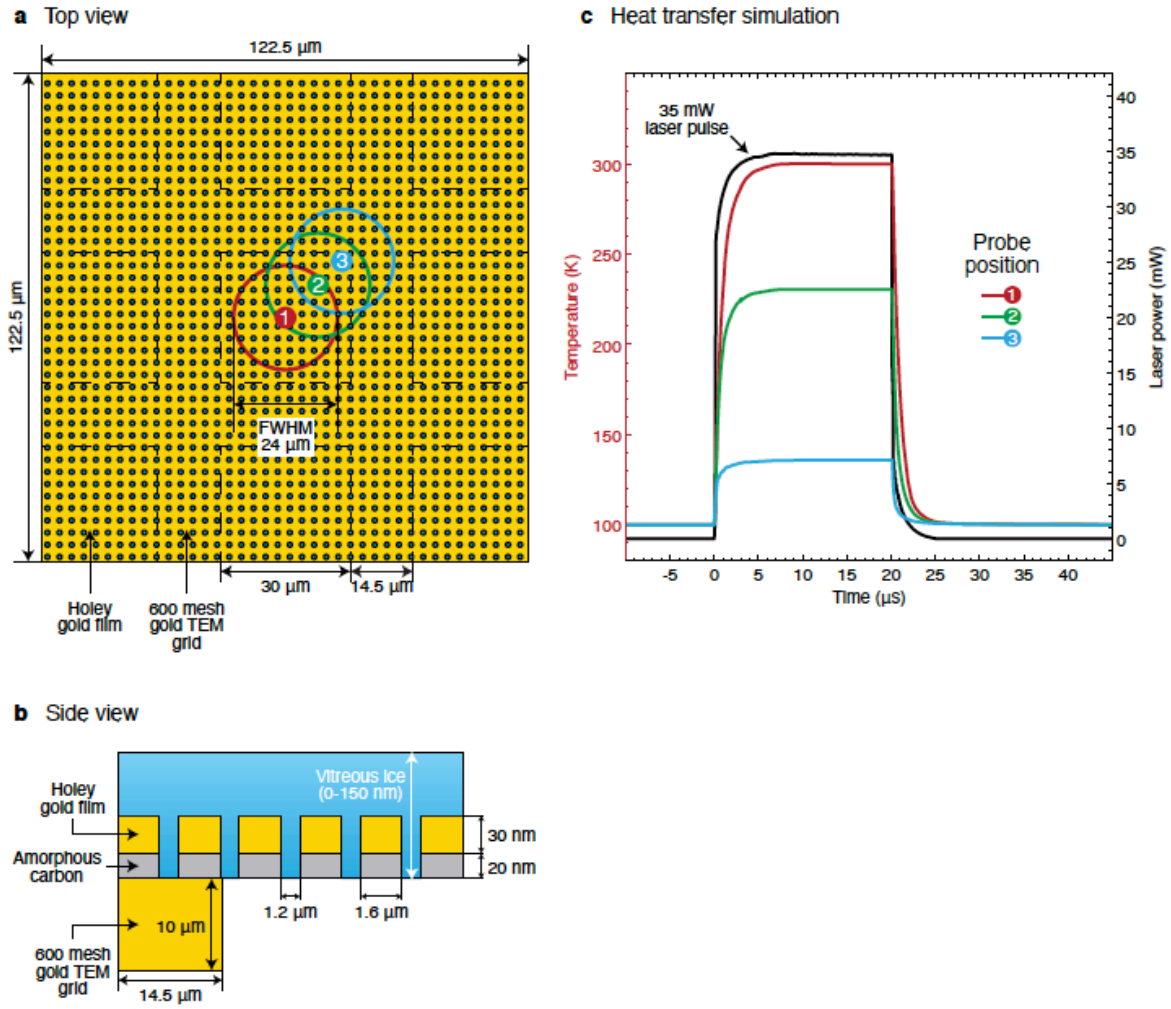

Fig. S3. Heat transfer simulations. (a,b) Top and side view of the simulated geometry, respectively. The empty circles mark the position of the laser focus, and the dots mark the regions probed in the corresponding simulation. (c) Temporal profile of the laser pulse (black curve) and temperature evolution of the gold film. While the magnitude of the temperature jump depends on the distance to the grid bars, the heating and cooling times (~1 µs) are largely unchanged.

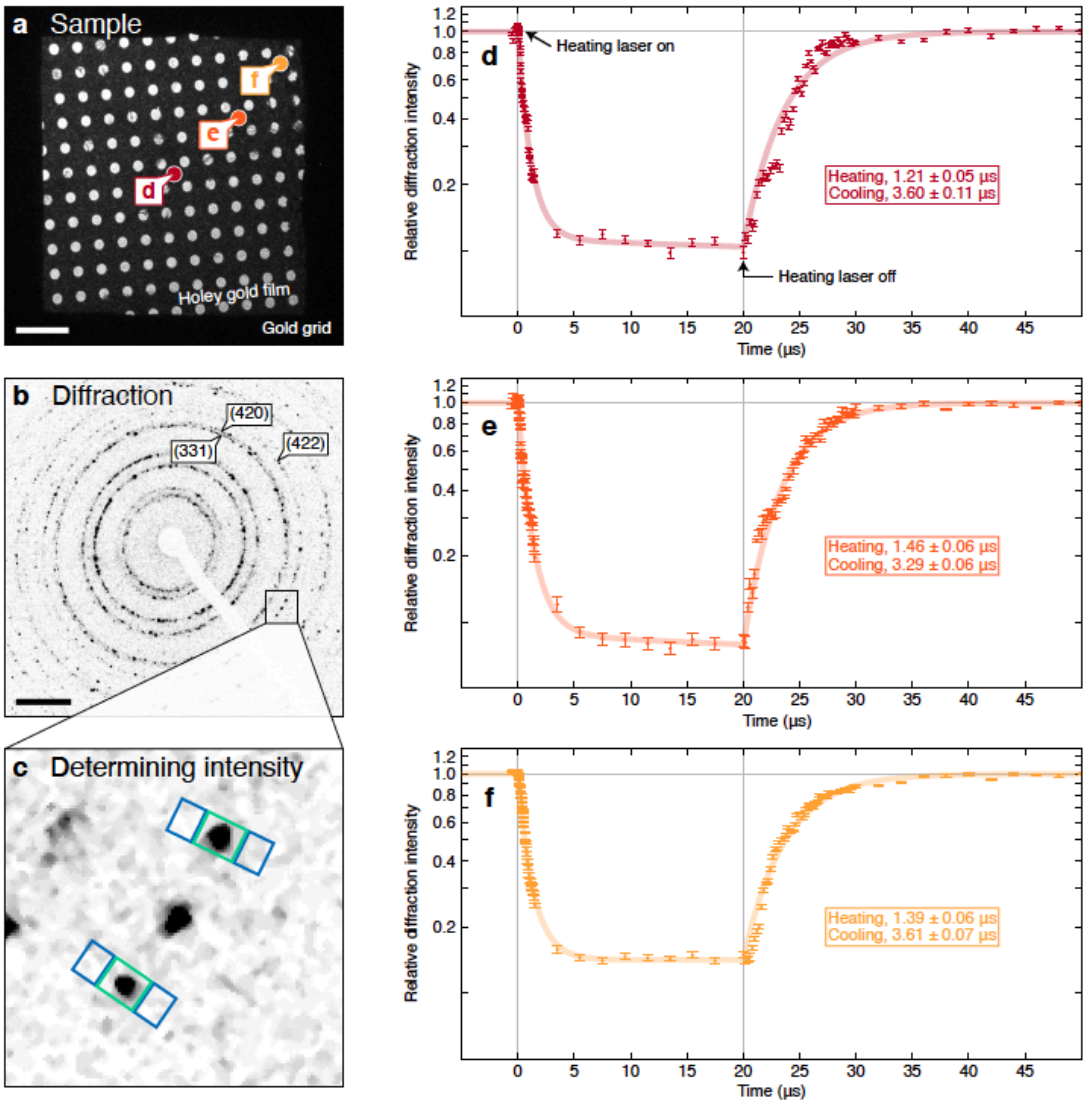

Fig. S4. Characterization of the temperature evolution of the sample under illumination with microsecond laser pulses. (a) Micrograph of the sample in a region that is free of ice. The dots mark the selected areas from which diffraction patterns were acquired and onto which the laser was focused. Scale bar, 5 µm. (b) Selected area diffraction pattern of the area marked with a red dot in (a). Scale bar, 5 nm-1. (c) The intensities of diffraction spots are determined by integrating a rectangular region of interest around the diffraction spot (green boxes) and subtracting the intensity of the diffraction background, as determined from the average intensity of the areas marked with blue boxes. (d–f) Temporal evolution of the diffraction intensity at the sample positions marked in (a). Heating and cooling times indicated in the figure are determined from fits with exponential functions (solid lines, see Note S7). The error bars represent the standard error.

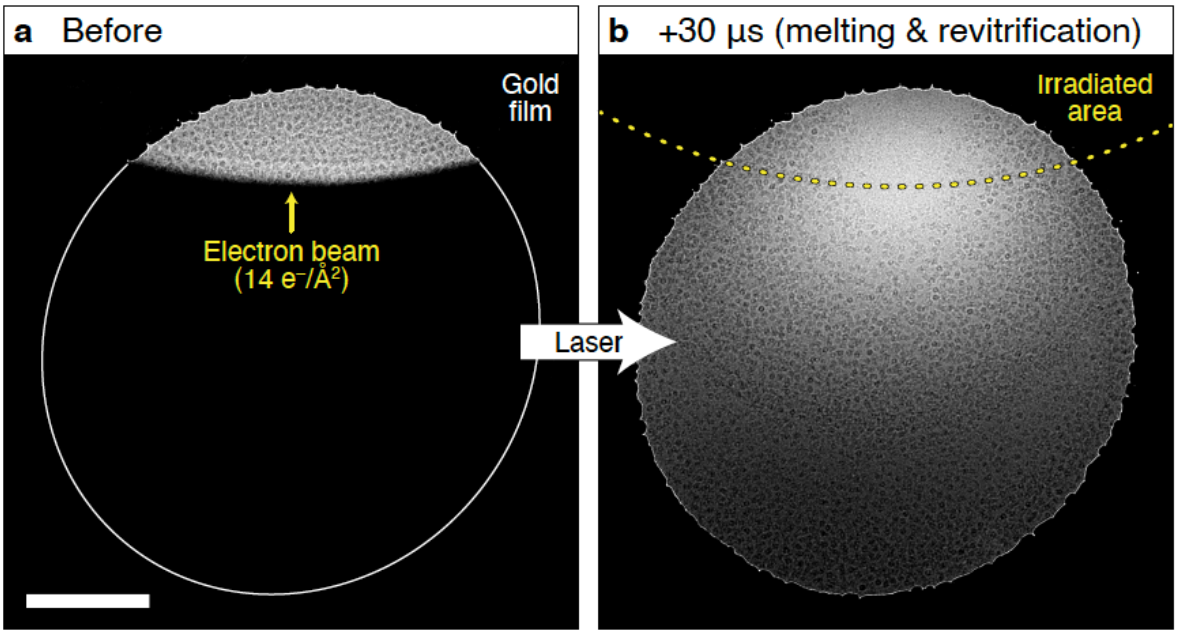

Fig. S5. Microsecond time-resolved cryo-EM of the rapid disassembly of GroEL following electron beam damage. (a) Micrograph of a vitrified sample of GroEL on a holey gold film. Only the top portion of the sample is irradiated with the electron beam (14 electrons/Å2) in order to limit beam damage to particles in that area. The line sketches the outline of the hole of the gold film. (b) The sample is melted with a 30 µs laser pulse in situ, allowing the damaged GroEL particles to unravel. Following the laser pulse, the sample revitrifies, trapping particles in their transient configurations. The dashed line marks the sample area that was irradiated in (a). Unlike in Fig. 5b of the main text, intact particles can be seen in the irradiated area. Moreover, the particle density is depleted beyond the region that was damaged by the electron beam. This suggests that convection has redistributed the particles. Scale bar, 300 nm.

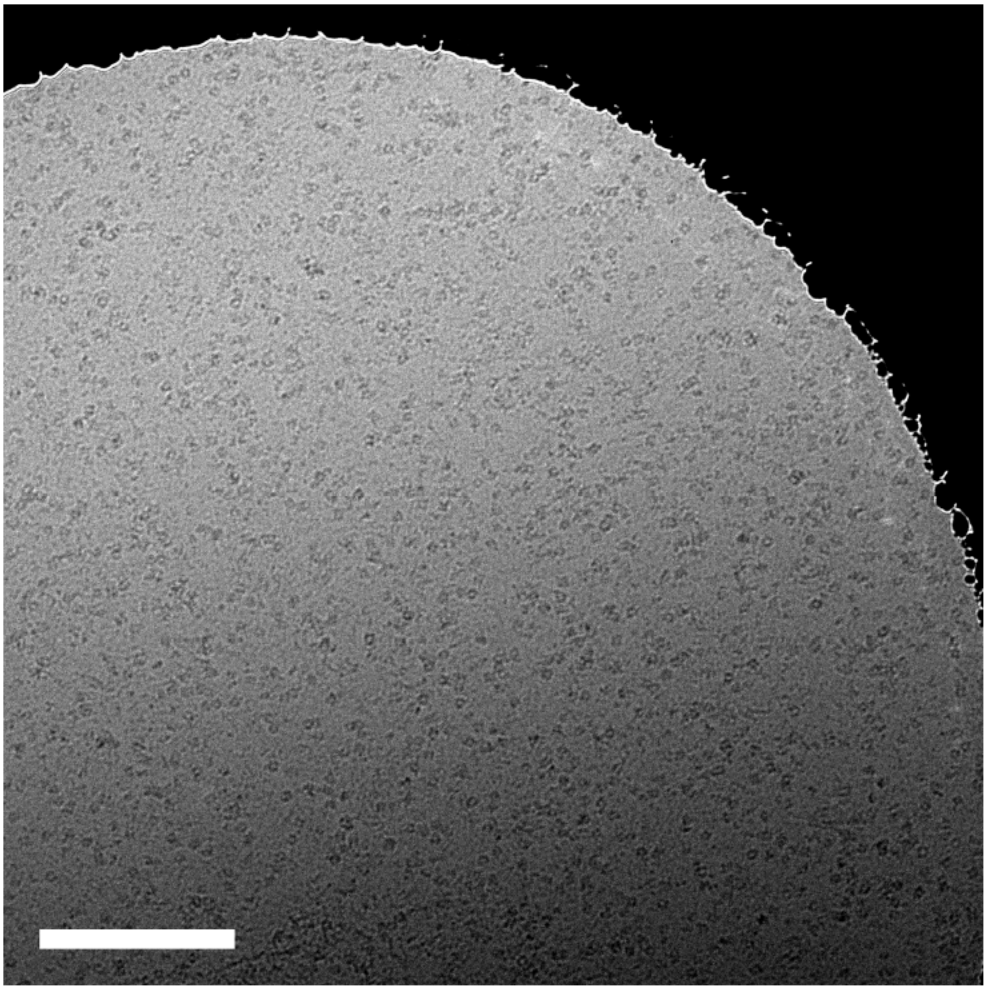

Fig. S6. GroEL particles in the hole adjacent to the area shown in Fig. 5c,d. The micrograph shows GroEL particles in a neighboring hole, which had not been irradiated by the electron beam in Fig. 5c. Despite being exposed to a near-identical laser intensity and reaching a similar temperature, the particles in this hole are still intact, indicating that the dynamics observed in Fig. 5d are not the result of laser irradiation. Scale bar, 250 nm.

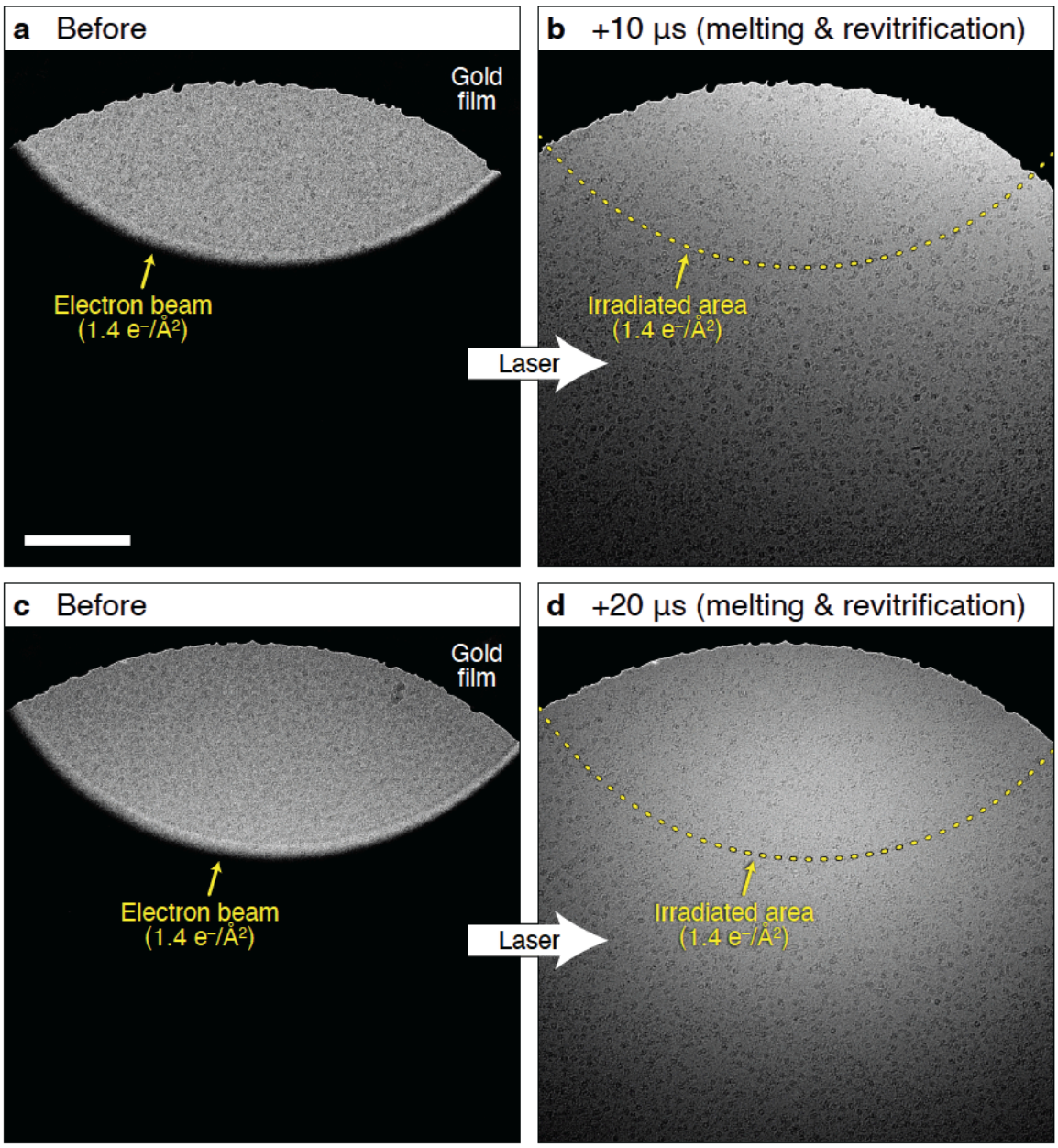

Fig. S7. Microsecond time-resolved cryo-EM of the rapid disassembly of GroEL following electron beam damage. (a) Micrograph of a vitrified sample of GroEL on a holey gold film. Only the top portion of the sample is irradiated with the electron beam (1.4 electrons/Å2) in order to limit beam damage to particles in that area. (b) The sample is melted with a 10 µs laser pulse in situ, allowing the damaged GroEL particles to unravel. Following the laser pulse, the sample revitrifies, trapping particles in their transient configurations. The dashed line marks the sample area that was irradiated in (a). (c,d) The experiment in (a,b) is repeated with a 20 µs laser pulse. Scale bar, 250 nm.

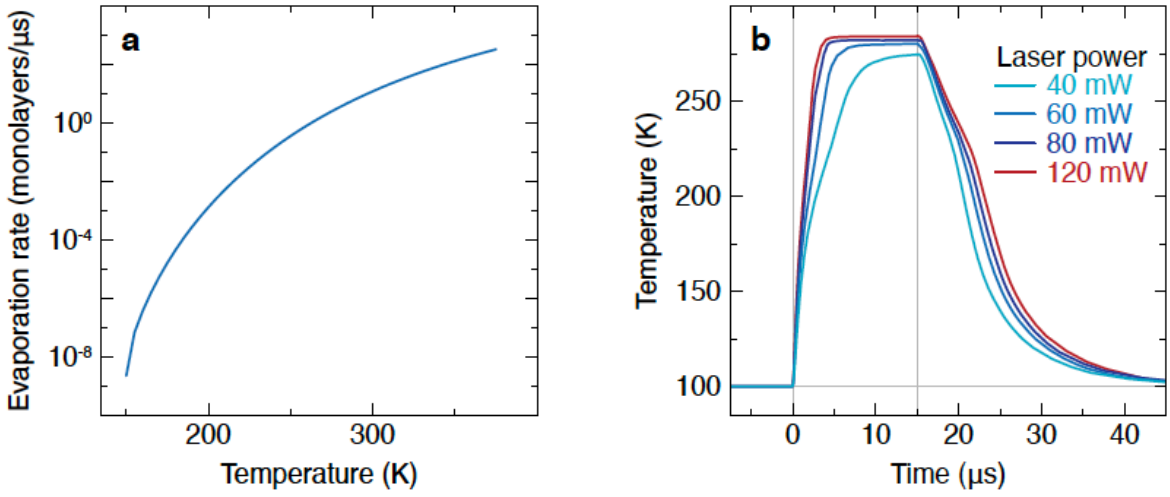

Fig. S8. Simulations of the temperature evolution in the experiments in Fig. 5. (a) Temperature-dependent evaporation rate of water.[16 17] (b) Simulated temperature evolution of an ice film heated by a 15 µs laser pulse of different laser powers with evaporative cooling of the sample included.

A1.3 References

1. P.K. Olshin, M. Drabbels, U.J. Lorenz, Characterization of a time-resolved electron microscope with a Schottky field emission gun, Struct. Dyn. 7 (2020) 054304.

2. A.A. Balandin, Thermal properties of graphene and nanostructured carbon materials, Nat. Mater. 10 (2011) 569–581.

3. J.W. Arblaster, Thermodynamic properties of gold, J. Phase Equilibria Diffus. 37 (2016) 229–245.

4. A.J. Bullen, K.E. O'Hara, D.G. Cahill, O. Monteiro, A. von Keudell, Thermal conductivity of amorphous carbon thin films, J. Appl. Phys. 88 (2000) 6317–6320.

5. S.R.P. Silva, Properties of Amorphous Carbon, INSPEC, The Institution of Electrical Engineers, London, 2003.

6. C. Moelle, M. Werner, F. Szücs, D. Wittorf, M. Sellschopp, J. von Borany, H.-J. Fecht, C. Johnston, Specific heat of single-, poly- and nanocrystalline diamond, Diam. Relat. Mater. 7 (1998) 499–503.

7. W. DeSorbo, W.W. Tyler, The specific heat of graphite from 13° to 300°K, J. Chem. Phys. 21 (1953) 1660–1663.

8. K. Murata, H. Tanaka, Liquid–liquid transition without macroscopic phase separation in a water–glycerol mixture, Nat. Mater. 11 (2012) 436–443.1

9. J.A. Sellberg, C. Huang, T.A. McQueen, N.D. Loh, H. Laksmono, D. Schlesinger, R.G. Sierra, D. Nordlund, C.Y. Hampton, D. Starodub, D.P. DePonte, M. Beye, C. Chen, A.V. Martin, A. Barty, K.T. Wikfeldt, T.M. Weiss, C. Caronna, J. Feldkamp, L.B. Skinner, M.M. Seibert, M. Messerschmidt, G.J. Williams, S. Boutet, L.G.M. Pettersson, M.J. Bogan, A. Nilsson, Ultrafast x-ray probing of water structure below the homogeneous ice nucleation temperature, Nature. 510 (2014) 381–384.

10. S. Maruyama, K. Wakabayashi, M. Oguni, Thermal properties of supercooled water confined within silica gel pores, AIP Conf. Proc. 708 (2004) 675–676.

11. O. Andersson, H. Suga, Thermal conductivity of low-density amorphous ice, Solid State Commun. 91 (1994) 985–988.

12. D.I. Yakubovsky, A.V. Arsenin, Y.V. Stebunov, D.Yu. Fedyanin, V.S. Volkov, Optical constants and structural properties of thin gold films, Opt. Express. 25 (2017) 25574–25587.

13. J.W. Weber, V.E. Calado, M.C.M. van de Sanden, Optical constants of graphene measured by spectroscopic ellipsometry, Appl. Phys. Lett. 97 (2010) 091904.

14. K.R. Pyun, K.D. Kihm, S. Cheon, H.G. Kim, W. Lee, G. Lim, W. Lee, S. Kim, M. Han, S.H. Ko, Interfacial thermal contact conductance inside the graphene–Bi2Te3 heterostructure, Adv. Mater. Interfaces. 6 (2019) 1900275.

15. M. Fuchs, E. Dayan, E. Presnov, Evaporative cooling of a ventilated greenhouse rose crop, Agric. For. Meteorol. 138 (2006) 203–215.

16. J.D. Smith, C.D. Cappa, W.S. Drisdell, R.C. Cohen, R.J. Saykally, Raman thermometry measurements of free evaporation from liquid water droplets, J. Am. Chem. Soc. 128 (2006) 12892–12898.

17. R.J. List, ed., Smithsonian Meteorological Tables, Smithsonian Institution Press, Washington, 1968.

18. A.H. Zewail, Four-dimensional electron microscopy, Science. 328 (2010) 187–193.

19. B.E. Warren, X-Ray Diffraction, Dover Publications, New York, 1990.

Appendix II – Supporting Information for Chapter 4

A2.1 Notes

Note S1. Experimental details.

All experiments were performed using a modified JEOL 2200FS transmission electron microscope operating at 160 kV accelerating voltage (Figure S1), which has been described previously.[1] To initiate melting and revitrification, the cryo sample is heated *in situ* with a 532 nm laser pulse of tens of microseconds duration. The laser pulse is obtained by chopping the output of a continuous laser with an acousto-optic modulator. The laser beam is directed to the sample by a mirror located above the upper pole piece of the objective lens, striking the sample at close to normal incidence. A 25 cm lens focuses the laser beam to a spot size of 24±1 μm FWHM, as measured by a knife edge scan in the sample plane. In all experiments, the laser beam is centered on the area under observation. We note that the laser radiation is not absorbed by either the proteins or the vitreous ice film, but only by the holey gold film of the specimen grid, which acts as the heat source for melting the cryo sample.

Cryo samples were prepared on Quantifoil UltrAuFoil TEM grids (R2/2 holey gold film with 50 nm thickness on 200 mesh gold) using solutions of apoferritin (EMD Millipore Corp, Figure 1,2) and GroEL (Takara Bio Europe SAS, Figure 3,6). The grids were plasma cleaned using an ELMO glow discharge system operating with negative head polarity, 0.8 mA plasma current, and 0.2 mBar residual air pressure. After plasma cleaning, approximately 3 μL of either the apoferritin or GroEL solution was placed on the grids. The grids were then inserted into a Vitrobot MarkIV (Thermo Fisher Scientific) held at 100% relative humidity and 22 °C. The grids were blotted with 595 filter paper for 2.5 seconds with a blotting force of -15 and were immediately vitrified by plunge-freezing in liquid ethane.

Note S2. Estimation of crystallization times for supercooled water.

The crystallization time of supercooled water τ_x was estimated according to

$$\tau_x = \left(\frac{3\phi}{\pi I_N \mu_G{}^3}\right)^{\frac{1}{4}}$$ References 2,3

Here, I_N is the nucleation rate, μ_G the growth rate, and ϕ the volume fraction that has crystallized, which we have set to $\phi = 0.5$, so that τ_x represents the time for half the sample to crystallize. Nucleation[4] and growth rates[5] were taken from the literature. As shown in Figure S3, the experimental data were splined, and the crystallization time τ_x shown in Figure 4 was then calculated from these splines.

Note S3. Heat transfer simulations.

Finite element heat transfer simulations of the temperature evolution of the sample under illumination with microsecond laser pulses were performed using COMSOL Multiphysics. A top view of the simulation geometry is given in Figure S4a. A 200 mesh gold TEM grid (38.5 μm wide and 15 μm thick bars, 86.8 μm x 86.8 μm viewing area) supports a gold film (50 nm thickness). The gold film features a pattern of regularly spaced holes (1 or 2 μm diameter, 4 μm pitch) and is covered by a thin layer of vitreous ice (160 nm thickness). The simulation area is limited to a square of 190 μm side length (red box in Figure S4a). The grid bars extend 405 μm past the simulation area in each direction in order to account for the large heat capacity of the specimen grid.

The simulation geometry for a cryo sample on a holey gold film (blue and yellow curves in Figure 5c,d, all curves in Figure S5c, and blue and yellow curves in Figure S5d) is shown in Figure S4b. Evaporation is simulated to occur from both surfaces of the water film (see details below), as is the case in our experiments.

For samples in which multilayer graphene has been added on top of the holey gold film (red curve in Figure 5c and red curve in Figure S5d), we use the geometry depicted in Figure S4c. Here, the ice rests on the top of the holey gold film, so that evaporation can only occur from the top surface of the water film. To reduce computational costs, we only simulate a small portion of the graphene sheet (10 μm x 10 μm square, 2.5 nm thick, ~8 layers, centered on the four central holes of the gold film).

We use literature values for the temperature-dependent heat capacity and thermal conductivity of gold[6,7] and graphene.[8,9] Experimental values of the heat capacity and thermal conductivity of supercooled water are unavailable for a range of temperatures known as "no man's land."[10,11] We therefore use the heat capacity of supercooled water in silica nanopores, which is available for the entire temperature range.[12] For the thermal conductivity of water, we use its room temperature value, which is similar to that of amorphous ice at low temperatures.[13]

The entire sample is set to an initial temperature of 100 K. We simulate heating with a 10 μs laser pulse by placing a Gaussian heat source (24 μm FWHM) on the top surface of the gold film in the center of the simulation area (green circle in Figure S4a). For samples in which graphene has been added on top of the holey gold film, the heat source is placed on the bottom surface of the water film and on the top surface of the graphene. The heating rate during irradiation with a 10 μs square heating laser pulse is calculated from the incident laser power and the absorption of the gold[14] and graphene films.[15] The lowest laser power used in the simulations (46 mW) is chosen to replicate the experimental conditions in Figure 3 of the main text. We note that the simulation reproduces the experimental observation that only the ice in the four central holes is melted and revitrified (see Figure 3b and Figure 5b).

To account for evaporative cooling in the simulations, we apply a negative heat source to the top surface (Figure S4c) or the top and bottom surfaces (Figure S4b) of the water film, depending on the simulated geometry. The cooling rate is determined from the temperature-dependent enthalpy of evaporation[16] and the temperature-dependent evaporation rate[17] (Figure S6) of water, which we calculate from literature values of the vapor pressure[18] assuming an evaporation coefficient of $\gamma = 0.62$ (Reference 17).

A2.2 Table

Table S1. Parameters for heat transfer simulations.

Property	Value	Reference
Heat capacity of gold	$38.5679 + 1.2434 \cdot T - 7.137 \cdot 10^{-3} \cdot T^2 + 1.9237 \cdot 10^{-5} \cdot T^3 - 1.9801 \cdot 10^{-8} \cdot T^4$ (J/kg·K)	6
Thermal conductivity of gold	$320.973 - 0.0111 \cdot T - 2.747 \cdot 10^{-5} \cdot T^2 - 4.048 \cdot 10^{-9} \cdot T^3$ (W/m·K)	7
Heat capacity of graphene	Data from Table 2 of Ref. 8	8
Thermal conductivity of graphene	Data for supported graphene from Figure 3a of Ref. 9	9
Heat capacity of water	Data from Figure 2 of Ref. 12	12
Thermal conductivity of water	0.6 W/(m·K)	13
Absorption of gold	25% at 532 nm	14
Absorption of graphene	~1% per monolayer at 532 nm = 8% total	15
Enthalpy of evaporation of water	$2.498 \cdot 10^6 - 3.369 \cdot 10^3 \cdot T$ (J/kg)	16
Evaporation rate	Equation 2 with g = 0.62	17
Vapor pressure of water	Page 350, Equation 1 of Ref. 18	18

A2.3 Figures

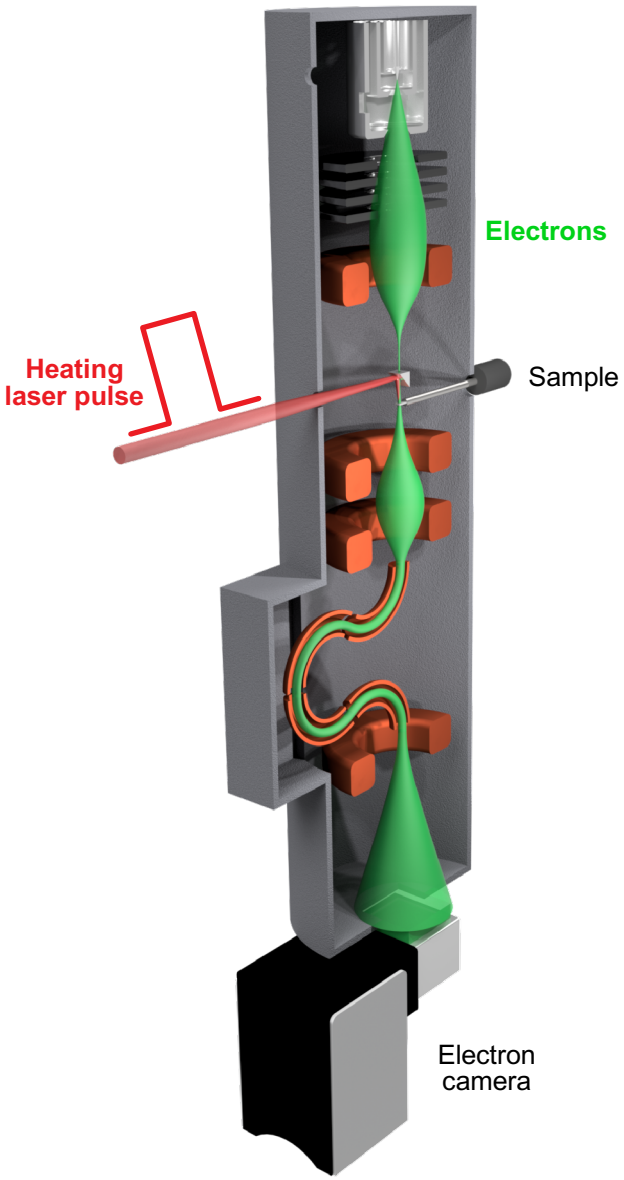

Figure S1. Modified transmission electron microscope used for microsecond *in situ* cryo-EM experiments. The sample is heated *in situ* by a laser pulse (532 nm, spot size of 24±1 μm FWHM in the sample plane) with a duration of tens of microseconds, which is obtained by chopping the output of a continuous laser with an acousto-optic modulator. The laser beam is directed onto the sample by an aluminum mirror, which is mounted above the upper pole piece of the objective lens, so that the laser beam strikes the sample at close to normal incidence.[1]

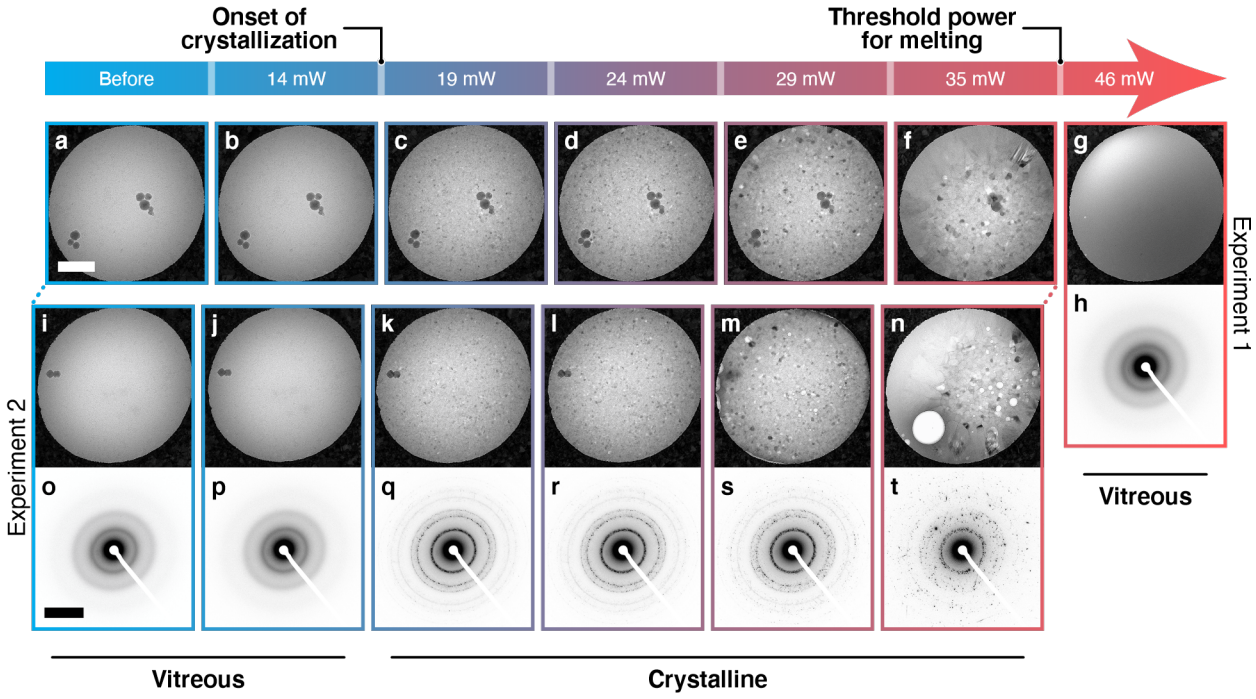

Figure S2. Phase behavior of cryo samples heated with laser pulses of increasing power. (**a**–**g**)

Micrographs of an apoferritin cryo sample under exposure to laser pulses of increasing power. The sample (a) remains vitreous after heating with a 10 µs laser pulse of 14 mW power (b), but crystallizes at a power of 19 mW (c). (d–f) The crystal morphology changes as the power is increased in steps to 35 mW. (g) A single pulse of 46 mW power melts the sample, causing it to revitrify when it cools after the end of the laser pulse. (h) Diffraction pattern of the revitrified sample in (g). (i–n) Micrographs and (o–t) diffraction patterns of a second identical cryo sample, recorded after heating with pulses of the same laser powers as above. We note that due to the prolonged exposure, electron beam damage has caused the formation of holes in the ice film in (m) and (n). Scale bars, 500 nm and 5 nm^{-1}.

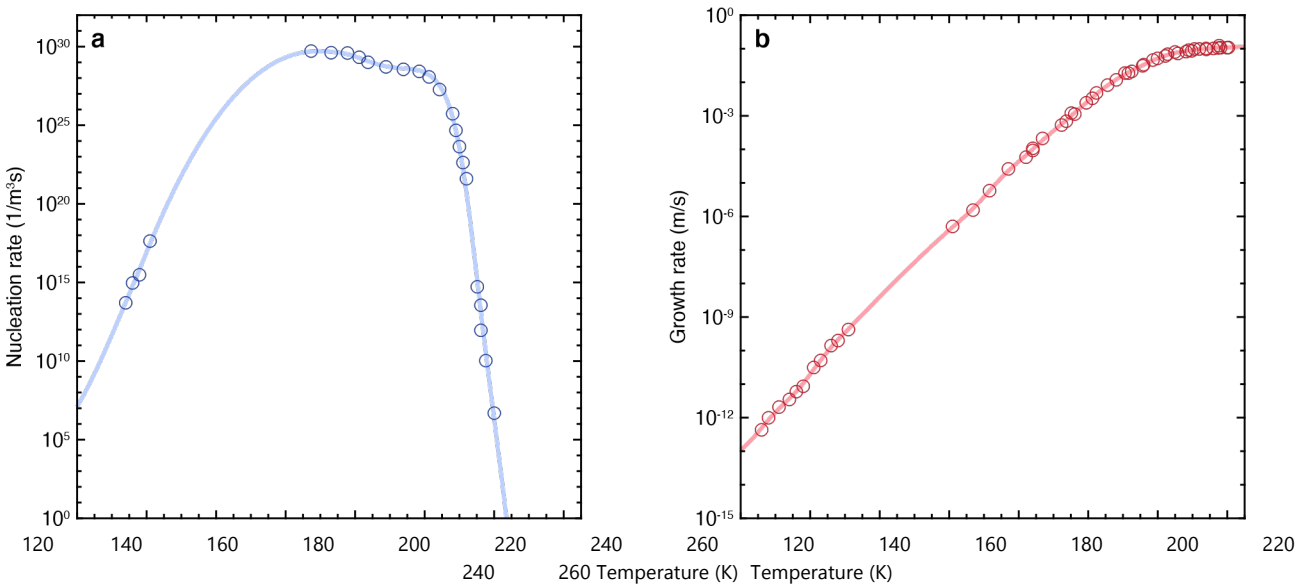

Figure S3. Nucleation and growth rates of ice. (a) Experimental nucleation rates are taken from Figure 5 of Reference 4. (b) Experimental growth rates are taken from Figure 3 of Reference 5. The solid lines are splines of the experimental data and are used to estimate the crystallization time $\tau_!$ in Figure 4 of the main text.

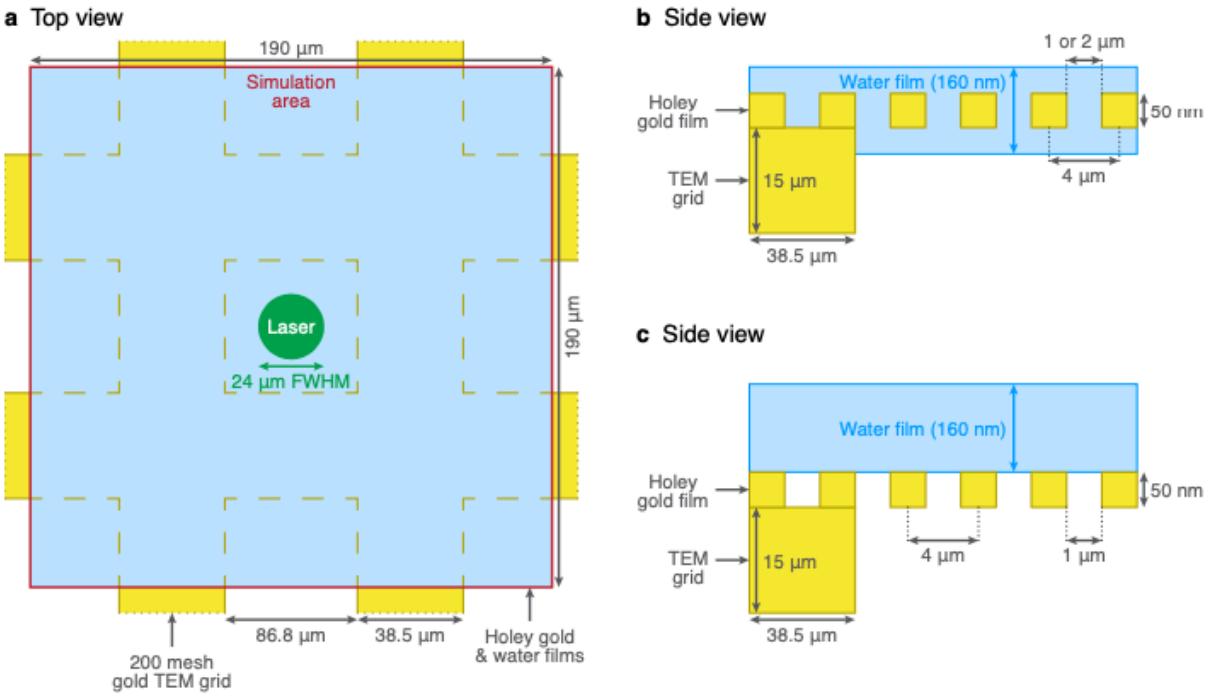

Figure S4. Sample geometries for heat transfer simulations. (a) Top view of the simulation geometry. Simulations are carried out in the area marked by the red box. The green circle marks the position of the Gaussian laser beam, which has a spot size of 24 µm FWHM. (b) Side view of the simulation geometry with the holey gold film covered on both sides with water. Evaporation occurs from both the top and bottom surface of the water film. (c) Side view of the simulation geometry for samples in which multilayer graphene is added on top of the holey gold film. Evaporation occurs only from the top surface of the water film, since its bottom surface is covered by graphene.

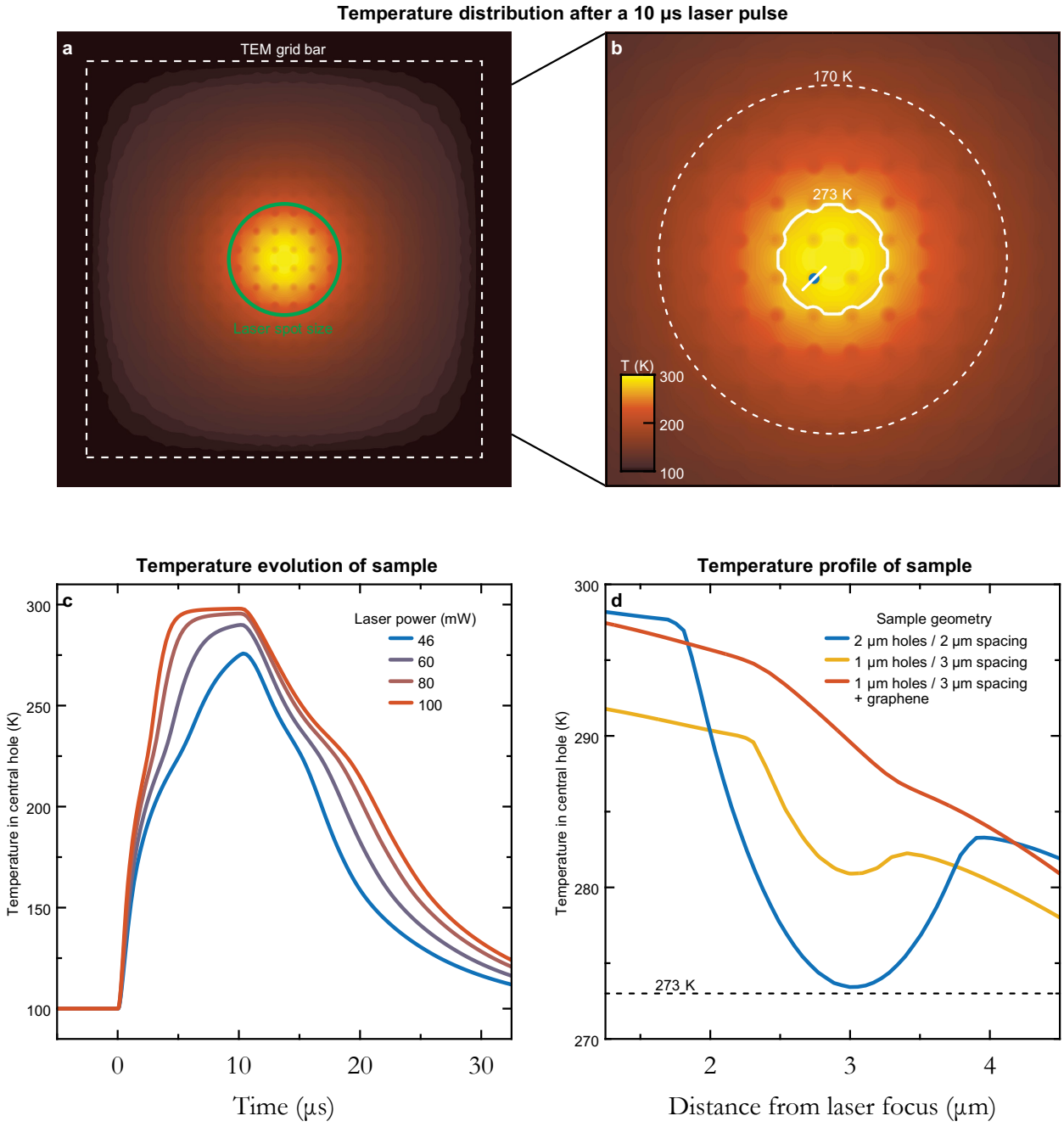

Figure S5. Heat transfer simulations of a melting and revitrification experiment. (a,b) Temperature distribution of a cryo sample after irradiation with a 10 µs laser pulse (46 mW, 24 µm spot size, indicated with a green circle). Scale bar, 10 µm. The white line in (b) indicates the isotherm at 273 K and the dashed circle represents the boundary of the crystalline region from the experiment in Figure 3b, at which the simulation predicts a temperature of 170 K. (c) Temperature evolution of the cryo sample (at the position of the blue dot in (b)) for different laser powers. The experimental laser power of 46 mW just barely heats the ice above 273 K. While higher laser powers heat the sample more rapidly, the temperature to which

the water film plateaus increases only gradually. We note that due to the larger spacing of the TEM grid bars used here, which act as a heat sink, the cooling rate (~10^7 K/s) is slightly lower than that previously reported.[19] (d) Temperature profiles across a central hole in the gold film (white line in (b)) at the end of a 10 μs laser pulse (46 mW) for different sample geometries. Due to its low heat conductivity, a temperature gradient forms in the water that is supported by the holey gold film with 2 μm diameter holes (blue curve). The gradients are less pronounced for a gold film with 1 μm diameter holes (yellow curve) and are absent when a layer of graphene is placed between the water and gold (red curve).

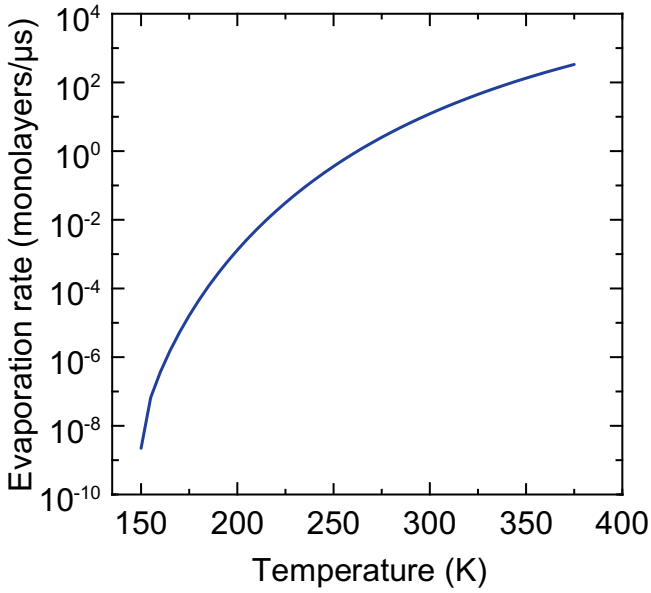

Figure S6. Temperature-dependent evaporation rate of water. The temperature-dependent evaporation rate of water is calculated using literature values of the vapor pressure[18] assuming an evaporation coefficient of $\gamma = 0.62$ (Reference 17).

A2.4 References

1. P. K. Olshin, M. Drabbels and U. J. Lorenz, Characterization of a time-resolved electron microscope with a Schottky field emission gun, Structural Dynamics, 2020, 7, 054304. B.E. Warren, X-Ray Diffraction, Dover Publications, New York, 1990.

2. P. G. Debenedetti, Metastable Liquids: Concepts and Principles, Princeton University Press, Princeton, 1997. B.E. Warren, X-Ray Diffraction, Dover Publications, New York, 1990.

3. H. Tanaka, Possible resolution of the Kauzmann paradox in supercooled liquids, Phys. Rev. E, 2003, 68, 011505. B.E. Warren, X-Ray Diffraction, Dover Publications, New York, 1990.

4. A. J. Amaya and B. E. Wyslouzil, Ice nucleation rates near 225 K, J. Chem. Phys., 2018, 148, 084501.

5. Y. Xu, N. G. Petrik, R. S. Smith, B. D. Kay and G. A. Kimmel, Growth rate of crystalline ice and the diffusivity of supercooled water from 126 to 262 K, Proc Natl Acad Sci USA, 2016, 113, 14921–14925. B.E. Warren, X-Ray Diffraction, Dover Publications, New York, 1990.

6. J. W. Arblaster, Thermodynamic properties of gold, J. Phase Equilib. Diffus., 2016, 37, 229–245.

7. J. Huang, Y. Zhang and J. K. Chen, Ultrafast solid–liquid–vapor phase change of a gold film induced by pico- to femtosecond lasers, Applied Physics A, 2009, 95, 643–653. B.E. Warren, X-Ray Diffraction, Dover Publications, New York, 1990.

8. W. DeSorbo and W. W. Tyler, The specific heat of graphite from 13° to 300°K, The Journal of Chemical Physics, 1953, 21, 1660–1663

9. E. Pop, V. Varshney and A. K. Roy, Thermal properties of graphene: Fundamentals and applications, MRS Bulletin, 2012, 37, 1273–1281. B.E. Warren, X-Ray Diffraction, Dover Publications, New York, 1990.

10. K. Murata and H. Tanaka, Liquid–liquid transition without macroscopic phase separation in a water– glycerol mixture, Nature Mater, 2012, 11, 436–443. B.E. Warren, X-Ray Diffraction, Dover Publications, New York, 1990.

11. J. A. Sellberg, C. Huang, T. A. McQueen, N. D. Loh, H. Laksmono, D. Schlesinger, R. G. Sierra, D. Nordlund, C. Y. Hampton, D. Starodub, D. P. DePonte, M. Beye, C. Chen, A. V. Martin, A. Barty, K. T. Wikfeldt, T. M. Weiss, C. Caronna, J. Feldkamp, L. B. Skinner, M. M. Seibert, M. Messerschmidt, G. J. Williams, S. Boutet, L. G. M. Pettersson, M. J. Bogan and A. Nilsson, Ultrafast x-ray probing of water structure below the homogeneous ice nucleation temperature, Nature, 2014, 510, 381–384.

12. S. Maruyama, K. Wakabayashi and M. Oguni, Thermal properties of supercooled water confined within silica gel pores, AIP Conference Proceedings, 2004, 708, 675–676.

13. O. Andersson and H. Suga, Thermal conductivity of low-density amorphous ice, Solid State Commun., 1994, 91, 985–988.

14. D. I. Yakubovsky, A. V. Arsenin, Y. V. Stebunov, D. Y. Fedyanin and V. S. Volkov, Optical constants and structural properties of thin gold films, Opt. Express, OE, 2017, 25, 25574–25587.

15. J. W. Weber, V. E. Calado and M. C. M. van de Sanden, Optical constants of graphene measured by spectroscopic ellipsometry, Applied Physics Letters, 2010, 97, 091904.

16. M. Fuchs, E. Dayan and E. Presnov, Evaporative cooling of a ventilated greenhouse rose crop, Agricultural and Forest Meteorology, 2006, 138, 203–215.

17. J. D. Smith, C. D. Cappa, W. S. Drisdell, R. C. Cohen and R. J. Saykally, Raman thermometry measurements of free evaporation from liquid water droplets, J. Am. Chem. Soc., 2006, 128, 12892– 12898.

18. R. J. List, Ed., Smithsonian Meteorological Tables, Smithsonian Institution Press, Washington, 1968.

19. J. M. Voss, O. F. Harder, P. K. Olshin, M. Drabbels and U. J. Lorenz, Rapid melting and revitrification as an approach to microsecond time-resolved cryo-electron microscopy, Chemical Physics Letters, 2021, 778, 138812.

Appendix III – Supporting Information for Chapter 5

A3.1 Figures

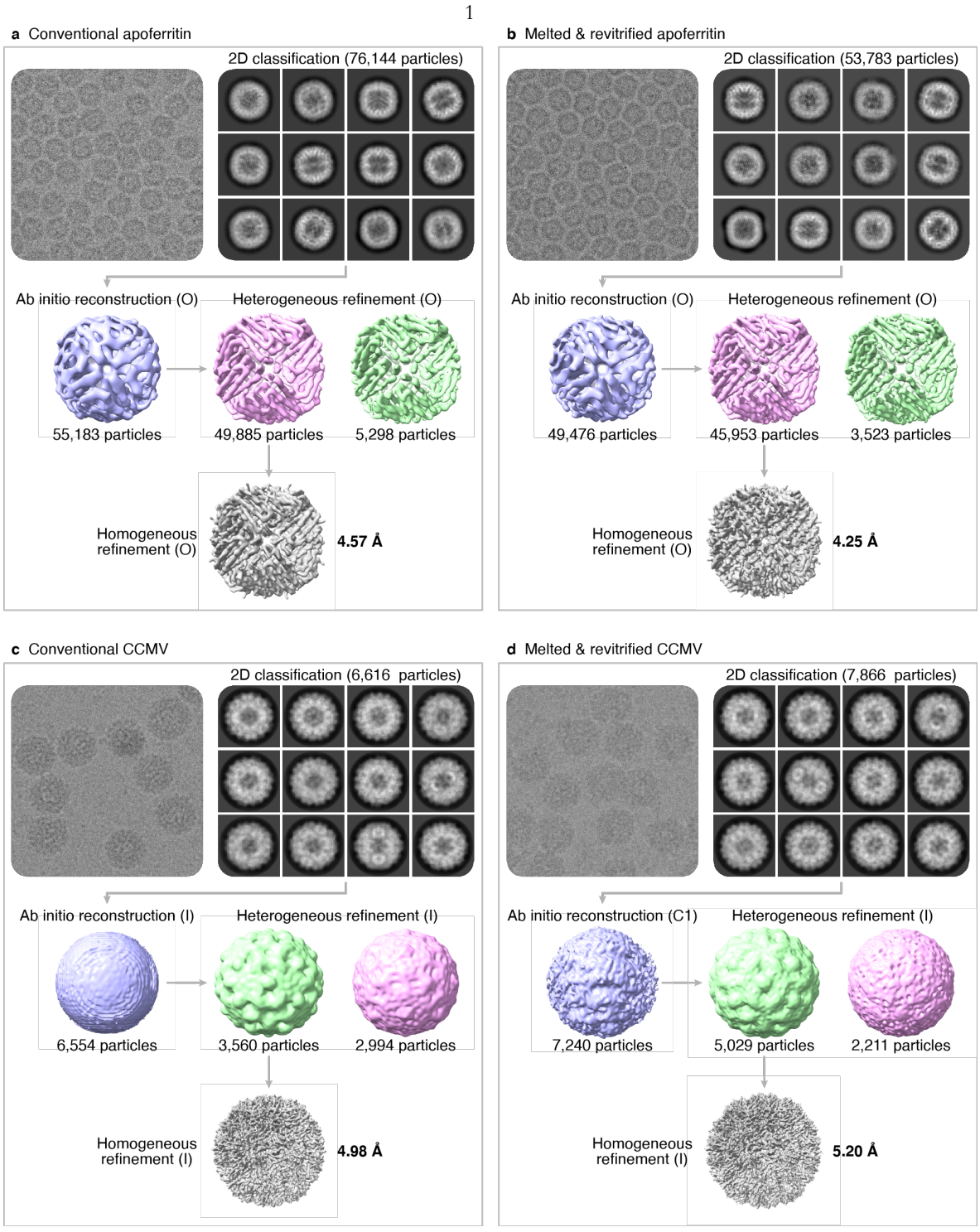

Figure S1. Workflows for single-particle reconstructions of apoferritin (a,b) and CCMV (c,d) from conventional and revitrified samples.

Appendix IV – Supporting Information for Chapter 6

A4.1 Notes

Experimental details.

A. Sample preparation

Cowpea chlorotic mottle virus was provided by the group of Prof. Jeroen Cornelissen at the University of Twente. Cryo samples of contracted CCMV (pH 5, free of divalent ions were prepared by applying 3 μl of the sample solution (11.5 mg/ml in 100 mM sodium acetate buffer, 1 mM sodium azide, 1 mM EDTA) to glow discharged UltrAuFoil grids (R1.2/1.3, 300 mesh, Quantifoil), which were plunge frozen with a Thermo Fisher Vitrobot Mark IV (10 °C, 95 % relative humidity, 3 s blotting time, blotting force of 10). Cryo samples of extended CCMV (pH 7.6) were prepared from the sample solution through buffer exchange with a centrifugal concentrator (MWCO 50 kDa, 10°C). The sample solution (23 mg/ml in 10 mM Tris buffer, 50 mM sodium chloride, 1mM EDTA) was then plunge frozen under the same conditions. For pH jump experiments, NPE-caged-proton (Bio-Techne, 120 mM) was added to this solution in a 1:6 volume ratio prior to plunge freezing.

In order to release the photoacid, cryo samples were placed in a Linkam cryo stage and irradiated with a nanosecond pulsed UV laser for 30 min (Bright Solutions Wedge, 266 nm, 35 mW, 7.1±0.1 mm FWHM spot size in the sample plane, as determined from a knife edge scan). The pH of the sample after release of the photoacid was determined as follows. A frozen droplet of the same sample solution (3 μl) was UV irradiated under identical conditions, after which the droplet was melted. A measurement with a pH strip yielded a pH of 4.5± 0.5.

In order to determine that UV irradiation does not cause contraction of the particles in the absence of a photoacid (Supplementary Fig. 2), cryo samples of extended CCMV (without photoacid) were irradiated under identical conditions.

B. In-situ revitrification

Revitrification experiments were performed *in situ* with a modified JEOL 2200FS transmission electron microscope as previously described.[1 2] Microsecond laser pulses for revitrification (532 nm wavelength, about 100 mW power) were obtained by chopping the output of a continuous laser (Laser Quantum, Ventus 532) with an acousto-optic modulator (AA Opto-Electronic). The laser beam was focused to a spot size of 28±2 μm FWHM in the sample plane, as determined from a knife edge scan. Sample areas were melted and revitrified with the laser beam centered onto a grid square. We estimate that both the melting and the revitrification process occur on a timescale of about 5-7 μs, as determined from heat transfer simulations, which we previously found to describe the experiment well.[2] Evaporation of the sample in the vacuum of the electron microscope reduces its thickness by several tens of nanometers, with the change in thickness depending on the exact sample thickness and plateau temperature reached. This number is likely smaller for the actual cryo samples used in our experiment, which contain buffer, photoacid, and proteins, all of which likely reduce the evaporation coefficient of the solution.

C. Data collection

Data were collected at the Dubochet Center for Imaging in Lausanne using a Titan Krios microscope equipped with Falcon IV detector and a SelectrisX energy filter. The data acquisition parameters for the different data sets are listed in supplementary table 1.

D. Single-particle reconstructions

Single-particle reconstructions were performed in CryoSPARC 4.0.1.[3] The following workflow was used, with details for the different data sets are provided in Supplementary Figs. 1 and 2. The micrographs were patch motion corrected, and movies with a total full-frame motion distance of more than 100 pixels were discarded. Contrast transfer function (CTF) estimation was performed using Patch CTF in CryoSPARC. Micrographs with an estimated resolution of less than 10 Å or an astigmatism of over 2000 Å were discarded, as well as micrographs containing hexagonal or cubic ice. Particles were picked using manual picking or blob picking, followed by template picking and were extracted with a box size of 768 pixels. Following 2D classification and *ab initio* reconstruction, the best classes resulting from heterogeneous refinement (Icosahedral symmetry) were further refined using homogeneous or non-uniform refinement

with Icosahedral symmetry imposed. Additional refinement steps included CTF refinement, per particle defocus refinement, and Ewald sphere correction. The global and local resolution was estimated using an gold-standard FSC threshold of 0.143. The structures were visualized with UCSF ChimeraX 1.5.[4,5] The reconstructions colored by local resolution, and the angular distribution of particles used in the final reconstructions are shown in Supplementary Fig. 3a–e and 3f–j, respectively.

E. Variability analysis

The variability analysis shown in Fig. 3e was performed on a combined dataset containing 21,675 refined particles each of the extended, partially contracted, and fully contracted CCMV. Three variability components and a low-pass filter resolution of 10 Å were used. In Fig. 3e, the particle distribution is shown as a function of the first two components. To analyze the motions of the capsid proteins during contraction, the particle distribution was divided into 30 equal slices along the first component, and each slice was homogeneously reconstructed with icosahedral symmetry imposed.

F. Model building

A model of contracted CCMV capsid was obtained with the following procedure. The model of contracted CCMV from PDB:1ZA7 [6] was protonated using the APBS-PDB2PQR software suite [7] with the pH set to 5 and rigidly fit into the auto-sharpened contracted CCMV map using UCSF ChimeraX 1.4.[4 5] The asymmetric unit was then iteratively refined using the real space refine tool in PHENIX 1.20.1-4487 [8], with secondary structure and non-crystallographic symmetry constraints imposed, and the ISOLDE plugin [9] in UCSF ChimeraX. The refinement was finalized using a map section containing the asymmetric unit as well as the chains in its proximity.

A model of the extended CCMV capsid was obtained with a similar procedure. The model of the contracted form obtained above was set to the protonation state at pH 7.6 and rigidly fit into the auto-sharpened map of extended CCMV. The asymmetric unit was then refined as above while imposing torsional and adaptive distance restraints derived from the contracted structure. Imposing these restraints helped prevent unphysical geometries from occurring during the refinement in the 3.9 Å map. The quality of the models were evaluated using MolProbity [10] and PHENIX.[8] The atomic models of the asymmetric units are shown in Supplementary Fig 5.

G. Analysis of the motions of the capsid proteins during contraction

In order to analyze the motions of the capsid proteins during contraction, the particle distribution in Fig. 3e was divided into 30 slices along the first component, and a reconstruction was obtained for each slice. The model of the extended state was then rigidly fit into the reconstructions of slices 1–12 (extended and partially contracted configurations), and the model of the contracted state into the reconstructions of slices 25–30 (contracted configurations). The positions of the alpha carbons were then used to extract the geometric parameters reported in Fig. 4.

The capsid diameter (Fig. 4b) was measured along 5-fold symmetry axis and corresponds to the largest distance of two alpha carbons along this direction. The angles of the rotation of the pentamers around the 5-fold axis (Fig. 4b) were determined from the displacements of the centers of mass of the B proteins. The rotation angles of the hexamers around the 3-fold axis (Fig. 4c) represent an average of the rotation angles of the A and C proteins, which were calculated in the same manner. After subtracting the rotation of the capsomers, the superimposed rotation of each capsid protein around its center for mass was then calculated (Fig. 4d).

A4.2 Figures

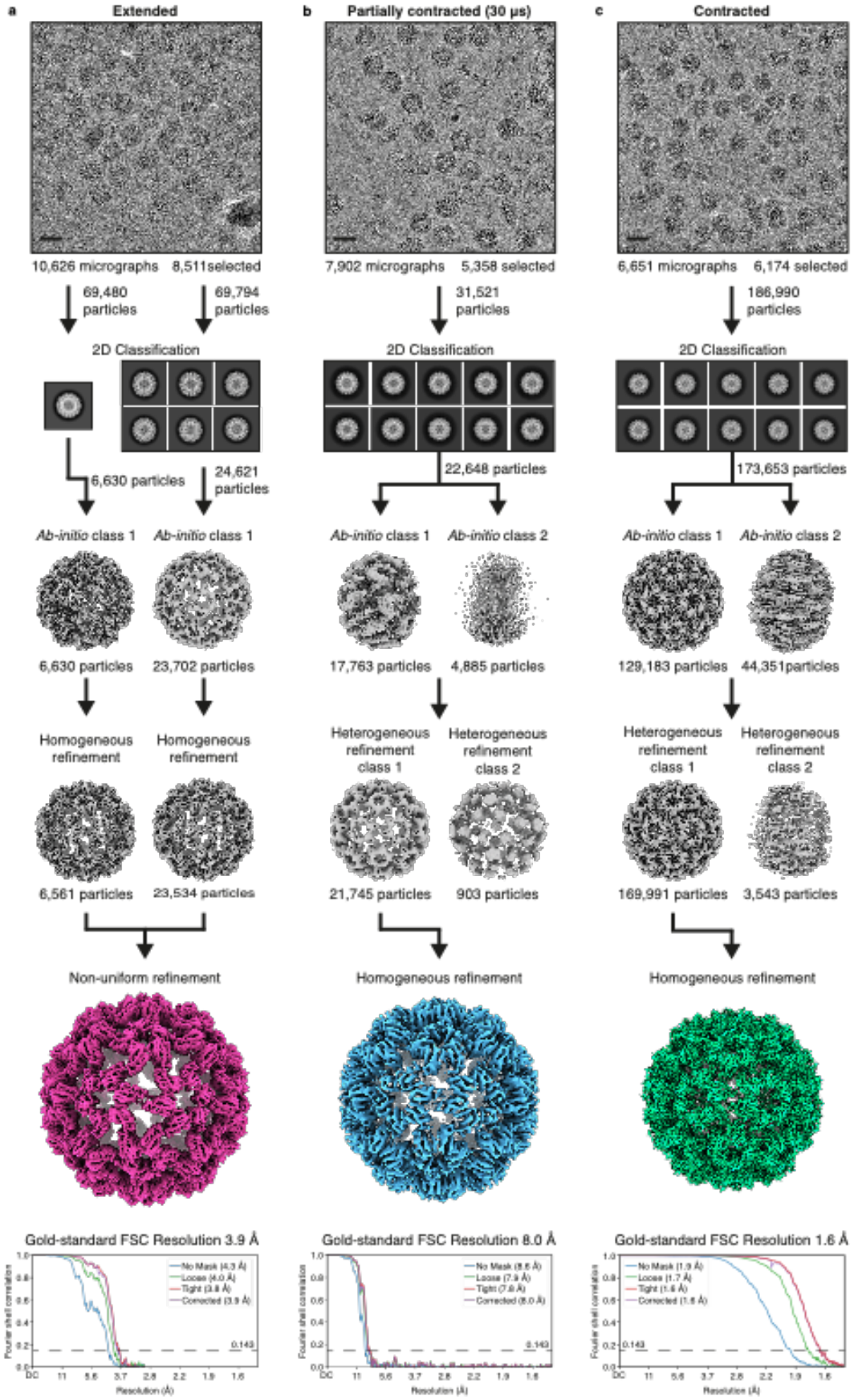
a
Extended
10,626 micrographs
8,511selected
69,480 particles
69,794 particles
2D Classification
6,630 particles
24,621 particles
Ab-initio class 1
Ab-initio class 1
6,630 particles
23,702 particles
Homogeneous refinement
Homogeneous refinement
6,561 particles
23,534 particles
Non-uniform refinement
Gold-standard FSC Resolution 3.9 Å
b
Partially contracted (30 µs)
7,902 micrographs
5,358 selected
31,521 particles
2D Classification
22,648 particles
Ab-initio class 1
Ab-initio class 2
17,763 particles
4,885 particles
Heterogeneous refinement class 1
Heterogeneous refinement class 2
21,745 particles
903 particles
Homogeneous refinement
Gold-standard FSC Resolution 8.0 Å
c
Contracted
6,651 micrographs
6,174 selected
186,990 particles
2D Classification
173,653 particles
Ab-initio class 1
Ab-initio class 2
129,183 particles
44,351particles
Heterogeneous refinement class 1
Heterogeneous refinement class 2
169,991 particles
3,543 particles
Homogeneous refinement
Gold-standard FSC Resolution 1.6 Å

Supplementary Fig. 1 | Single-particle reconstruction workflows for the extended (a), partially contracted (b), and fully contracted configurations of the CCMV capsid (c). Gold Standard Fourier Shell Correlations are shown for each data set, with the dashed black line indicating the 0.143 cutoff. For the extended configuration in (a), two datasets were processed separately and merged in the final reconstruction. Note that the micrograph in (b) shows some partially disassembled particles. These particles have likely already disassembled during the preparation of the extended state of CCMV, which is unstable and prone to disassembly. Melting and revitrification does not seem to noticeably increase the number of such partially disassembled particles (see also the micrographs in Supplementary Fig. 2a and 2b), although we cannot exclude that protonation of partially disassembled configurations leads to the further disassembly during laser melting.

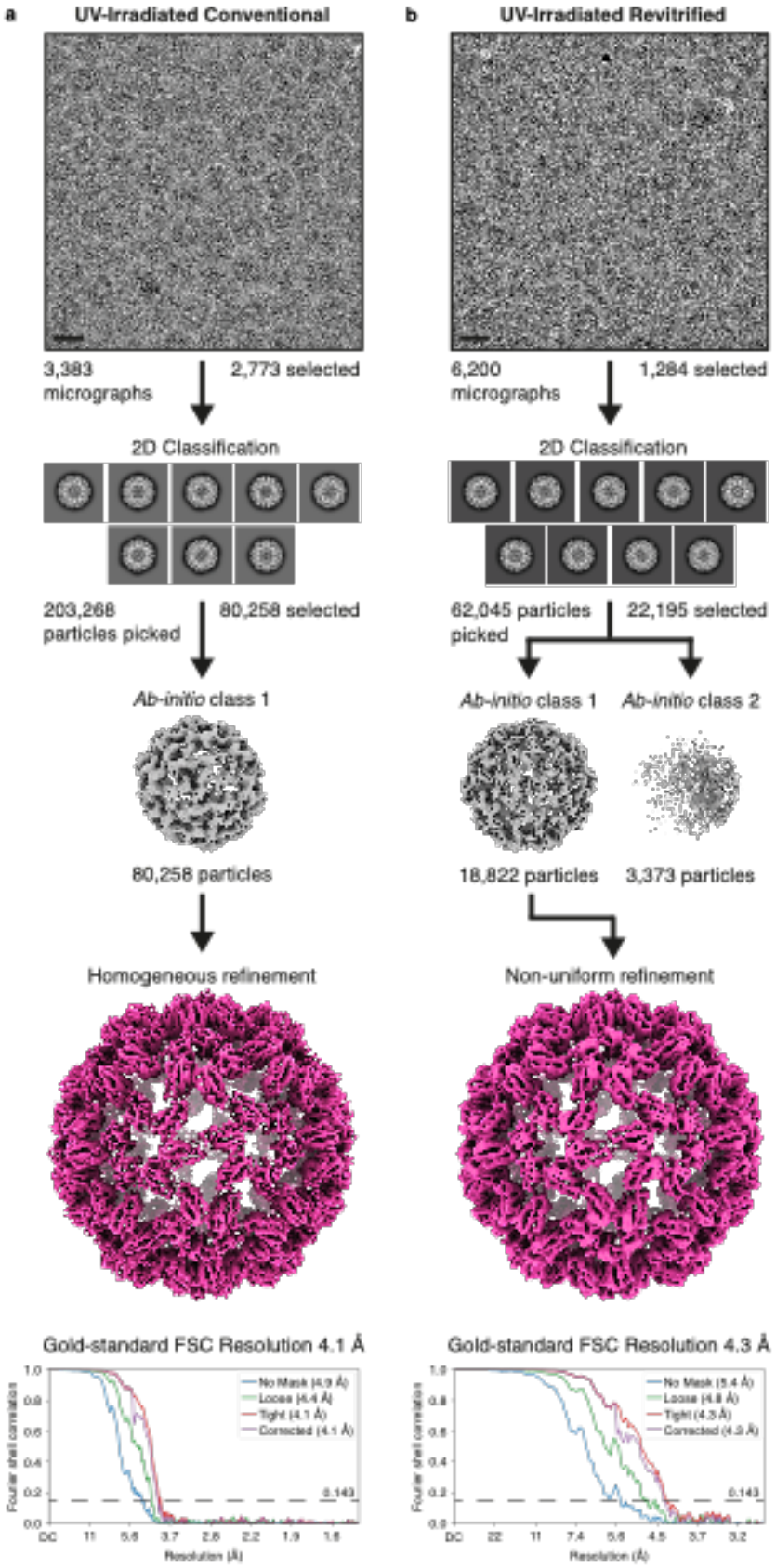
a
UV-Irradiated Conventional
b
UV-Irradiated Revitrified
3,383 micrographs
2,773 selected
6,200 micrographs
1,284 selected
2D Classification
2D Classification
203,268 particles picked
80,258 selected
62,045 particles picked
22,195 selected
Ab-initio class 1
Ab-initio class 1
Ab-initio class 2
80,258 particles
18,822 particles
3,373 particles
Homogeneous refinement
Non-uniform refinement
Gold-standard FSC Resolution 4.1 Å
Gold-standard FSC Resolution 4.3 Å
No Mask (4.9 Å)
Loose (4.4 Å)
Tight (4.1 Å)
Corrected (4.1 Å)
No Mask (5.4 Å)
Loose (4.8 Å)
Tight (4.3 Å)
Corrected (4.3 Å)
0.143
Fourier shell correlation
Resolution (Å)

Supplementary Fig. 2 | Control experiment demonstrating that the contraction of CCMV is not induced by any effect that UV irradiation might have on the particles, but instead by the pH jump created through the release of the photoacid. A sample of the extended configuration of CCMV was prepared at pH 7.5 in the absence of any photoacid and irradiated with UV light, using the same fluence as in the experiment of Fig. 3. Single-particle reconstruction workflows for conventional and revitrified sample areas are shown in (a) and (b), respectively. The reconstructions reveal that melting and revitrification does not cause the particles to contract. This demonstrates that UV irradiation alone does not induce contraction. Gold Standard Fourier Shell Correlations are shown for each data set, with the dashed black line indicating the 0.143 cutoff.

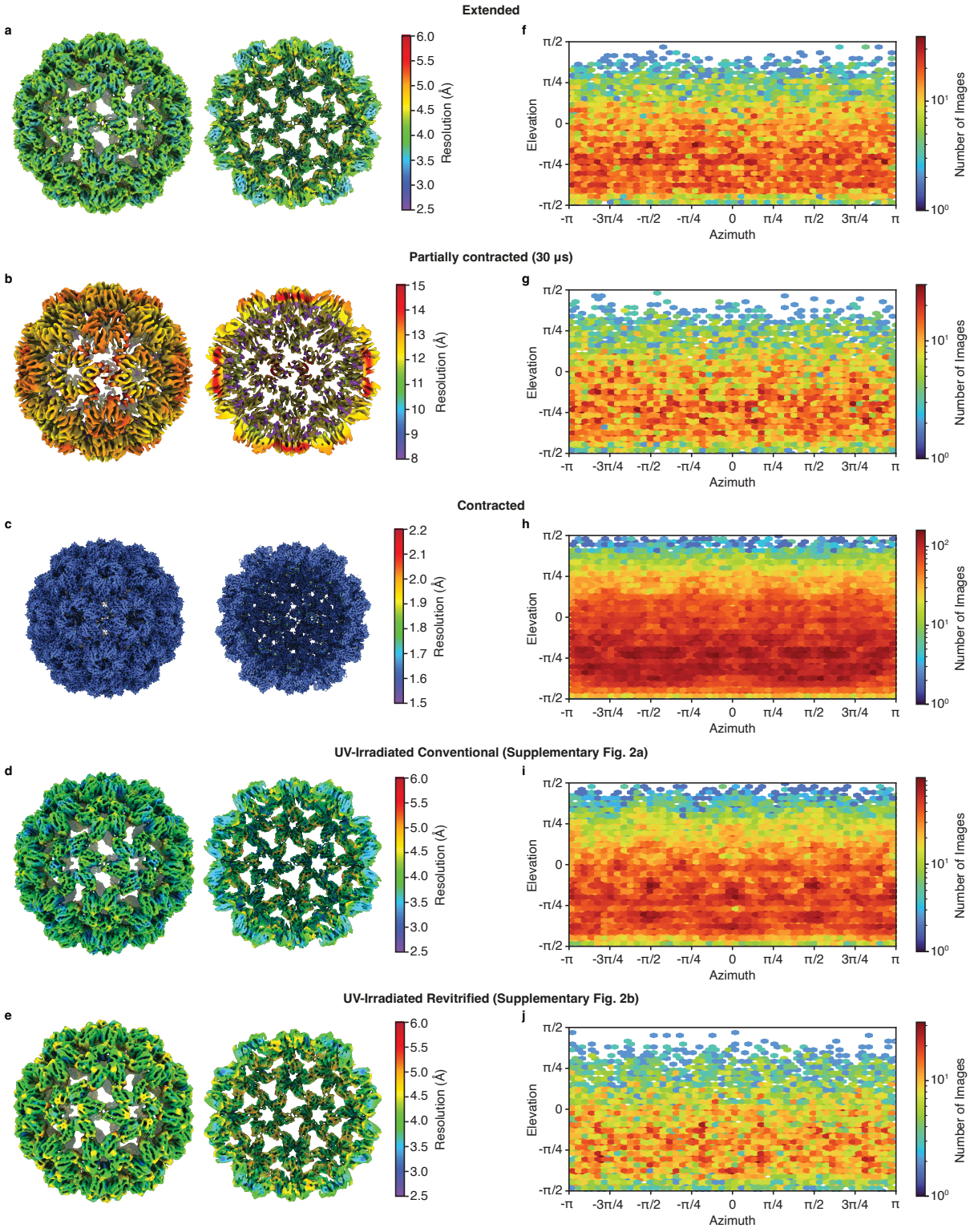

Supplementary Fig. 3 | Local resolution, and angular distribution for the reconstructions shown in the manuscript.

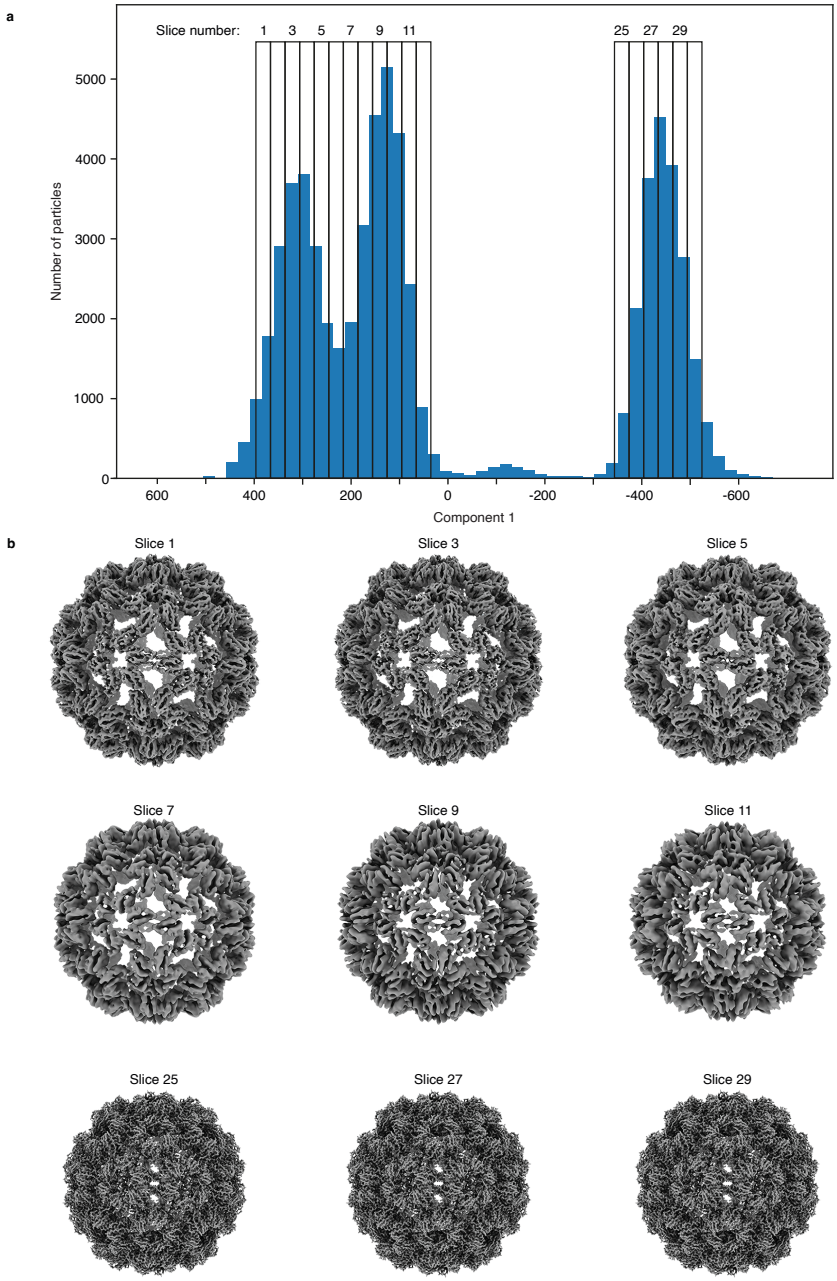

Supplementary Fig. 4 | Variability analysis of a combined dataset of the extended, partially contracted, and fully contracted configurations of CCMV from Fig. 3e. (a) The particle distribution from Fig. 3e is shown as a function of the first variability component. The distribution is divided into 30 slices along the first component. (b) A reconstruction is performed for the particles in each slice, which is used to determine the motions of the capsid proteins (Fig. 4). Here, reconstructions are shown for representative slices, which illustrate the pH jump induced contraction process.

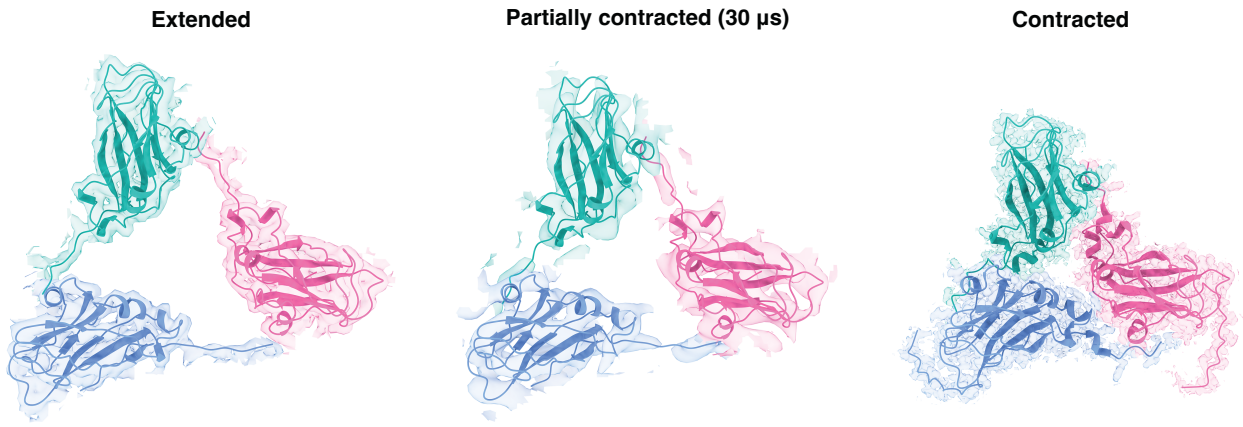

Supplementary Fig. 5 | Models of the asymmetric unit of the extended, partially contracted, and fully contracted states.

A4.3 Table

Supplementary Table 1 | Data collection parameters, and reconstruction and modelling statistics.

Figure **Name**	Fig. 3c **Contracted**	Fig. 3b **Partially contracted (30 µs)**	Fig. 3a **Extended**	Sup. Fig. 2b **UV-irradiated Revitrified**	Sup. Fig. 2a **UV-irradiate Conventional**
EMDB accession	(EMDB-16400)	(EMDB-16798)	(EMDB-16790)	(EMDB-16858)	(EMDB-16857)
PDB accession	(PDB 8C38)		(PDB 8CPY)		
Data collection					
Microscope	Thermo Fisher Titan Krios				
Detector	Falcon 4				
Energy Filter	SelectrisX, 10 eV band width				
Magnification	165,000				
Voltage (kV)	300				
Electron exposure (e–/Å^2)	50				
Defocus range (µm)	-0.3 – -0.9				
Pixel size (Å)	0.726				
Data processing					
Initial movies (no.)	6,651	7,902	10,626	3,383	6,200
Symmetry imposed	Icosahedral (I)	Icosahedral (I)	Icosahedral (I)	Icosahedral (I)	Icosahedral (I)
Initial particle images (no.)	186,990	31,521	139,274	62,045	203,268
Final particle images (no.)	169,835	21,675	30,095	18,822	79,910
Map resolution (Å)	1.6	3.9	8.0	4.3	4.1
FSC threshold	0.143	0.143	0.143	0.143	0.143
Map resolution range (Å)	1.63 – 2.16	6.76 – 9.84	3.41 – 15.06	3.17 – 6.48	2.86 – 6.35
Refinement					
Initial model used (PDB code)	1ZA7	-	8C38	-	-
Model resolution (Å)	1.61	-	3.81	-	-
FSC threshold	0.143	-	0.143	-	-
Model resolution range (Å)	1.61 – 1.65	-	3.81 – 3.93	-	-
Map sharpening *B* factor (Å^2)	40.7	1017.9	133.1	143.9	153.5
Model composition					
Non-hydrogen atoms	3,593	-	3,307	-	-
Protein residues	479	-	441	-	-
Average *B* factors (Å^2)					
Protein	4.17	-	92.09	-	-
R.m.s. deviations					
Bond lengths (Å)	0.003	-	0.005	-	-
Bond angles (°)	0.553	-	1.000	-	-
Validation					
MolProbity score	0.87	-	1.67	-	-
Clashscore	1.38	-	8.12	-	-
Poor rotamers (%)	0.00	-	0.28	-	-
Ramachandran plot					
Favored (%)	98.73	-	96.55	-	-
Allowed (%)	1.27	-	3.45	-	-
Disallowed (%)	0.00	-	0.00	-	-

A4.4 References

1. Olshin, P. K., Voss, J. M., Drabbels, M. & Lorenz, U. J. Real-time observation of jumping and spinning nanodroplets. Struct. Dyn. 7, 011101 (2020).

2. Bongiovanni, G., Harder, O. F., Voss, J. M., Drabbels, M. & Lorenz, U. J. Near-atomic resolution reconstructions from in situ revitrified cryo samples. Acta Crystallogr. Sect. Struct. Biol. 79, 473–478 (2023).

3. Punjani, A., Rubinstein, J. L., Fleet, D. J. & Brubaker, M. A. cryoSPARC: algorithms for rapid unsupervised cryo-EM structure determination. Nat. Methods 14, 290–296 (2017).

4. Pettersen, E. F. et al. UCSF CHIMERAX : Structure visualization for researchers, educators, and developers. Protein Sci. 30, 70–82 (2021).

5. Goddard, T. D. et al. UCSF ChimeraX: Meeting modern challenges in visualization and analysis: UCSF ChimeraX Visualization System. Protein Sci. 27, 14–25 (2018).

6. Speir, J. A. et al. Enhanced Local Symmetry Interactions Globally Stabilize a Mutant Virus Capsid That Maintains Infectivity and Capsid Dynamics. J. Virol. 80, 3582–3591 (2006).

7. Jurrus, E. et al. Improvements to the APBS biomolecular solvation software suite. Protein Sci. 27, 112–128 (2018).

8. Liebschner, D. et al. Macromolecular structure determination using X-rays, neutrons and electrons: recent developments in Phenix. Acta Crystallogr. Sect. Struct. Biol. 75, 861–877 (2019).

9. Croll, T. I. ISOLDE : a physically realistic environment for model building into low-resolution electron-density maps. Acta Crystallogr. Sect. Struct. Biol. 74, 519–530 (2018).

10. Williams, C. J. et al. MolProbity: More and better reference data for improved all-atom structure validation: PROTEIN SCIENCE.ORG. Protein Sci. 27, 293–315 (2018).

Acknowledgements

This thesis could not be completed successfully without the support and assistance of many great people. I would like to thank Ulrich Lorenz and Marcel Drabbels for the opportunity to do research at EPFL.

Foremost, I would like to thank the people who built the foundations for this work. In my mind, you three share and deserve more credit for all the results I presented: **Pavel Olshin** made this work possible by modifying the microscope such that the heating laser can be easily used in experiments. Aside from that, I am grateful for everything you taught me about operating and maintaining the microscope. I was always looking forward to you checking in and helping out when I was running in circles in 2021. From Congo to Cuba for 11.7k!

Christoph Schillai is undoubtedly the discoverer of this technique as he was the first person to melt and revitrify cryo-samples inside an electron microscope with a heating laser. I wish you all the best and hope that you're doing well.

Due to your groundwork, **Jon Voss** and I "only" had to put it all together. In retrospect, our journey certainly looks comical and uninformed due to the project's innovative nature. Regardless, figuring it all out during the pandemic in 2020 was just an incredible time. I think our humble and humorous approach when utterly out of our depth made it possible. Project Gorilla Ascension complete!

Next, I would like to thank everyone that worked with me on a shared project or helped during day-to-day operations: Exploring the "Henderson" effect with **Chengcheng Yan** was very interesting and rewarding for me. I hope you enjoyed the short excursion into the world of cryo-EM and going back to the lab as much as me having a new friend in the lab. Thank you for all the nice discussions and insights. I hope your future is bright, you deserve it!

Gabriele Bongiovanni deserves my gratitude for helping to repeat the experiments presented in chapter 5 at higher resolution and taking care of the writing. Together, I really enjoyed the opportunity to then mirror these experiments ex-situ with an optical microscope. But most importantly, I enjoyed our endless discussions on mathematics, finance and futurism. Up or out!

Investigating the SARS-CoV-2 Spike Protein with **Subha Jana** was truly enjoyable. Teaching you all the technique's intricacies and accompanying the experiments was a lot of fun. I wish you all the success for finishing this work. You can check out anytime!

Next, I want to thank **Constantin Krüger** and **Nathan Mowry** for being awesome colleagues and always ready to help each other out in the lab. I wish you all the best in your future plans. Chchch!

Lastly, I'd like to thank the remaining members of LND.

Enormous credit and gratitude go to everyone involved in donating, supporting the acquisition and production of biological sample solutions: The scientists at PTPSP, **Kelvin Lau**, **Florence Pojer** and **Michaël Francois**, provided and produced milliliters of protein solution necessary for these types of experiments. I am particularly grateful that you were always available to give valuable advice at a moment's notice and to teach protocols or techniques when expertise from our end did not exist.

Much gratitude is also owed to **Dong Ni** for donating top-grade apoferritin for the reconstructions presented in Chapter 5.

Jeroen Cornelissen and **Regine van der Hee** have been incredibly generous by again donating milliliters of virus solution required to make these kinds of experiments work. Your immense contribution was crucial and made this work feasible.

The Technical contributions, be it equipment or consumables, to this work were numerous, immense and invaluable given the usually short notice. The Dubochet Center for Imaging and the people running it, **Emiko Uchikawa**, **Bertrand Beckert**, **Alexander Myansnikov** and **Sergey Nazarov**, have been truly invaluable to this work. Aside from providing state-of-the-art microscopes, I was graciously allowed to use a wide range of equipment for sample preparation. Your contribution to this work by helping me make the countless perfect samples necessary for this technique while ensuring top quality data collection can truly not be overstated. You make an awesome facility and it was always a pleasure to collect and treat data together.

Davide Demurtas from CIME provided not only test samples but taught us all our practical expertise on cryo-electron microscopy. Thank you not only for excellent teaching, equipment and consumables but also for being open to our constant questions and request for advice.

Yves Morier, as my go-to member of the mechanical workshop, has been the best support I could ask for. No matter the trouble, vacuum issues, replacements, mechanical measurements or issues with the sample holder, you were always ready with a smart and practical solution. Thank you for teaching me many technical expressions in French. I wish you the best of luck and enjoyment with your future plan.

Ben Le Geyt, as my go-to member of the mechanical workshop deserves equal credit. Thank you for helping out with writing scripts, testing electrical equipment and providing insights into relics from the past.

Jacques Gremaud and **Florent Menoud** as members of the chemical stores did awesome work in providing all kinds of critical components and goods while advising on many issues. It was a luxury to rely on you maintaining this critical network and infrastructure.

Lionel Cachoulet from JEOL was incredibly helpful in anything related to the electron microscope. Thank you for helping with a large range of issues and being truly pleasant and interesting company.

Bruno Barlassina from Gatan helped immensely whenever we ran into issues with the K3, the microscope camera. I greatly appreciate all the things I learned from you in the past years.

Finally, I want to thank all the people who supported and inspired me during this time. Foremost, I would like to thank **Annick Gaudin Delmonaco** for supporting this work relentlessly in administrative and personal ways. It was always fun to show your daughter and their friends a bit of our work.

Next, I would like to thank the members of the committee, **Christoph Bostedt**, **Cécile Hébert**, **Sasha Schäfer** and **Benoît Zuber** for accepting to participate in the oral exam. Special thanks to **Christoph Bostedt** for chairing the committee and taking excellent care of the bureaucracy.

I would like to thank **Bridget Carragher** for the nice and insightful chat at the DCI Symposium in Geneva. Your detailed insights from the experiments using Chameleon convinced me to follow my idea of addressing preferred orientation with microsecond melting and revitrification. I am sure you will drive incredible research with the CZ Imaging Initiative.

I would also like to thank **Richard Henderson** and **Jacques Dubochet** for the encouraging, inspiring comments and pleasant chats.

Concluding this thesis, I would like to thank my family and my friends for their support and encouragement during this time.

Curriculum Vitae

EDUCATION & TEACHING

ÉCOLE POLYTECHNIQUE FÉDÉRALE DE LAUSANNE Feb 2020 – Jan 2024
Doctoral Assistant

- Thesis: "Microsecond Time-resolved Cryo-Electron Microscopy"
- Teaching Assistant for Quantum Chemistry and Spectroscopy

Ludwig-Maximilians-Universität München Sep 2016 – Sep 2018
Master of Science

- Thesis: "Forced convection by high-speed rotation in Czochralski growth of intermetallics"

Teaching Assistant

- Courses: Crystallography, Structure and Properties, X-Ray Diffraction, Introduction to Earth Sciences
- Laboratory Courses: X-Ray Diffraction, Polarized Light Microscopy

TECHNISCHE UNIVERSITÄT MÜNCHEN Sep 2013 – Sep 2016
Bachelor of Science

- Thesis: "Crystal growth and characterisation of $CoSb_3$"

PUBLICATIONS

OF Harder, SV Barras, M Drabbels, UJ Lorenz
Fast viral dynamics revealed by microsecond time-resolved cryo-EM
Nat Commun 14, 5649, 2023

G Bongiovanni, OF Harder, M Drabbels, UJ Lorenz
Microsecond melting and revitrification of cryo samples with a correlative light-electron microscopy approach
Frontiers in Molecular Biosciences 9, 1044509, 2023

G Bongiovanni, OF Harder, JM Voss, M Drabbels, UJ Lorenz
Near-atomic resolution reconstructions from in situ revitrified cryo samples
Acta Crystallographica Section D: Structural Biology 79 (6), 2023

OF Harder, JM Voss, PK Olshin, M Drabbels, UJ Lorenz
Microsecond melting and revitrification of cryo samples: protein structure and beam-induced motion
Acta Crystallographica Section D: Structural Biology 78 (7), 2022

JM Voss, OF Harder, PK Olshin, M Drabbels, UJ Lorenz
Rapid melting and revitrification as an approach to microsecond time-resolved cryo-electron microscopy
Chemical Physics Letters 778, 138812, 2021

JM Voss, OF Harder, PK Olshin, M Drabbels, UJ Lorenz
Microsecond melting and revitrification of cryo samples
Structural Dynamics 8 (5), 2021

M Pillaca, O Harder, W Miller, P Gille
Forced convection by Inclined Rotary Bridgman method for growth of CoSb3 and FeSb2 single crystals from Sb-rich solutions
Journal of Crystal Growth 475, 346-353, 2017